
Machine learning approach to model the microstructure and strength of nickel superalloys

Patrick Louis Taylor

Supervisor: Dr Gareth Conduit
Department of Physics
University of Cambridge

This thesis is submitted for the degree of
Doctor of Philosophy

Clare College



December 2022

Declaration

This thesis is the result of my own work and includes nothing which is the outcome of work done in collaboration except as declared in the preface and specified in the text. It is not substantially the same as any work that has already been submitted before for any degree or other qualification except as declared in the preface and specified in the text. The thesis does not exceed the prescribed word limit of 60,000 words as specified by the Degree Committee for the Faculty of Physics and Chemistry.

Publications

The following chapters have been published in peer reviewed scientific journals:

- Chapter 4 has been published as: Taylor, P. L. & Conduit, G. Machine learning predictions of superalloy microstructure. *Computational Materials Science* **201**, 110916 (Jan. 2022) [1].

Contribution: the DUQ was originally developed by Dr Gareth Conduit and expanded on by myself. The rest of the machine learning methodology described in the paper, along with all the results, are my own original work. Reviewing and editing was carried out by Dr Gareth Conduit.

- Chapter 5 has been published as: Taylor, P. L. & Conduit, G. Machine learning superalloy microchemistry and creep strength from physical descriptors. *Computational Materials Science* **227**, 112265 (Aug. 2023) [2].

Contribution: the machine learning methodology and results in this paper are wholly my own work. Reviewing and editing was carried out by Dr Gareth Conduit.

Machine learning approach to model the microstructure and strength of nickel superalloys

Patrick Louis Taylor

Nickel superalloys are a class of materials that find crucial applications in technologies such as jet and gas turbine engines. In order to accelerate the further development of these alloys, this thesis develops machine learning models that can better predict their microstructure and strength. The Gaussian process regression (GPR) models of microstructure are shown to be just as good at interpolation as traditional CALPHAD models, with advantages in speed, retrainability, incorporation of non-equilibrium effects, and the effective inclusion of computational data. By incorporating domain knowledge, it is shown that such GPR models can extrapolate into regions of composition space which include elements unseen during the training process. They can also make accurate predictions for the evolution of microstructure when heat treatments are applied. By making use of domain knowledge, similar extrapolations are possible for models of creep strength. Incorporating the results of the microstructure models leads to models of creep strength that meaningfully reveal underlying physical mechanisms of creep deformation.

Acknowledgements

First and foremost, I want to thank my supervisor, Dr Gareth Conduit, for all of the valuable guidance he has provided throughout this PhD project. He has been greatly invested in this project from the start and throughout, and has always been eager to lend his advice to me. I would also like to thank Dr Victor Milman and Dr Alexander Perlov at Dassault Systèmes UK for the help and feedback they have provided.

Funding for this PhD was provided by the UK Engineering and Physical Sciences Research Council (EPSRC) and by Dassault Systèmes via an EPSRC Industrial Cooperative Award in Science and Technology (ICASE).

I would also like to extend my thanks to the friends and colleagues who have supported me in different ways during the course of this degree: my Centre for Doctoral Training cohort, especially Tim Wallis, Ben Seddon, Philip Kloza, Alwin Bücher, and James Wills; my colleagues in the Cavendish, including my office-mate Gunnar Lange, and Jack Whaley-Baldwin, who always had an extra-curricular distraction lined up for the weekend, as well as Dr Michael Rutter for his computer support; my old friends and one-time housemates Rob Horne and Alex White; all the friendly faces at Clare College MCR over the years, too innumerable to name here. And of course I also want to thank my family, who have provided care and support throughout: mum, dad, and my sister Bea (plus Vera the cat). Last but by no means least, I'd like to thank Ekim Luo, whose love and support has transformed this last and most difficult year of my PhD.

But this is no longer the time for sprites, nickel, and kobolds. We are chemists, that is, hunters: ours are ‘the two experiences of adult life’ of which Pavese spoke, success and failure, to kill the white whale or wreck the ship; one should not surrender to incomprehensible matter, one must not just sit down. We are here for this—to make mistakes and to correct ourselves, to stand the blows and hand them out. We must never feel disarmed: nature is immense and complex, but it is not impermeable to the intelligence; we must circle around it, pierce and probe it, look for the opening or make it.

— Primo Levi, *The Periodic Table*

Contents

Declaration	i
Summary	iii
Acknowledgements	v
1 Introduction	1
1.1 Motivation	2
1.2 Aims	4
1.3 Structure of the thesis	4
2 Background	7
2.1 Machine learning	7
2.1.1 A heuristic interpretation of Gaussian process regression	7
2.1.2 Choosing the right kernel for Gaussian processes	12
2.2 Metallurgy	15
2.2.1 Modelling alloys	17
2.2.2 Nickel superalloy metallurgy	20
2.3 Design of superalloys	28
2.3.1 Discussion	31
3 Superalloy database	35
3.1 Introduction	35
3.2 Database summary	35
3.3 Pre-processing	40
3.4 Database validation	42
3.4.1 Using the distribution of uncertainty quality for validation	42
3.5 Conclusion	45
4 Machine learning predictions of superalloy phase chemistry	47
4.1 Introduction	48
4.2 Data processing	49
4.2.1 Data parameterisation	50
4.3 Computational method	52
4.3.1 Machine learning methodology	52
4.3.2 Calculation of phase compositions and fractions	54
4.4 Results and discussion	55
4.4.1 Comparison to CALPHAD	62
4.5 Conclusion	63
4.A Appendix: supplementary work to paper	65
4.A.1 Distribution of uncertainty quality	65
4.A.2 Bayesian inferral of consistent phase chemistry	66

5 Machine learning superalloy properties from physical descriptors	69
5.1 Introduction	70
5.2 Computational method	71
5.2.1 Data representation	71
5.2.2 Physical descriptors	72
5.2.3 Gaussian process regression	74
5.2.4 Probabilistic correction to phase compositions	74
5.2.5 Creep strength modelling	75
5.3 Results	76
5.3.1 Performance when all elements available	78
5.3.2 Extrapolative predictions in composition-space	79
5.3.3 Heat treatments	81
5.3.4 Creep rupture life model	82
5.4 Conclusion	84
5.A Appendix: supplementary work to paper	85
5.A.1 Bayesian correction for constraints	85
5.A.2 Further analysis of the phase chemistry GPR model	86
5.A.3 GPR model of solidus and liquidus temperatures	87
6 Designing a new superalloy	91
6.1 Introduction	91
6.1.1 Design criteria	91
6.2 Computational method	93
6.3 Results	94
6.4 Conclusion	96
7 Conclusion	99
A Embedded atom model potentials for Re and Ru	105
A.1 Introduction	105
A.2 Theory	105
A.3 Development of new potentials for Re and Ru	107
A.4 Supercells for alloy simulation	112
Bibliography	115

Chapter 1

Introduction

The English word nickel comes from the German *Kupfernickel*, which roughly translates to demon-copper. This was the name given to a mineral known to medieval German miners; it looked just like the ores that were smelted to give copper, but yielded none. Despite all the scientific advances of the intervening six centuries, the original name of element 28 is still rather apt. Like copper, its neighbour in the periodic table, nickel is tough and ductile due to its face-centred cubic (fcc) crystal structure. It retains this crystal structure—and hence its useful thermomechanical properties—up to its melting point at 1455°C , which is nearly 400°C higher than that of copper. Other transition metals with similar properties are rare and expensive—whereas nickel is the fifth most abundant element on the planet. For these reasons, nickel-based alloys have become one of the most important classes of high-temperature materials.

The development of high temperature nickel-based alloys has largely been apace with the development of their most important technological application; gas turbine engines. Gas turbine engines power jet aircraft, ships, and land-based power plants. The Brayton cycle describes the ideal operation of a gas turbine: the efficiency associated with this

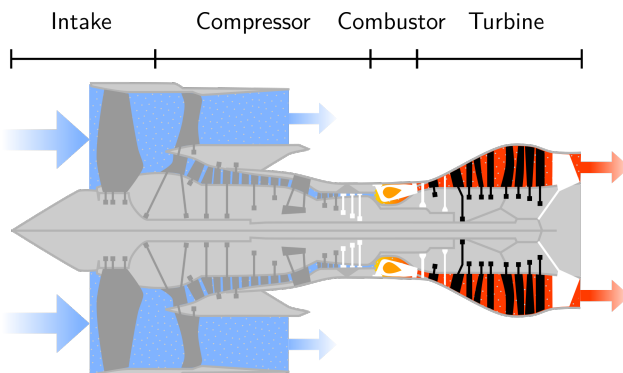


Figure 1.1: An illustrative cross section of the type of jet engine used in modern jetliners. Components in the turbine section that would typically be cast from nickel superalloys are highlighted in black. Colours (blue to red) are used to indicate the temperatures of airflow through the engine. Figure adapted from [3].

thermodynamic cycle is $\eta = 1 - T_1/T_2$, where T_2 is the operating temperature and T_1 the heat-rejection temperature. Hence, the overarching paradigm of turbine development has been to increase operating temperatures [4]. This requires a corresponding increase in the high temperature capabilities of the materials used in the hottest parts of the engine, the turbine blades and disc, see Fig. 1.1. This, in turn, means increasing the melting point, hot corrosion resistance, and high-temperature strength (mainly characterised by resistance to creep deformation and yield stress) of the nickel-based alloys. Density and elastic constants are also important properties.

This process has largely proceeded by trial-and-improvement; guided by physical insight. Over the course of nearly a century, this approach has produced a number of key discoveries, and has resulted in modern commercial nickel-based alloys with upwards of ten components and complex, multi-stage heat treatments, which can often incorporate the application of a corrosion-resistant coating. Some key discoveries are worth highlighting here. In 1940 (just after the first jet-powered aeroplanes were tested), X-ray analysis by Bradley and Taylor [5] revealed that adding Al to Ni-based alloys produced a strengthening precipitate phase. This is the γ' phase. Like the primary phase (the γ phase), it is fcc, but has an ordered structure based on Ni_3Al . In theory, the two phases are expected to completely separate at equilibrium; in practice, they form a distinctive matrix/precipitate (or γ/γ') microstructural morphology, see Fig. 2.3(c). The presence of the precipitate phase leads to a counter-intuitive *increase* in an alloy's yield stress with temperature. This is due to a mechanism that locks line defects together, limiting their motion and any resulting plastic deformation. The 'locking' mechanism is thermally activated [3]. Due to this anomalous effect, and their other extraordinary high-temperature properties, this class of nickel-aluminium alloys are called *superalloys*.

A key development of the late twentieth century was the invention of single-crystal superalloys (Fig. 2.3(a)). This allows turbine blades to be cast as single crystals of a superalloy: by eliminating the grain boundaries that are normally found in such components, their strength properties are greatly improved. At the cutting edge of superalloy development is the ongoing drive to make use of additive manufacturing (commonly referred to as 3D printing) to create jet engine parts [6–8]. This production technique can be used for rapid prototyping, as well as the creation of parts with hollow sections or complex topologies, which would be difficult or outright impossible to machine or cast using conventional techniques.

1.1 Motivation

The traditional approach to superalloy design has used physical insight to extrapolate from previous superalloy designs, making use of intensive experimentation to accurately map out and assess each proposed modification. This approach has been slow and ex-

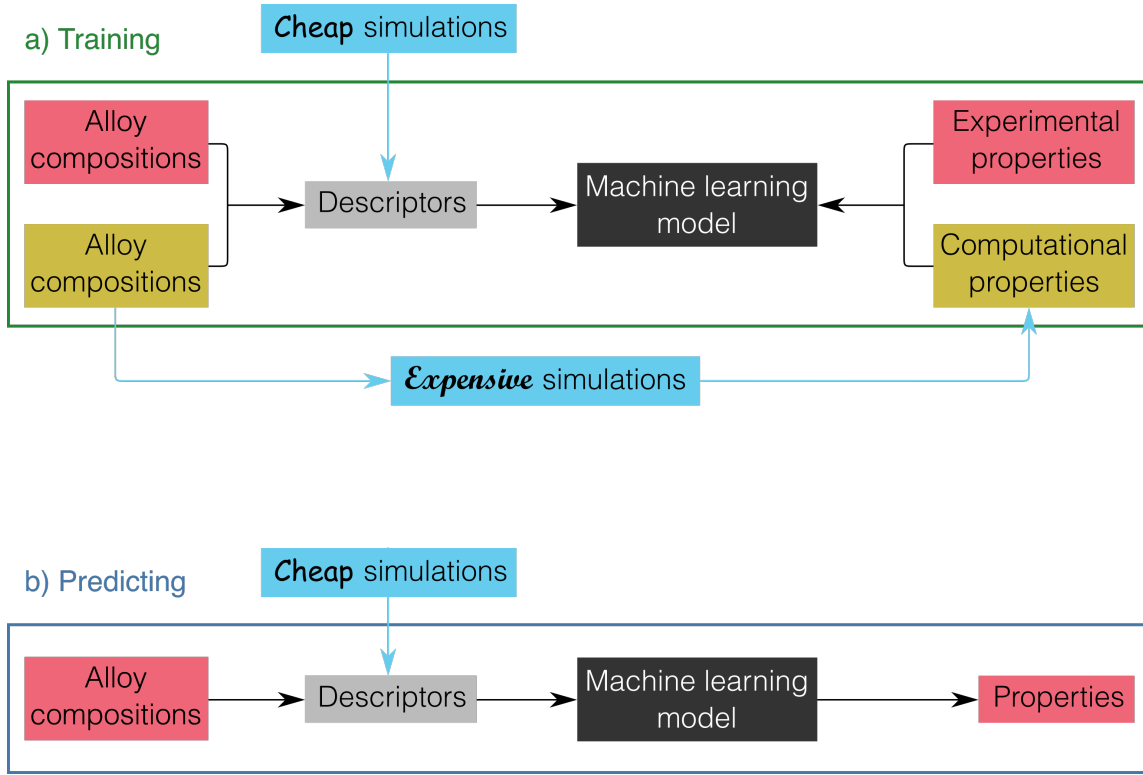


Figure 1.2: A flexible approach to modelling alloy properties, that combines machine learning with simulation methods spanning the range of possible computational costs.

pensive, with new ‘generations’ of superalloys typically arriving every 5–10 years [3, 9]. However, the ever-growing span of possibilities for the make-up of a superalloy, as well as the necessary consideration of the effects of any given modification on a range of properties, have made this approach insufficient for fully exploring the design space of superalloys. In recent years traditional superalloy development can no longer keep pace with the requirements of jet engineers. However, advancements in simulation and machine learning (ML) have opened up new approaches to superalloy design. Recently, a number of superalloys and other related alloys have been designed using a fully ML approach: a neural network learns alloy properties from input compositions, then the landscape resulting from input to property mapping is explored to find compositions corresponding to optimal properties [8, 10]. Alternatively, Pollock and Van der Ven reviewed the various recent computational developments that point towards the possibility of a fully simulation-based approach to superalloy design [11]. The simulation methods span length scales from atomistic (DFT, MD, CALPHAD) through to the macroscale¹ (Fig. 2.4 summarises this approach). This multiscale approach is essential due to the metallurgy of superalloys.

¹The mesoscale and macroscale methods are not discussed in this thesis; readers are referred to the review mentioned above [11].

Both computational methods have advantages and disadvantages. An obvious advantage of machine learning is speed: making predictions from a trained model is near instantaneous, which is helpful if tens of thousands of input compositions are to be searched to find optimal properties. On the other hand, machine learning models can only reliably make interpolative predictions; although, helpfully, most machine learning approaches output an uncertainty to accompany each prediction, so that the reliability of a prediction is always quantified. On the other hand, the simulation-based approach is expected to be suitable for extrapolation, since fundamental physics is transferable to any material. And new and exciting materials—the sorts of materials that have a revolutionary impact, like the first generation of superalloys—will be extrapolative discoveries. However, one should not automatically trust that fully-simulated predictions are accurate. In this approach, illustrated later in Fig. 2.4, each method at each scale introduces new approximations and assumptions in order for the subsequent calculations to be tractable. It is not clear that the reliability of such predictions can be easily quantified.

1.2 Aims

The aim of this thesis is to develop an approach to alloy modelling that synthesises machine learning and simulation: the proposed framework is shown diagrammatically in Fig. 1.2. It is, fundamentally, a machine learning model, and hence leverages the benefits of such a model: notably speed of prediction and quantification of predictive uncertainty. Computationally expensive simulations, such as the sort shown in Fig. 2.4, can be used to train the machine learning model. This is simply accomplished by tagging training data as being either computationally or experimentally generated: the machine learning model then has the flexibility to determine for itself whether or not the simulated data is relevant to making predictions of ‘real’ (i.e. obtained experimentally) properties.

However, the approach of this work also allows for the possibility that computationally cheap simulations—or even approximate models—of atomistic properties can adequately capture the physics of the alloys being modelled, and hence their inclusion can allow the model to extrapolate into new materials’ space. These so-called ‘cheap simulations’ enter the model as descriptors. Descriptors are mappings from alloy compositions to new, physics-based, features. These new features then enter the machine learning model as its actual input. Descriptors have to be computationally cheap to calculate, because they need to be generated each time the model is asked to make a prediction, see Fig. 1.2(b).

1.3 Structure of the thesis

Chapter 2 introduces the prerequisite background material on machine learning, nickel superalloy metallurgy, and superalloy design methodologies. Next, the database of su-

peralloy properties that is made use of in the machine learning models is detailed in Chapter 3. The pre-processing carried out to construct the database is also validated in this Chapter; this makes use of machine learning models from the subsequent chapters, as well as making novel use of a new metric (the distribution of uncertainty quality or DUQ) developed as part of this work. In Chapter 4, (published as Ref. [1]), a machine learning model of superalloy phase chemistry is developed. This model does not make use of descriptors, instead using alloy composition as a direct input. Correction methods to enforce necessary soft and hard constraints on phase chemistry are introduced, as well as a proper introduction of the DUQ. This model is benchmarked against CALPHAD in an extrapolation test, and is shown to have a small quantitative edge. In Chapter 5, the phase chemistry model is expanded on by making use of descriptors and a different correction method. It is shown that these models perform better on interpolation than plain-descriptor models; but also that they are able to effectively extrapolate in composition and processing space, with examples provided of both use-cases. A machine learning model of creep strength is also trained using a similar descriptor-based approach. Finally, Chapter 6 demonstrates a proof-of-concept tool that makes use of the various machine learning models of superalloy properties to design a new nickel superalloy. After concluding in Chapter 7, Appendix A includes some additional work towards atomistic simulations of nickel superalloys using molecular dynamics.

Chapter 2

Background

2.1 Machine learning

The aim of this section is to introduce the machine learning methods—specifically, Gaussian process regression—that are made use of throughout this thesis. Gaussian processes are an approach to machine learning that can be used for supervised tasks¹. Like all machine learning methods, they have associated pros and cons. The main pro is that unlike most other machine learning methods, the theory describing how they work is not ad hoc; rather it has been developed from formal Bayesian statistics. Consequently, a trained Gaussian process is in no sense a ‘black box’, and is instead readily interpretable. Their major con is that they are slow to train, having computational complexity $\mathcal{O}(N^3)$ with the number of training data entries N .

There are plenty of texts that thoroughly cover the development of the theory of Gaussian processes using Bayesian probability theory; the classic text, *Gaussian Processes for Machine Learning* by Rasmussen and Williams is considered to be the ‘bible’ for this topic [12]—this section will borrow their notation. However, it seems that in practical usage, plenty of scientists are quite happy to accept that Gaussian processes have a rigorous statistical basis and are more interested in their practical implementation and heuristic interpretation. In this section I will aim to describe just that.

2.1.1 A heuristic interpretation of Gaussian process regression

Recall Bayes’ theorem:

$$P(A|B) = \frac{P(B|A) P(A)}{P(B)} .$$

¹This work is concerned with just one type of supervised learning task, regression, i.e. fitting a curve to a set of datapoints.

The posterior probability, $P(A|B)$, is the probability of event A , given event B . It is equal to the likelihood, $P(B|A)$, conditioned on the prior, $P(A)$, which is the probability of event A , without knowledge of B .

Scientists typically ask the following question: I have a hypothesis, \mathcal{H} . In order to determine if it's a good hypothesis, I've gone and done an experiment. This involved making a series of n measurements of a dependent variable, $\mathbf{y} \in \mathbb{R}^n$, in response to varying a set of m independent variables $X \in \mathbb{R}^{n \times m}$. Does the data I've gathered support my hypothesis? Bayes' theorem can be reformulated to represent this key question:

$$P(\mathcal{H}|X, \mathbf{y}) \sim P(\mathbf{y}|\mathcal{H}, X)P(\mathcal{H}|X) .$$

It can be seen that the prior represents our hypothesis—specifically, the probability of our hypothesis holding given the available data—and the likelihood represents how likely it is that these measurements have been observed given said hypothesis. Note that the marginal probability, $P(B)$, has been ignored, and for the purposes of this section can be thought of as a normalisation factor.

A further reformulation brings us a step closer to something that looks like a machine learning model. As practical scientists, we will formulate our hypothesis in terms of a mathematical function with output \mathbf{f} , which hopefully the measured dependent variable values \mathbf{y} will lie as close to as possible. And as we want to develop scientific theories that will benefit our fellow humans, the real question of interest is whether this theory can be applied to predict the outcome of our experiment, f_* , under different measurement conditions, \mathbf{x}_* . This can be formulated probabilistically as follows²:

$$P(f_*|X, \mathbf{y}, \mathbf{x}_*) \sim \int P(\mathbf{y}|\mathbf{f}, X)P(\mathbf{f}, f_*|X, \mathbf{x}_*)d\mathbf{f} . \quad (2.1)$$

Note the integration over function space: this allows for the possibility that the exact function that describes our hypothesis is unknown. This isn't so different from the familiar case of fitting a straight line through a set of $x - y$ data, in which case the hypothesis is that there's a linear relationship, but the exact gradient of the line is unknown.

It can be seen that Eq. 2.1 contains a lot of probability distributions. Without getting bogged down in mathematical detail, it will suffice to say that the easiest way to ensure this formula is mathematically tractable is to assume that each probability distribution is Gaussian. Each term on the right hand side of Eq. 2.1 can be expressed as a multivariate normal distribution, characterised by a mean and covariance. The likelihood is the easiest

²As formulated in Eq. 2.1, we now have what is called a regression model in the field of machine learning. Because machine learning engineers typically want to make it sound like their models are replicating human intelligence, they call the initial dataset, X and \mathbf{y} , the training dataset. The new measurement, \mathbf{x}_* , is called a test input.

to express:

$$P(\mathbf{y}|\mathbf{f}, X) = \mathcal{N}(\mathbf{f}, \sigma_n^2 I) . \quad (2.2)$$

Here σ_n^2 is the variance of the noise in our measurements.

The prior is more interesting:

$$P(\mathbf{f}, f_*|X, X_*) = \mathcal{N}\left(\mathbf{0}, \begin{bmatrix} K(X, X) & K(X, \mathbf{x}_*) \\ K(\mathbf{x}_*, X) & k(\mathbf{x}_*, \mathbf{x}_*) \end{bmatrix}\right) . \quad (2.3)$$

The new function that has been introduced, $k(\mathbf{x}, \mathbf{x}')$ is called the kernel. K is simply the matrix representation of the kernel, i.e. $K_{ij} = k(\mathbf{x}_i, \mathbf{x}_j)$. The kernel encapsulates our prior knowledge about the problem. One simple, often quoted interpretation of the kernel is that it expresses the expected similarity between two inputs, \mathbf{x} and \mathbf{x}' .

Putting all of this together, the left hand side of Eq. 2.1 can be expressed as (see Rasmussen and Williams [12] for a thorough derivation):

$$P(\mathbf{f}_*|X, \mathbf{y}, X_*) = \mathcal{N}(\bar{\mathbf{f}}_*, \text{cov}(\mathbf{f}_*)) , \quad \text{with} \quad (2.4)$$

$$\bar{\mathbf{f}}_* = K(X_*, X) [K(X, X) + \sigma_n^2 I]^{-1} \mathbf{y} , \quad (2.5)$$

$$\text{cov}(\mathbf{f}_*) = K(X_*, X_*) - K(X_*, X) [K(X, X) + \sigma_n^2 I]^{-1} K(X, X_*) . \quad (2.6)$$

The predictive mean, Eq. 2.5, is used as the prediction value, and the diagonal of the predictive covariance, Eq. 2.6, is used as the uncertainty associated with the prediction. This is one of the pros of Gaussian process regression; the uncertainty drops out for free, whereas other approaches to ML require making use of techniques such as bootstrapping to calculate an uncertainty. For both equations, a matrix inversion is required: a Cholesky decomposition is typically used, which has computational complexity $\mathcal{O}(N^3)$ for a rank N matrix. Pseudocode 2.1 & 2.2 describes the steps in a practical implementation of Gaussian process regression.

Fitting a Gaussian process regression model

There is an issue with what's been laid out above: it is likely that exactly what the kernel function, $k(\mathbf{x}, \mathbf{x}')$, should be is unknown. At best, it is probably possible to specify a functional form parameterised by a set of variables $\boldsymbol{\theta}$ (see the next subsection 2.1.2). And the noise level of our observations, σ_n , is almost certainly unknown. Like in all approaches to machine learning, the parameters $\{\boldsymbol{\theta}, \sigma_n\}$ will have to be fitted in order to produce a model that gets as close to our training data as possible. When using other machine learning methodologies, this is done via cross-validation and minimisation of a loss function (e.g. the mean-squared error) over the validation datasets. A neat feature

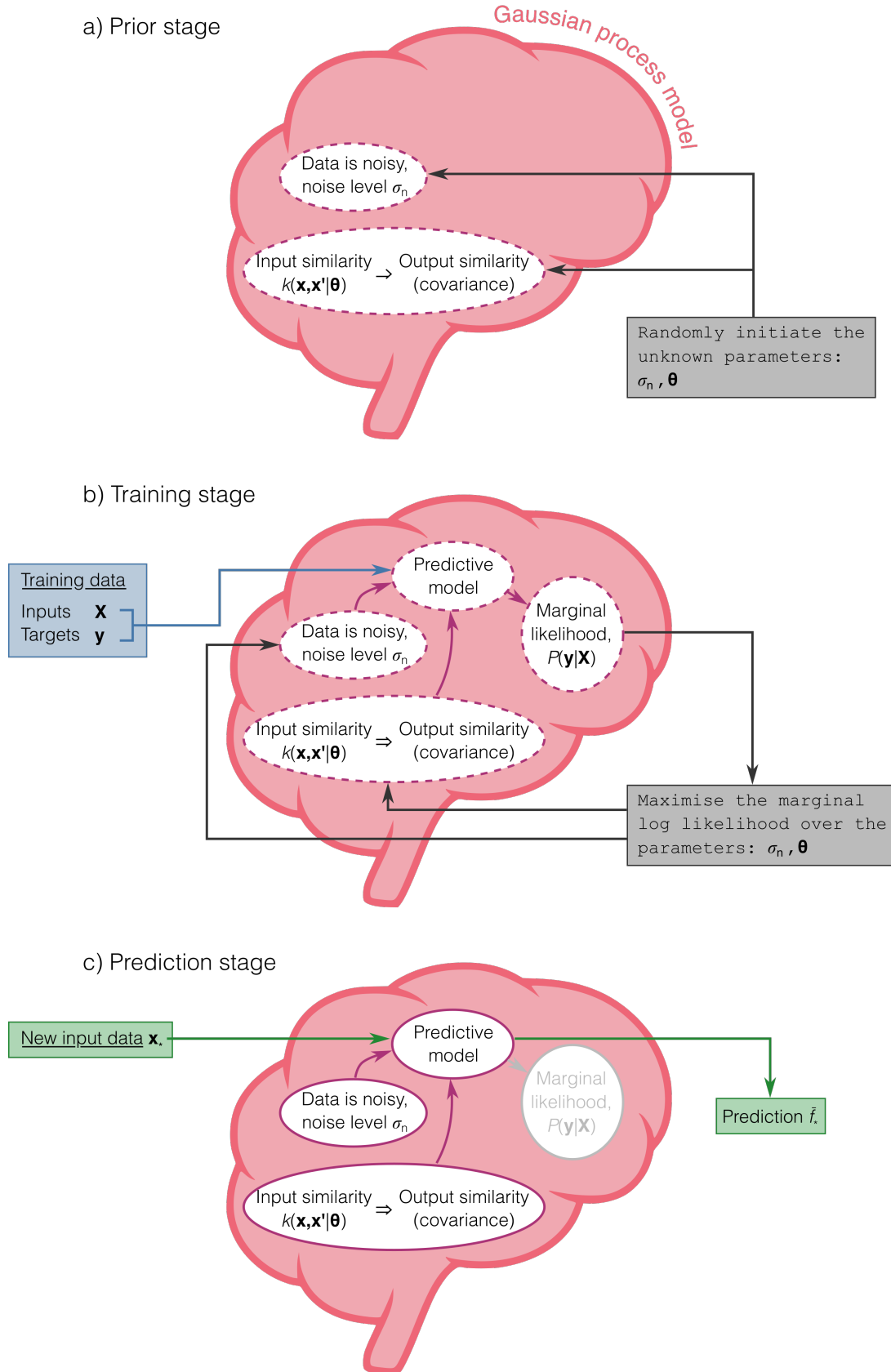


Figure 2.1: A Gaussian process ML model can be visualised in three stages: a prior stage, a training (parameter optimisation) stage, and a (trained) prediction stage.

Pseudocode 2.1 Training a Gaussian process regression model (adapted from Rasmussen and Williams, Chapter 2 [12]).

input: Training data inputs X and corresponding targets \mathbf{y}

output: Maximal value of the marginal log likelihood (MLL).

- 1: Randomly initialise the kernel and noise parameters θ, σ_n .
- 2: **while** MLL not maximised **do**
- 3: $L \leftarrow \text{cholesky}(K(X, X|\theta) + \sigma_n^2 I)$
- 4: $\alpha \leftarrow L^T \backslash (L \backslash \mathbf{y})$
- 5: $\text{mll} \leftarrow -\frac{1}{2}\mathbf{y}^T \alpha - \sum_i \log L_{ii} - \frac{n}{2} \log 2\pi$ ▷ The marginal log likelihood Eq. 2.7
- 6: $\theta, \sigma_n \leftarrow \text{maximiser}(\text{current mll}, \text{previous mll}, \theta, \sigma_n)$
- 7: **end while**
- 8: **return** maximal MLL

Pseudocode 2.2 Making predictions with a Gaussian process regression model (adapted from Rasmussen and Williams, Chapter 2 [12]).

input: Test input \mathbf{x}_* . Precalculated Cholesky decomposition, L , and solution to lower triangular system, α (see Pseudocode 2.1).

output: Predicted mean and variance.

- 1: $\bar{f}_* \leftarrow \mathbf{k}_*^T \alpha$ ▷ The predictive mean Eq. 2.5
- 2: $\mathbf{v} \leftarrow L \backslash \mathbf{k}_*$
- 3: $\text{var}(f_*) \leftarrow k(\mathbf{x}_*, \mathbf{x}_*) - \mathbf{v}^T \mathbf{v}$ ▷ The predictive variance Eq. 2.6
- 4: **return** \bar{f}_* (predictive mean), $\text{var}(f_*)$ (predictive variance)

of Gaussian process regression is that this doesn't need to be done. Using our various probability distributions and Bayes' rule, it is possible to write down a so-called marginal likelihood $P(\mathbf{y}|X)$. This is also called the evidence—it is literally just that, the likelihood that our model fits our training observations. It can be seen from Eq. 2.2 and Eq. 2.3 that the training observations are distributed as $\mathbf{y} \sim \mathcal{N}(\mathbf{0}, K + \sigma_n^2 I)$. This yields the following for the log marginal likelihood:

$$\log P(\mathbf{y}|X) = -\frac{1}{2}\mathbf{y}^T(K(X, X) + \sigma_n^2 I)^{-1}\mathbf{y} - \frac{1}{2}\log |K(X, X) + \sigma_n^2 I| - \frac{N}{2}\log 2\pi . \quad (2.7)$$

The parameters $\{\boldsymbol{\theta}, \sigma_n\}$ can be optimised by maximising the log marginal likelihood according to this expression. Eq. 2.5, Eq. 2.6, and Eq. 2.7 are the only expressions needed to implement Gaussian process regression (along with libraries for Cholesky decomposition and bounded optimisation).

Fig. 2.1, inspired by the vaguely anthropomorphic descriptions often used in ML, represents a Gaussian process in three stages. In stage (a), the prior stage, the model already has some ‘prior’ knowledge about the problem in question. Stage (b) represents the fitting—or training—procedure described above. In stage (c), the model has been fully trained and is ready to make predictions. These three stages can be compared to e.g. a conventional neural network. In stage (a), there would be a network with random weights. The user may have used some prior knowledge to determine the number of neurons and layers, but that prior knowledge is extrinsic to the model, unlike a GP where it is an intrinsic part of the model. For the neural network, stage (b) and (c) would then be much the same as for the Gaussian process.

2.1.2 Choosing the right kernel for Gaussian processes

The kernel $k(\mathbf{x}, \mathbf{x}')$ is the function that describes the similarity between two input vectors \mathbf{x} and \mathbf{x}' . As described above, its exact form needs to be somewhat flexible in order to optimise it for the problem at hand, and as such should be specified by one or more parameters $\boldsymbol{\theta}$. The matrix $K(X, X)$ with entries $K_{ij} = k(\mathbf{x}_i, \mathbf{x}_j)$ is called the Gram matrix, and since it can represent a covariance matrix, it must be positive semi-definite [12]. A further simple (although not necessary) condition, is that the kernel should be *stationary*. This means that the similarity between two input vectors should depend on the difference between them but should not vary when equal translations are applied to each vector; a sensible requirement for most (non-discrete) input vectors. For example, the following kernel is not stationary:

$$k(\mathbf{x}, \mathbf{x}') = \mathbf{x} \cdot \mathbf{x}' .$$

This is called the dot product kernel, and it is not stationary because $k(\mathbf{x}, \mathbf{x}') \neq k(\mathbf{x} + \mathbf{a}, \mathbf{x}' + \mathbf{a})$. Interestingly, usage of the dot product kernel reduces the GPR model to be equivalent to Bayesian Ridge Regression [12–14].

Two main types of stationary kernel are used in this work. The first is the squared exponential (or Gaussian radial basis function) kernel:

$$k(\mathbf{x}, \mathbf{x}'|l) = \exp\left(-\frac{1}{2}\|\mathbf{x} - \mathbf{x}'\|^2/l^2\right) . \quad (2.8)$$

The second is the Matérn kernel:

$$k(\mathbf{x}, \mathbf{x}'|l, \nu) = \frac{2^{1-\nu}}{\Gamma(\nu)} \left(\frac{\sqrt{2\nu}\|\mathbf{x} - \mathbf{x}'\|}{l}\right)^\nu K_\nu\left(\frac{\sqrt{2\nu}\|\mathbf{x} - \mathbf{x}'\|}{l}\right) , \quad (2.9)$$

where K_ν is a modified Bessel function. However, for the special case that ν is half integer, the function greatly simplifies to the product of a kernel and an exponential term [12]. In practice, these special values are almost always used—they are far more computationally efficient due to not containing Bessel functions.

In both of these kernels, the parameter l is referred to as a lengthscale. In Eq. 2.8 it is especially easy to see why it is called that, as here l is approximately the lengthscale beyond which two inputs are not significantly ‘similar’. Both kernels can be modified into an automatic relevance determination (ARD) form [13]. In this case, each feature of the input has a corresponding lengthscale, e.g. the squared exponential kernel becomes:

$$k(\mathbf{x}, \mathbf{x}'|\mathbf{l}) = \exp\left(-\frac{1}{2}\sum_i|(x_i - x'_i)/l_i|^2\right) . \quad (2.10)$$

When using an ARD kernel, each input feature is independently ‘relevant’ (or not) to the model. Irrelevant features have very large lengthscales compared to relevant features (typically, several orders of magnitude larger). This is extremely useful in models where we don’t *a priori* know whether all the features will be equally important (see Chapter 5). The ARD kernel has as many parameters as there are features; like in other machine learning models, there is a trade-off here. The model can achieve a more accurate fit, but at the risk of overfitting. Additionally, the optimisation procedure becomes more expensive, as it takes longer to ‘explore’ the much higher dimensional parameter landscape.

The smoothness of a kernel

So why choose one form of stationary kernel over another? Kernels can be characterised by their *smoothness*: literally, how smoothly their measure of similarity varies. There are several ways to look at this mathematically, including the upcrossing rate and the

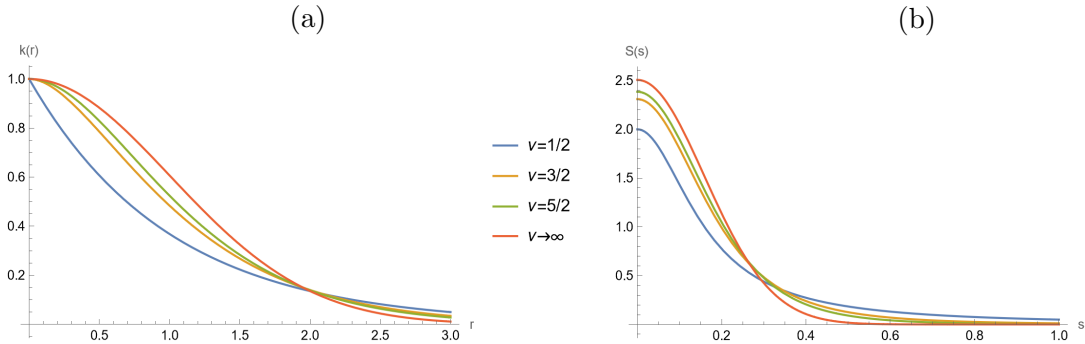


Figure 2.2: (a) examples of the Matérn kernel for different values of ν and $l = 1$. (b) the corresponding spectral densities. Note that the case $\nu \rightarrow \infty$ is equivalent to the squared exponential kernel.

mean square continuity and differentiability, see Rasmussen and Williams Chapter 4 for details [12]. It is also possible to look at the spectral density of the kernel:

$$S(\mathbf{s}) = \int k(\tau) e^{-2\pi i \mathbf{s} \cdot \tau} d\tau , \quad (2.11)$$

that is, the Fourier dual of the kernel, with $\tau = \mathbf{x} - \mathbf{x}'$ for a stationary kernel. Smoother kernels have more of their spectral density concentrated near $\tau = \mathbf{0}$. Examples for the Matérn kernel are shown in Fig. 2.2. Since it is isotropic, the kernel has been written in terms of $r = \|\mathbf{x} - \mathbf{x}'\|$. As the parameter ν increases, the kernel becomes smoother. The limiting case, $\nu \rightarrow \infty$, is in fact equivalent to the squared exponential kernel.

The spectral density view is an informative way of looking at kernels, and has been used to design new, more general, kernels such as the spectral mixture kernel [15].

2.2 Metallurgy

Nickel superalloys are primarily used in jet engines and ground-based gas turbines' blades and turbine discs. Found in the final stage of a gas turbine, these are the hottest components; in a jet engine, the gas stream in the turbine section can attain temperatures of 1800 K at take-off. In general, Ni superalloys possess a number of properties that make them well-suited to these use-cases. The high melting point they inherit from Ni is a crucial property for their high temperature applications. Typically, Ni superalloys have a yield stress that increases with temperature up to around 1050 K [3, 18]. The components that superalloys are used in undergo extreme mechanical fatigue, and so creep strength is widely considered one of the most important strength properties. In fact successive generations of superalloys have increasingly been designed to improve on the creep strength. This is especially true of the single crystal superalloys for use in turbine blades [19, 20]. Other important properties are density and thermal expansivity [21, 22].

This is by no means an exhaustive list of important properties—new superalloys are designed to meet certain design criteria, depending on their intended use-case. For example, an area of much active research is the design of nickel superalloys for additive manufacturing (i.e. 3D printing). Conventional superalloys have been found to be susceptible to hot cracking when printed, and the mechanisms responsible have not been fully elucidated [6, 23, 24]. Properties such as the liquidus-solidus temperature range have been proposed to be important [25, 26].

Like all alloys, superalloys have relevant structure spanning multiple lengthscales (refer to Fig. 2.3 for an illustration of this). Here, ‘relevant’ means that the structures arising at each lengthscale, and the associated physics, inform the final properties of the alloy. And the structures are hierarchical: the properties of the lower level structure inform the structure at the next lengthscale, and so on.

This can be summarised a little more explicitly for the specific case of superalloys. Nickel superalloys have unique microstructure, from which they derive many of their exceptional high temperature properties; they typically contain two constituent phases, the γ and γ' phase, which form into the matrix/precipitate pattern shown in the SEM image Fig. 2.3(c) in white and black respectively. The prototypical example of these phases are fcc Ni (Strukturbericht designation A1) for the γ phase (the matrix phase) and Ni_3Al (Strukturbericht L1₂) for the γ' phase (precipitate phase). These are the two phases found in the section of the binary Ni-Al phase diagram with Al fraction under 25%. The γ phase can be considered a solid solution, as there is only limited experimental evidence to suggest that short-range ordering occurs amongst the various alloying elements [27–29]. In the γ' phase, each sublattice—corresponding to either Ni or Al sites in the prototypical Ni_3Al —can be considered to be a separate solid solution, with alloying additions of a given species typically partitioning to a preferred sublattice [30–32].

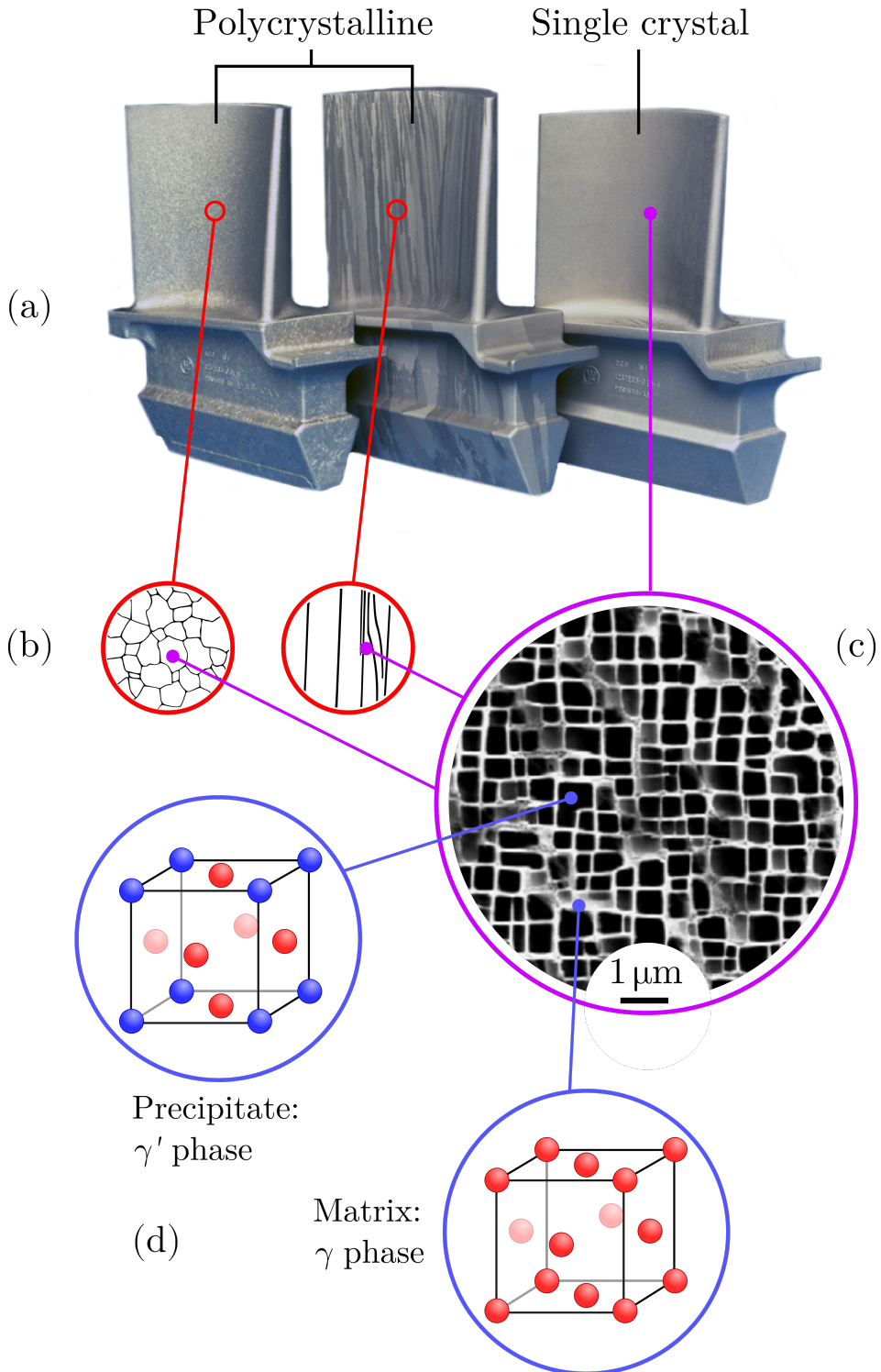


Figure 2.3: The microstructure of Ni superalloys across different scales. (a) different turbine blade castings, (b) crystal structure of the polycrystalline blades, (c) matrix/-precipitate microstructure, and (d) the prototypical precipitate and matrix phases. Blue atoms are Al and red Ni. Images from [3, 16, 17].

And in both phases, disordering due to alloying elements is substitutional not interstitial. The properties of each constituent phase combine together with the morphology of the two phase microstructure, then in turn with the polycrystalline structure of the alloy, to give its overall properties. In single crystal superalloys—from which components are literally grown as a single crystal—the properties arising from those of the two phases and their interaction in the microstructure directly lead to the overall properties, as illustrated in Fig. 2.3. A detailed account of the microstructure of Ni superalloys is provided in the texts by Reed and Durand-Charré [3, 33].

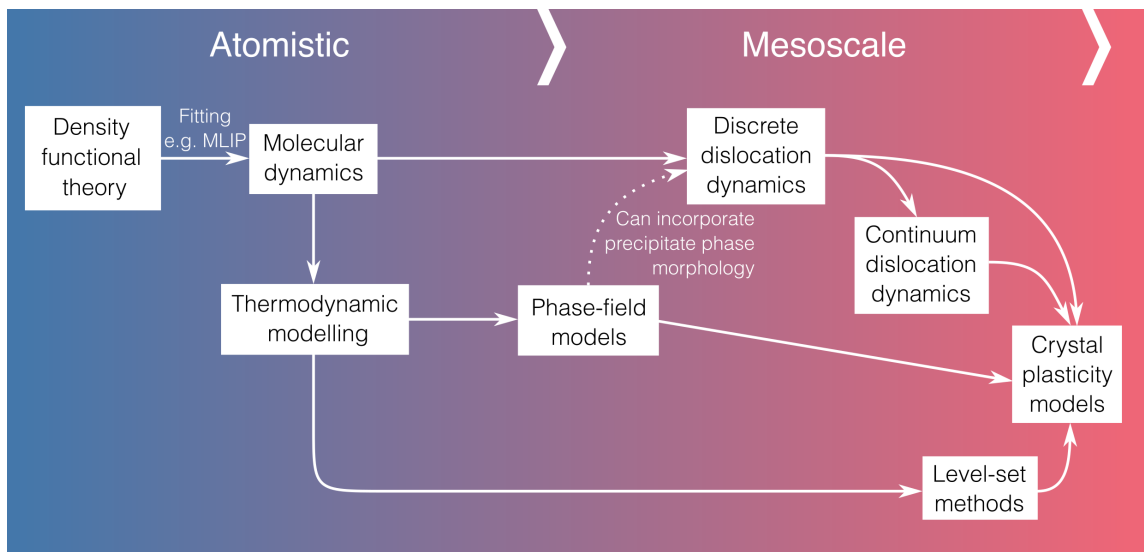


Figure 2.4: An approach to simulating alloy properties from first principles. Thermomechanical properties of interest can be calculated from crystal plasticity modelling. Simulation scales increase (approximately) from left to right.

2.2.1 Modelling alloys

The focus of this work is on using machine learning to model the properties of nickel superalloys. However, it is also necessary to consider physical models of superalloy properties, as a) a point of comparison, and b) due to the possibility of incorporating such models into the machine learning framework in order to improve the transferability of the ML model (see Fig. 1.2). A schematic of how one might go about simulating alloy properties is shown in Fig. 2.4. Each subsequent stage in the overall simulation procedure requires further approximations. This starts with the first step, atomistic modelling. Here we will give details of atomistic simulations and thermodynamic modelling (CALPHAD), as they tie into the overall modelling approach proposed in this work. Of the mesoscale methods, phase-field and level-set methods model diffuse and sharp interfaces, respectively [11, 34, 35]. Dislocation models feed-forward into crystal plasticity models, from which thermomechanical properties such as creep strength can be computed [36, 37]. For

a review of state-of-the-art multiscale alloy simulation see Pollock & Van Der Ven [11]; for a more detailed review of multiscale plasticity modelling, see Bertin *et al.* [36].

Atomistic modelling

Focusing first on true ab initio approaches such as density functional theory (DFT), we immediately run into a number of problems. Alloy phases exist in solid solution, meaning atoms belonging to each atomic species are randomly distributed throughout their crystal lattices. Fortunately, Ni superalloys are substitutional alloys—i.e. the alloying elements occupy lattice sites of the base structure, in this case fcc Ni for the γ phase and L1₂ Ni₃Al for the γ' phase, so interstitial atoms are never considered. But the number of random arrangements of atoms on a given supercell lattice is large. For an alloy of n atomic species, each with fraction x_i , and total lattice sites N , the total number of arrangements is $N!/\prod_i n_i!$ before taking the lattice's space group operations into account. Appendix A.4 provides an estimate for the minimum size of a supercell required for a pseudorandom atomic configuration to be representative of a given alloy; it scales with the number of components in the alloy system. Then the computational cost of the simulation scales as $\mathcal{O}(N^3)$ with the N electrons in the simulation cell [38].

In the literature, we find a number of approximate approaches to choosing alloy supercells for atomistic simulations. The special quasirandom structure (SQS) method: find a supercell that is sufficiently small that it is not prohibitively computationally expensive to simulate but which still captures the key physics of an infinitely sized supercell [39–42]. The cluster variation method (CVM): consider the contribution of different configurations of atoms to the overall energy of the structure and compute their energies as smaller, less expensive ‘clusters’ that can then be used in e.g. Monte Carlo simulations [43–47]. Or, ignore the higher entropy structures that arise due to having many elements in the alloy and carry out calculations for Ni–X binary alloys (for the γ phase) or Ni₃(Al,X) ternary alloys (for the γ' phase), from which physical effects can be inferred—or a superposition of the effects of each alloying element X is used as an estimate for the solid solution alloy [48–52].

Once an appropriate method of generating simulation supercells has been chosen, ab initio methods run into further problems. Superalloys are used for their high temperature properties, and hence capturing thermal effects in the simulations are crucial. This means phonons need to be modelled, requiring the use of even larger supercells. To capture effects such as lattice expansion, the use of a quasiharmonic modelling approach is required [48, 53, 54]. The simulation can rapidly become prohibitively expensive, all whilst introducing further and further approximations. Many researchers simulating superalloys have focused on calculating stacking fault energies [40, 50, 51, 55] and anti-phase boundary energies [42, 49, 54], where the main energy contributions are electronic not

thermal.

Molecular dynamics is an alternative approach to atomistic modelling, with a much lower computational cost and scaling ($\mathcal{O}(N)$ with the number of atoms compared to $\mathcal{O}(N^3)$ with the number of electrons for DFT). However, the simulation is premised on the quality of the interatomic potentials being used. Accurate potentials covering a large number of atomic species are not readily available (see Chapter A)—recall that modern commercial superalloys can contain upwards of eight different elements in non-trace amounts. Machine learned interatomic potentials (MLIPs) offer a potential route to ‘best of both worlds’ simulations—they can get close to the accuracy of the DFT simulations they were trained on whilst demonstrating much better transferability than traditional potentials [56–60]. State-of-the-art MLIPs have been designed to simulate alloys with up to five components [47, 61–65].

CALPHAD

As discussed above, a key property underlying the phenomenal high temperature properties of Ni superalloys is their unique sub-crystal scale matrix/precipitate microstructure [19, 20, 66] (Fig. 2.3). A consequence of this is that ab initio modelling of superalloys is dependent on accurate prediction of both the amount and chemical composition of each phase. Even in approaches to alloy modelling that forgo these expensive simulations, microstructure predictions can still inform the model’s predictions via inclusion as descriptors (see Chapter 5). Alternatively, microstructure features can be directly included as design criteria [8, 10, 19, 20, 25].

Calculation of Phase Diagrams (CALPHAD) describes a broad set of methodologies for computing the concentration-dependent phase mixture in alloys³. It is an equilibrium thermodynamics approach that uses a free energy model for each phase to explore equilibrium properties [67–69]. This is an inverse problem approach to fitting experimental phase composition data [70]. The basic principle is this; Gibbs free energies of mixing for different (combinations of) elements are inferred from available experimental data, and are then used to calculate convex hull diagrams for new combinations of elements. The challenging part is finding an appropriate mathematical form for the Gibbs free energy. Doing this for different crystal structures makes it possible to extrapolate phase stability to materials with new combinations of elements [67, 69]. CALPHAD is a well established technique with a dedicated journal and commercially available databases/software to carry out the calculations, such as Thermo-Calc [71]. There is also an open source implementation of the calculation methods—OpenCalphad—but few open source databases [72].

The free energy models that underlie CALPHAD can incorporate results from atom-

³Arguably, the phase chemistry models in Chapters 4 & 5 fall under the CALPHAD umbrella.

istic simulations, potentially improving their transferability [70, 73]. However, traditional CALPHAD methods do not calculate uncertainties, so users cannot understand how trustworthy a given prediction is, which limits the usefulness of their predictions. Recent work by Attari *et al* attempted to address this issue by using a Markov Chain Monte Carlo approach to work out the parameter values in a CALPHAD model, and hence infer uncertainties within a Bayesian framework [74].

Another limitation of CALPHAD is its basis in equilibrium thermodynamics. The fronts of metallurgy textbooks are always crammed with alloy phase diagrams—and they do provide important starting points for understanding for understanding a given alloy system. However, alloys fundamentally exist out of equilibrium, including making use of out-of-equilibrium phases. The canonical example is the martensitic transformation that occurs when steels are quenched in their austenite phase; the resulting crystal structure, Martensite, is not even a stable equilibrium phase. In superalloys, multi-stage heat treatments are applied to control both the microstructure’s morphology and composition [33]. CALPHAD’s free energy approach cannot easily incorporate such non-equilibrium effects.

2.2.2 Nickel superalloy metallurgy

As discussed above, the reason nickel superalloys are so technologically important is due to their thermomechanical properties at elevated temperatures. In particular, their high creep strength and anomalous rising yield stress have been highlighted. Both of these properties are related to the nature of plastic deformation in superalloys; a mechanism that in turn arises due to physics that spans multiple lengthscales. But the ultimate origin lies in atomistic physics that occurs in both the γ and γ' phases, and in both cases is largely driven by the nucleation and motion of defects.

Defects

The possible crystallographic defects that can arise in an alloy can be classified according to their dimensionality; point, linear, planar, and bulk defects. Each type of defect can arise in different forms. These will be treated one-by-one.

- *Point defects* Interstitial atoms are point defects that occur off-lattice, and play an important role in some alloys—but not superalloys, in which alloying elements are typically substitutional. Of course, these substitutions also constitute another type of point defect since they break the symmetry of the underlying lattice. In ordered crystals, like L1₂, a lattice site occupied by an atom of the ‘wrong’ species is a so-called antisite defect.

Yet another point defect is the lattice vacancy. Their motion leads to solid diffusion; when induced by an applied stress, this is one of the main mechanisms by which

creep occurs.

- *Linear defects* This important class of defect is topological in nature: in fact, it can be shown that line defects in a 3D crystal must be described by a homotopy group equivalent to the group of translations between the Bravais lattice vectors [75]. This means each defect is characterised by a vector: this is called the Burger's vector. These line defects are properly referred to as *dislocations*⁴.

The stress-induced motion of dislocations leads to the other main type of creep deformation, dislocation creep. This is discussed in further detail for superalloys in the subsequent paragraphs.

- *Planar defects* Unbounded planar defects separate the domain of the crystal in two: grain boundaries would be an example of such a defect. Planar defects can also be bounded by dislocations (creating a ribbon-like structure), and such defects play an important role in both the fcc and L1₂ systems.
- *Bulk defects* Clustering effects of either vacancies, or certain atomic species. These include mesoscale defects such as cracks or pores, as well as the formation of precipitates.

Both *diffusion creep* and *dislocation creep* are relevant for nickel superalloys—just how relevant depends on the stress and temperature regime of the creep conditions [3]. When diffusion creep occurs through the interior of a grain (Nabarro-Herring creep), vacancies move down the chemical potential gradient caused due to applied stresses [76]. Evidently, the concept of a physical vacancy only really makes sense in a phase with long-range order, and the disappearance of long-range order at the melting temperature T_m can be understood as the onset of mass-transport via random kinetic motion. Hence, the Nabarro-Herring creep mechanism dominates at high homologous temperatures (T/T_m). Another mechanism for diffusion creep is mass transport via grain boundaries (Coble creep), which can occur at slightly lower temperatures. Eliminating this effect is precisely what motivated the development of single crystal superalloys [3].

Dislocation creep occurs when dislocations *slip* due to an applied stress. Slip occurs along the Burger's vector of a dislocation—the slip plane must also contain the dislocation line's vector. In an fcc crystal, the most favourable slip system corresponds to the shortest possible Burger's vector, which is $a/2\langle 110 \rangle$, with the close packed plane [1̄1̄1] being the favourable slip plane [3, 77, 78]. Under a harmonic model of atomic interaction, the energy

⁴Technically, this formulation is arrived at by neglecting the rotational symmetry of a crystal. Taking this into account and computing the homotopy group leads to two types of line defects, dislocations and disclinations. See Ref. [75] for details. Other key takeaways are that point defects are purely physical defects, not topological, and that the conventional distinction between edge and screw dislocations is non-topological in nature. In nature, dislocations are typically ‘mixed’, i.e. not wholly screw or edge-type.

associated with a dislocation is proportional to the magnitude of the Burger's vector $\|\mathbf{b}\|^2$; this means the Burger's vector can disassociate into a pair of partial dislocations:

$$\mathbf{b} \rightarrow \mathbf{b}_1 + \mathbf{b}_2 \quad ,$$

such that the topological invariant (i.e. the Burger's vector) associated with the dislocation is conserved, and the total energy is decreased:

$$\begin{aligned} \mathbf{b} &= \mathbf{b}_1 + \mathbf{b}_2 \quad , \\ \|\mathbf{b}\|^2 &> \|\mathbf{b}_1\|^2 + \|\mathbf{b}_2\|^2 \quad . \end{aligned}$$

Here \mathbf{b}_1 and \mathbf{b}_2 are referred to as Shockley *partial dislocations*. The two partial dislocations bound a planar defect. Taken together, the three defects are referred to as an *extended dislocation*. In an fcc crystal system, the following extended dislocation will always be energetically favourable:

$$\frac{a}{2}\langle 110 \rangle \rightarrow \frac{a}{6}\langle 21\bar{1} \rangle + \frac{a}{6}\langle 121 \rangle \quad . \quad (2.12)$$

The planar defect that forms in such an extended dislocation is a stacking fault. This type of defect can come in different forms, and can be understood as a disruption in the stacking order of the close packed crystal planes [3, 79, 80]. The insertion of an extra plane forms an *extrinsic* stacking fault, and the removal of a plane forms an *intrinsic* stacking fault. It is the latter that is formed in an fcc extended dislocation. The close packed $\{1\bar{1}1\}$ planes in fcc stack in a ABCABC... order; an intrinsic stacking fault corresponds to the formation of an ABABAB... order, localised to the layers either side of the defect plane. This extended dislocation and stacking fault are shown in Fig. a2.5. The ABAB... ordering in fact corresponds to the close packed structure of a hcp lattice. This means that a first order approximation to the intrinsic stacking fault energy density is [40, 41]:

$$\gamma_{\text{ISF}} \approx 2(E_{\text{hcp}} - E_{\text{fcc}})/A \quad . \quad (2.13)$$

Here A is the area per atom of the planar fault.

A dislocation with a parallel line and Burger's vector can *cross-slip* onto a different slip plane [3, 77, 81]. This allows dislocations to move around obstacles such as alloying elements. Extended dislocations have to constrict back to a simple line defect in order to cross-slip (the Friedel-Escaig mechanism). This occurs more easily when the energy associated with the stacking fault is high. Hence, dislocations are more readily pinned in fcc alloys with lower stacking fault energies, causing higher resistance to plastic deformation.

The L1₂ system has space group Pm $\bar{3}m$ compared to Fm $\bar{3}m$ for fcc. This means it has a different set of possible Burger's vectors that can characterise its dislocations—and

again, these must be equal to Bravais lattice vectors [75]. Examples are $\mathbf{b} = a\langle 110 \rangle$ or $a\langle 100 \rangle$. As was described above for the fcc system, these dislocations disassociate into partial dislocations that preserve the overall invariant—except in this case they are not true Bravais lattice vectors, and instead correspond to vectors between atomic sites in the crystal’s basis. These are properly called *superpartial dislocations* [3, 49, 54]. In contrast to the fcc system, these disassociations only occur under the influence of mechanical deformation, not thermal conditions [3]. An example would be the following disassociation:

$$a\langle 1\bar{1}0 \rangle \rightarrow \frac{a}{2}\langle 1\bar{1}0 \rangle + \frac{a}{2}\langle 1\bar{1}0 \rangle .$$

The paired superpartial dislocations bound a type of planar defect called an antiphase boundary, which can be thought of as a plane of antisite defects. However, in a similar manner to the formation of the extended dislocation in Eq. 2.12, further disassociations are possible:

$$\begin{aligned} a\langle 1\bar{1}0 \rangle &\rightarrow \frac{a}{2}\langle 1\bar{1}0 \rangle + \frac{a}{2}\langle 1\bar{1}0 \rangle \\ &\rightarrow \frac{a}{6}\langle 2\bar{1}\bar{1} \rangle + \frac{a}{6}\langle 1\bar{2}\bar{1} \rangle + \frac{a}{6}\langle 2\bar{1}\bar{1} \rangle + \frac{a}{6}\langle 1\bar{2}\bar{1} \rangle . \end{aligned} \quad (2.14)$$

This is a *superdislocation*, with each pair of new partials bounding a mixed antiphase boundary/stacking fault (a *complex stacking fault*), which in turn bound an antiphase boundary [3, 54, 82]. This series of dislocations is shown in Fig. 2.6.

When a $\mathbf{b} = a/2\langle 110 \rangle$ dislocation belonging to the fcc matrix phase enters an L1₂ precipitate, it introduces a superpartial dislocation to the precipitate. The superpartial leaves an antiphase boundary in its wake, that can only be cancelled out by the passage of a further, trailing, superpartial dislocation. This pair of dislocations—each a separate extended dislocation in the matrix phase, and taken together a single superdislocation in the precipitate phase—are effectively coupled together. Depending on how their separation compares to the lengthscales of the superalloy microstructure, this coupling is either weak or strong. In either case, an energy barrier associated with the antiphase boundary has to be overcome in order for this precipitate *cutting* to occur [3]. This is the mechanism by which the precipitate phase helps to resist dislocation motion, explaining the significance of the two-phase microstructure—as emphasised in the preceding sections—to the phenomenal strength properties of nickel superalloys.

Dislocation theory can also explain the yield strength anomaly exhibited by superalloys that was mentioned in the introduction to Section 2.2. The superdislocation given by Eq. 2.14, residing on the {111} plane, is the favourable slip system for the γ' phase in nickel superalloys. A thermally activated mechanism for cross-slip of part of the superdislocation ‘ribbon’ onto the {001} plane exists. The segment that moves from the

favourable {111} slip plane onto the non-favourable {001} gets locked in place, hindering dislocation motion. This mechanism is called the Kear-Wilsdorf lock [82]. Due to its thermal activation, it causes the yield stress to rise with temperature, leading to the anomalous yield stress increase exhibited by L1₂ intermetallics, and consequently, superalloys.

Heat treatments

For all commercially used superalloys, a heat treatment is applied after the initial melting of the alloy powder and solidification into a component. The purpose of these heat treatments is to control the morphology and composition of the microstructure, and can be divided into two categories: solution (or homogenising) heat treatments and precipitation/ageing heat treatments. Prior to heat treatment, the alloy is said to be *as-cast*.

A heterogeneous distribution of precipitates is typical in the as-cast superalloy microstructure, which can include typical precipitate sizes varying through the alloy, incoherent precipitate/matrix morphology, and the formation of secondary phases. Additionally, some elements are not distributed evenly throughout the precipitates and segregate strongly to the centre or dendrite arms. The solution heat treatment is used to homogenise the microstructure, and occurs at a temperature between the γ' solvus and solidus temperatures [33]. A typical solution heat treatment is 3 hours at a temperature above 1300°C, with the exact regimen depending on the as-cast alloy composition. This can result in fairly complex heat treatment regimens for commercial alloys with highly inhomogenous as-cast microstructures, such as CMSX-4 and CMSX-10 [83].

After the solution heat treatment further heat treatments are applied to further optimise the morphology of the superalloy microstructure. These heat treatments are typically chosen by alloy designers to improve the thermomechanical properties for a given alloy application. Another consideration is whether these further heat treatments can be combined with the application of a protective coating to the alloy. Microstructure control via heat treatment is a non-equilibrium thermodynamic process that naturally effects the precipitate fraction and phase chemistry along with the phase morphology [84–89].

Experimental metallurgy

The microstructure of superalloys are experimentally determined via a range of different techniques. The morphology of superalloys—that is the mesoscale grain structure of the two phases—with a typical characteristic scale of ~ 400 nm, is typically studied directly using transmission electron microscopes (TEM), scanning electron microscope (SEM), or scanning transmission electron microscopes (STEM) [85, 90–101]. The composition of the different phases of the alloy (the microchemistry of the alloy) can be determined in a variety of different ways. Direct methods to determine the composition of each phase

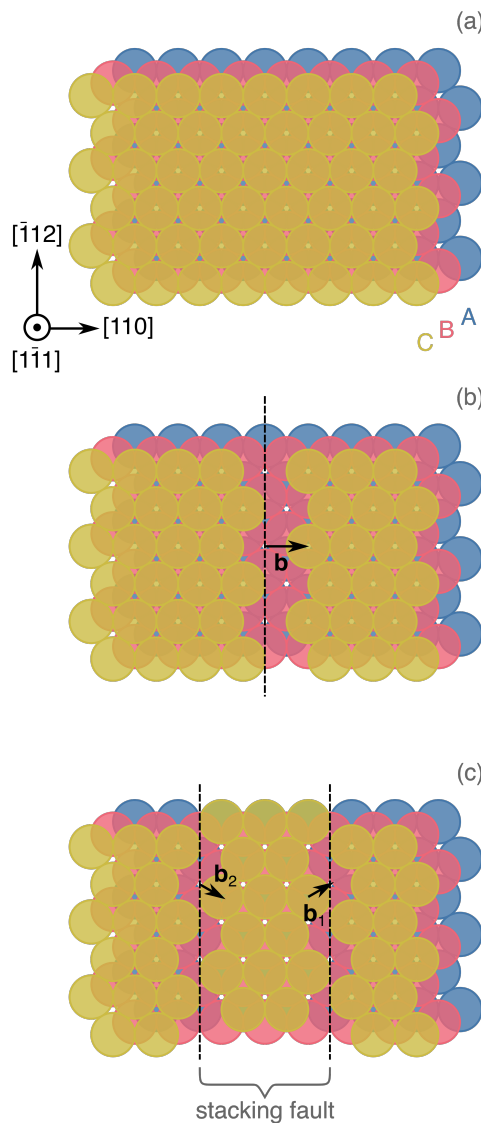


Figure 2.5: Dislocations in an fcc crystal lattice; (a) the defect-free lattice structure in the close-packed direction $(1\bar{1}\bar{1})$, showing the ABC stacking pattern, (b) a dislocation with Burger's vector $\mathbf{b} = a/2[110]$, (c) the disassociation of a dislocation into two partial dislocations bounding a stacking fault.

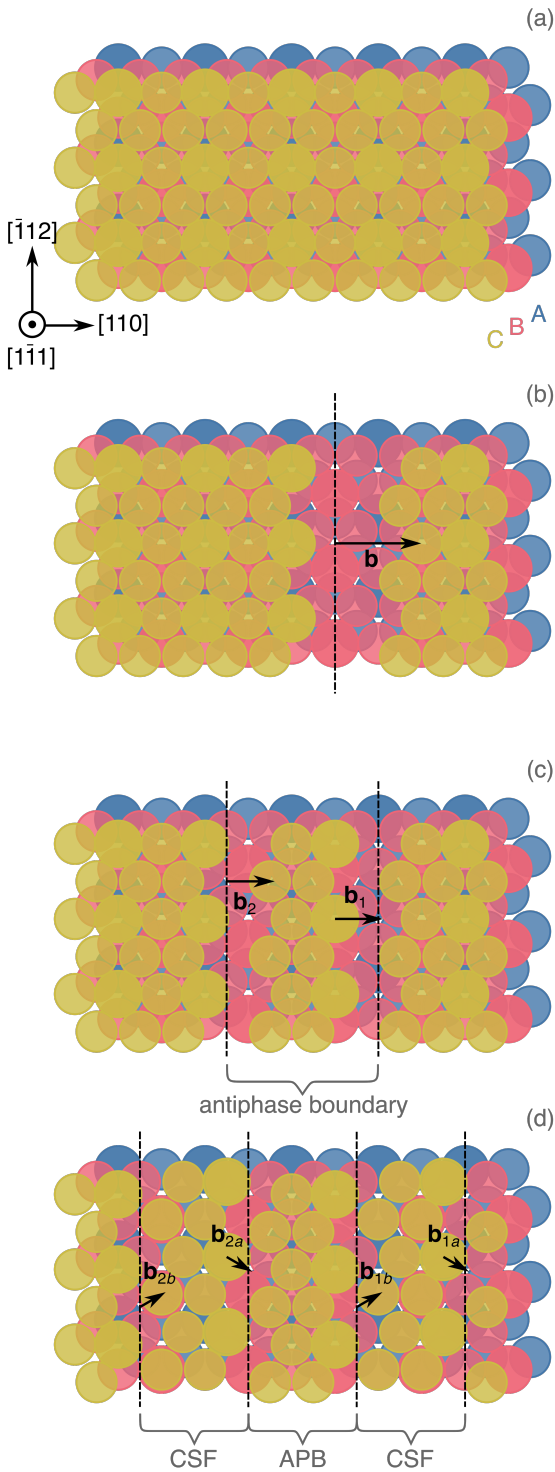


Figure 2.6: Dislocations in an L1₂ crystal lattice; (a) the defect-free lattice structure in the close-packed direction (111), showing the ABC stacking pattern, with Al-site atoms shown as larger and darker than Ni-site atoms, (b) a dislocation with Burger's vector $\mathbf{b} = a[110]$, (c) the disassociation of a dislocation into two superpartial dislocations bounding an antiphase boundary stacking fault, (d) a further disassociation into superpartial dislocations, with an antiphase boundary (APB) defect now sandwiched between a pair of complex stacking faults (CSF).

are atom probe tomography (APT) and atom probe field ion microscopy (APFIM) [84, 87, 95, 102]. The use of APT in the study of superalloys, including the determination of phase composition, has been reviewed by Miller in 2001 [103]. X-ray TEM has also been used as an in-situ method to determine phase composition [86, 99, 104].

If not measured in-situ a phase extraction method can be used to separate out the two phases, then their compositions can be analysed. An example of a phase extraction method is electrolytic extraction. Methods used to measure the composition after extraction include inductively coupled plasma atomic emission spectroscopy (ICP-AES) [85], and wet chemical analysis. Tin et al (2004) [30] compared two methods of determining the γ' phase composition: in-situ APT and extracted wet chemical analysis. They found significant discrepancies between the two methods, e.g. finding 2.86 at.% W via the former method and 4.30 at.% W via the latter for the superalloy RR2100. However most authors report compositions determined via a single method. Typically, experimental errors are not reported.

Many of the properties of superalloys that are of interest, such as the creep strength, yield stress, elastic properties, and fatigue life, are measured via standard experimental techniques within metallurgy that will not be covered in detail here. The stacking fault energy is unusual in that it is determined via measurements of the superalloy microstructure. Measurement of the Burger's vector in a strained alloy can be used to calculate the SFE [93, 94, 98, 105, 106].

2.3 Design of superalloys

Following the discussion of the machine learning methodology used in this work (Gaussian process regression), and some aspects of superalloy metallurgy, this section reviews some other approaches to alloy design. For the sake of conciseness this sections focuses only on those methods which have been applied to the design of nickel superalloys. For a more generic review, see Hart et al [107].

Neural networks

Superalloy properties have been predicted using neural networks since the turn of this century [108, 109]. The neural network tool developed by Conduit et al has been used to design a conventional nickel superalloy [10] as well as a superalloy suitable for additive manufacturing [8]. Their approach leverages the fact that machine learning models are agnostic to the nature of the properties they are aiming to predict. This means a single machine learning model—in this case a neural network—can predict many different kinds of properties at once, so long as each property type has its own discrete label which is included as one of the neural network’s inputs. If correlations between these properties exist, the neural network should be able to capture them within its latent space representation of the materials space it is modelling. Conduit et al used a single hidden layer neural network and showed that it was able to form such a latent space representation even when there was a very small number of training examples with measurements of a certain property (~ 10) of interest, but a much larger number (~ 1000) of different training examples with data for a different but related property. They made effective use of this to design a superalloy for direct laser deposition despite only having 10 data entries for processability via this manufacturing method.

In order to optimise an alloy composition to a given set of target criteria \mathbf{t} , Conduit et al made use of the full probabilistic output of their models: the predictions for each property, \mathbf{f}_c , but also the covariance of these predictions, Σ_c . The objective function they used was the log probability of target fulfilment, $\log(p_c)$, where:

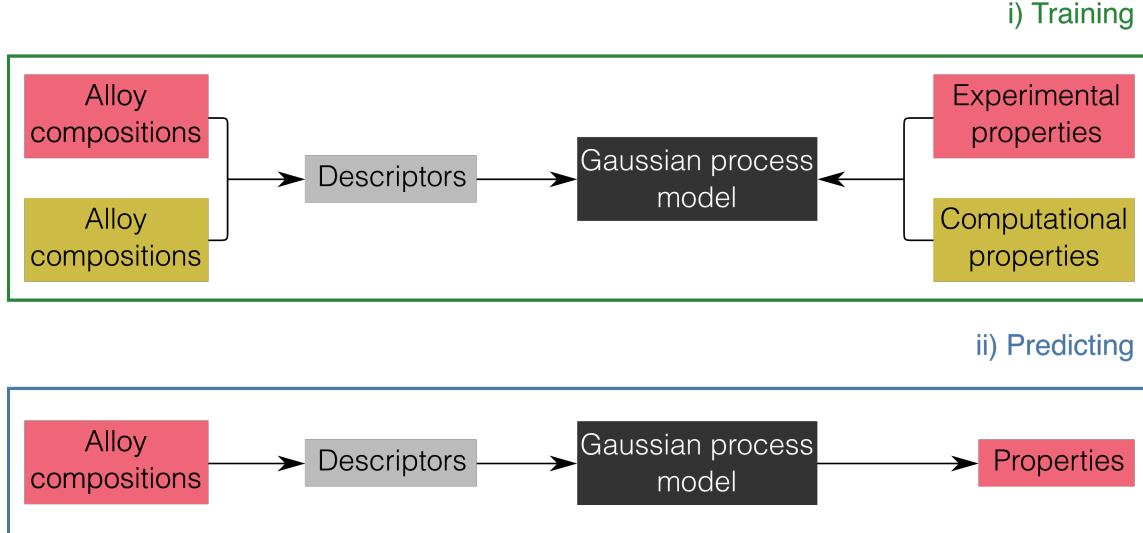
$$p_c = F(\Sigma_c^{-1}(\mathbf{f}_c - \mathbf{t})) \quad . \quad (2.15)$$

Simulated annealing was then used to maximise this quantity [8, 10].

Alloys-by-design

A straightforward computational paradigm for superalloy design is described by Reed et al and called the ‘alloys-by-design’ method [19, 20, 25]. With this method single crystal superalloys were optimised for a single thermomechanical property; creep strength. Constraints were also imposed on the predicted density, cost, and castability of the alloy

a) GPR model



b) Neural network model

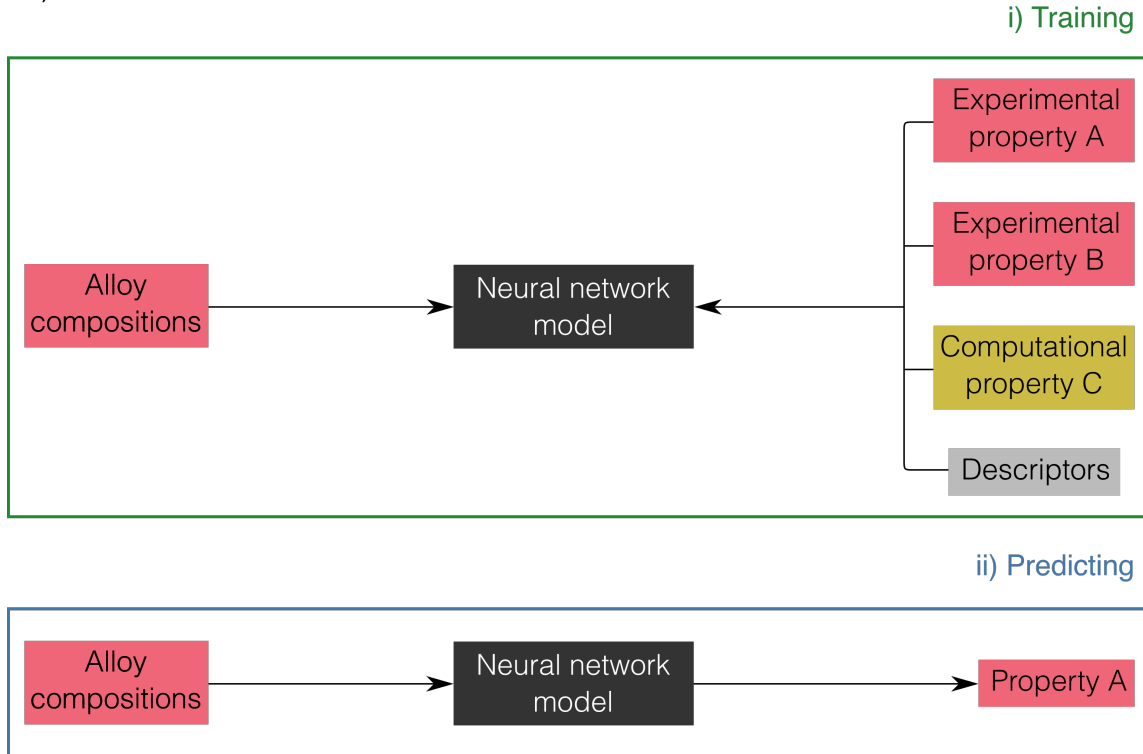


Figure 2.7: A comparison between a) the GPR model approach proposed in this work (see also Fig. 1.2) and b) a neural network approach similar to that used by Conduit et al [8, 10].

in order to ensure the alloy that was designed would meet the requirements for practical commercial usage. Simple physical models were used for these three properties: density was calculated according to a rule of mixtures for the elements present, cost from the weight fraction of each element in the alloy and its cost per kilogram, and castability from a ‘merit index’ for freckle formation. Optimisation for creep resistance was achieved by maximisation of a single merit index for creep, along with consideration of three other properties that promote creep resistance.

Creep occurs by two main mechanisms, diffusion and dislocation motion. In the alloys-by-design method the merit index for creep reflects the influence of the diffusion mechanism only and is calculated as: $M_{\text{creep}} = \sum_i x_i / \tilde{D}_i$, where x_i are the overall fractions of each element in the alloy and \tilde{D}_i are empirically determined interdiffusion coefficients for each element in pure Ni. The other three properties relating to creep that are calculated are associated with the microstructure of the superalloy. These are the γ' fraction, the γ/γ' lattice parameter misfit, and the effective metal-d level of the alloy—an estimate of TCP phase susceptibility. There is a physical basis for using these three properties as they all play a role in the theory of dislocation motion [3, 33]. But they are also three of the simplest properties relating to the microstructure of the superalloy that could be included; the first two are fundamental geometric properties of the γ/γ' morphology, and the TCP susceptibility is the reverse of the chemical stability of the two-phase microstructure. The γ' fraction is found via CALPHAD, as is the composition of each phase, which are used to calculate the respective lattice parameters (from an empirical model based on the effect of each element X on the lattice parameter in the binary Ni-X system) and hence lattice parameter misfit.

The alloys-by-design method does not make use of machine learning techniques to infer the correlation between the various predicted properties and merit indices, and instead relies on manual interpretation of trade-off diagrams. The properties above are calculated for $\sim 100,000$ alloys in an initial compositional space. The compositional space is then narrowed down using constraints on the different properties and consideration of the analysis of the trade-off diagrams, then finally the superalloy’s composition is optimised with respect to the primary property of interest, in this case the creep merit index. Originally applied to single crystal superalloys, the method has also been applied to polycrystalline alloys for use in turbine blades, with different merit indices [20]. Yield stress is the key property of superalloys for use in turbine discs, so a merit index for strength is proposed, $M_{\text{strength}} = \bar{M}^{\frac{1}{2}} \gamma_{\text{APB}} f^{1/2} / b$, based on the theory of precipitation hardening. \bar{M} is the Taylor factor, γ_{APB} is the APBE, f is the γ' fraction, and b is the Burgers vector. The APBE used in this calculation was found from DFT analysis of the APBE of the ternary $\text{Ni}_3(\text{Al},\text{X})$ system, assuming linear superposition of the effect of each ternary element X in the multi-component system [49].

The merit indices used in the Alloys-by-design paradigm influenced the physical

descriptors used in Chapter 5.

Alloy Design Program

The Alloy Design Program was developed at NIMS, Japan, by Harada et al [110, 111]. The program calculates the phase chemistry of a superalloy from its nominal composition using linear regression models of the partitioning coefficients for each element. They define the partitioning coefficients as $K_i = x_i^\gamma / x_i^{\gamma'}$. Superalloy properties, such as creep strength, are then computed from the predicted phase compositions and γ' fraction using further linear regression models. For physical properties of each phase, such as lattice constants, they used a statistical thermodynamics approach called the cluster variation method (CVM), which made use of Lennard-Jones potentials to calculate the enthalpy of mixing between different atoms [112, 113]. Modern versions of the Alloy Design Program has been used to design the TMS-series superalloys [100, 114].

2.3.1 Discussion

Having surveyed other approaches to modelling nickel superalloys, the relative merits of the Gaussian process approach proposed in this thesis can now be assessed—especially compared to the neural network approach that has been employed in similar, previous work [8, 10]. Major differences between the two machine learning algorithms are provided in Table 2.1. The major con associated with Gaussian process regression is it’s poor scaling with the amount of training data, see Section 2.1.1. The sparse Gaussian process regression framework does provide a workaround, at the cost of adding a further hyperparameter and a further (non-Bayesian) approximation [115]. However, due to the small datasets used in this work, training times never posed a major problem, see Sections 4.4 & 5.2.3.

Another advantage of neural networks is their ability to produce very complex models, as seen in the deep learning architectures underlying the most cutting-edge language models and chatbots. But again, the training datasets used in this work are comparatively small and hence this advantage doesn’t really present itself. In fact, the large number of model-related hyperparameters that neural networks have—which allow for their phenomenal model complexity—present as a disadvantage compared to Gaussian processes when it comes to small training datasets. In particular, the number of layers and neurons require careful fine-tuning in order to avoid overfitting [14].

Finally, Gaussian processes have a number of pros that are especially beneficial to the ideas and concepts developed in this work. Their probabilistic theoretical basis leads to intrinsic predictions of rigorously defined uncertainties and covariances. The use of these quantities will be highly developed in subsequent chapters. Furthermore, the interpretability of Gaussian process regression models depends only on the choice of kernel. In fact,

the choice of kernel allows the user to have some control over the interpretability of their models [13]. This will be made use of—in combination with descriptors—in Chapter 5.

Table 2.1: Differences between neural networks and Gaussian processes. *Refers to the computational complexity with respect to the number of training data points N .

	Neural networks	Gaussian processes
Interpretability	via feature importance analysis e.g. SHAP [116]	intrinsic [12, 13]
Hyperparameters	<ul style="list-style-type: none"> • number of layers • number of neurons per layer • learning rate • activation function • weight initialisation algorithm • optimisation algorithm [14] 	<ul style="list-style-type: none"> • choice of kernel • optimisation algorithm [12, 14, 117]
Uncertainty	via bootstrapping [10, 118]	intrinsic [12]
Covariance	via bootstrapping [10, 118]	intrinsic [12]
Scaling*	$\mathcal{O}(N)$ [14]	$\mathcal{O}(N^3)$ $\mathcal{O}(N)$ (sparse GP) [115]

Chapter 3

Superalloy database

3.1 Introduction

Obtaining a suitable dataset is a crucial first step in any machine learning approach. This chapter details the database of nickel superalloys that was constructed as part of this work. All the data was taken from other open-source datasets [3, 22, 30–33, 83–89, 91–99, 104–106, 110, 114, 119–170]. Much of it was gleaned from academic literature; other sources include datasets compiled by different researchers and industry bodies. The data taken from research papers was acquired manually; some of the data was extracted from plots and figures using WebPlotDigitizer [171].

This chapter starts with summary statistics of the database, and an overview of how it was compiled, then discuss some details of the pre-processing that was applied to it. Finally, some of the machine learning tools that will be developed in later chapters are used to validate the quality of the database.

3.2 Database summary

The basic structure of the database is that each row corresponds to a different alloy, and each column to a different property. Alloys / row entries are distinguished by composition *and* applied heat treatments. In total, the database has 1337 rows with 45824 separate entries (i.e. distinct pieces of information) spanning all the rows and columns. As the database comprises of nickel superalloys, which mostly have a multi-phase microstructure, phase chemistry data is treated a bit differently in the database to other properties. Where composition data exists for a constituent phase of a superalloy, it gains its own row entry. Each row is flagged as representing either a ‘parent’ alloy or a ‘child-phase’. Parent alloys are tied to their child-phase via unique tags generated for each row entry. The motivation for choosing this representation of multi-phase alloys was an assumption that (at least some) child-phases would also constitute stable alloys, and could hence be

Figure 3.1: A screengrab of a portion of the database in spreadsheet format.

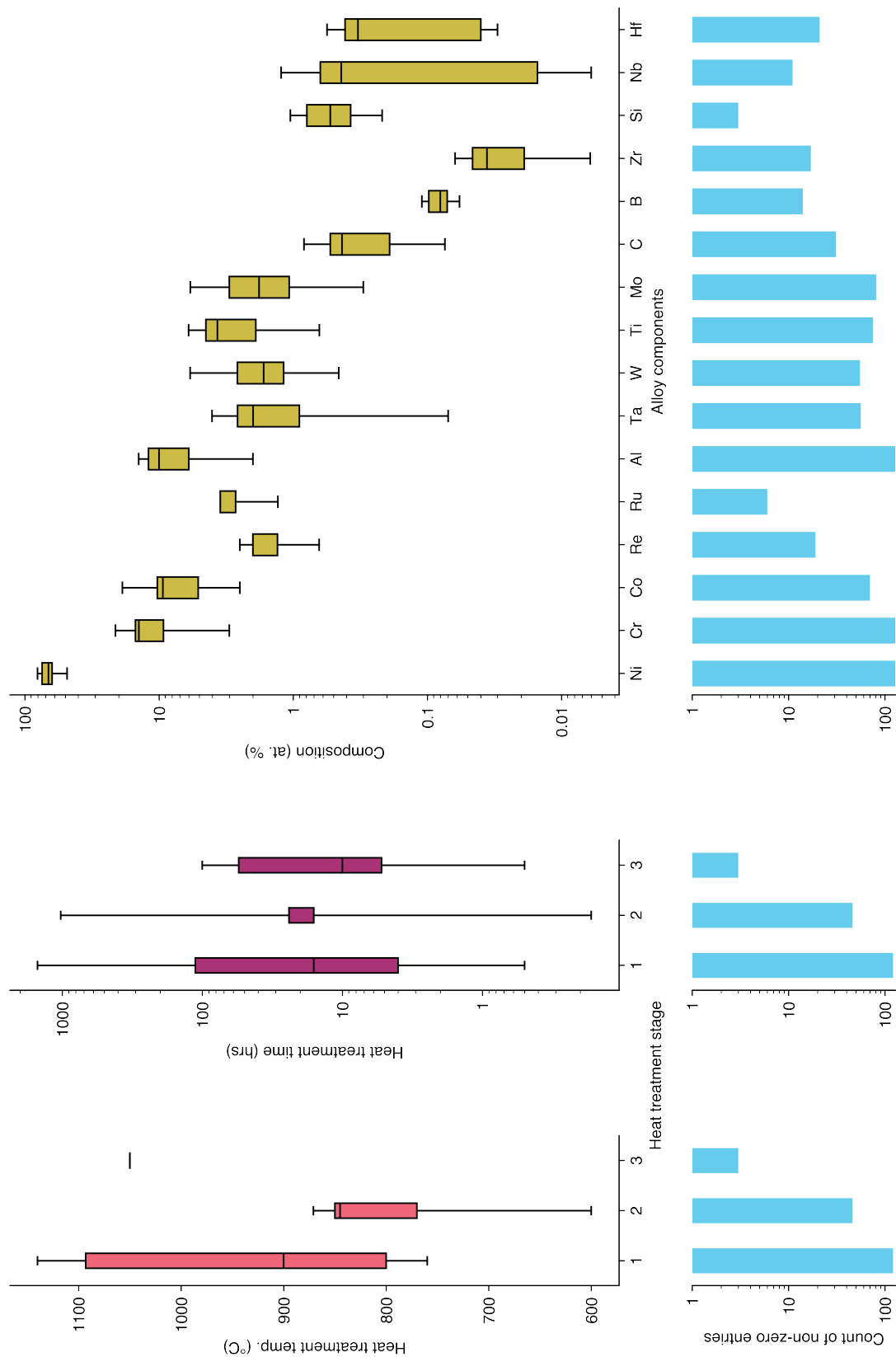


Figure 3.2: Box plots representing a portion of the database: the alloy compositions and heat treatments which have corresponding complete phase chemistry data. The bars descending below each boxplot represent the number of non-zero entries in the database for each component.

used on an equal footing to the parent alloys in certain machine-learning tasks¹. Based on this, other microstructure data was entered exclusively for the parent alloys; this included phase fractions and electron micrographs of phase morphology. Phase chemistry data is summarised using box plots in Fig. 3.2: for the sake of brevity, only the parent alloys, and only those with complete entries for both corresponding phase compositions and fractions, are summarised in the graph. This data formed the inputs to the machine learning models for microchemistry developed in Chapters 4 & 5 (data citations: [30–33, 85–87, 89, 95, 106, 110, 119, 124–127, 129, 130, 135, 137, 138, 141, 142, 146, 151, 152, 154, 155, 158, 160, 161, 164, 165, 167]). In total, there were 128 such entries. The distribution between different casting methods is shown in Fig. 3.3.

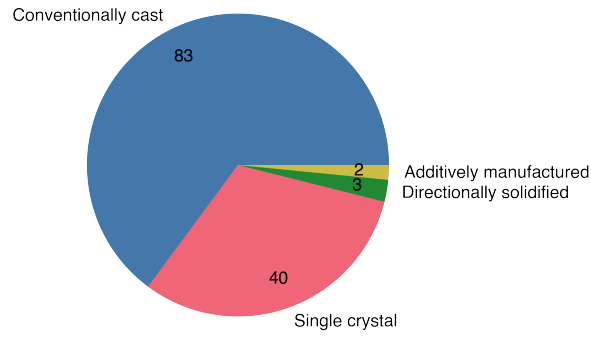


Figure 3.3: Distribution of different casting methods for superalloys in the phase chemistry subset of the database.

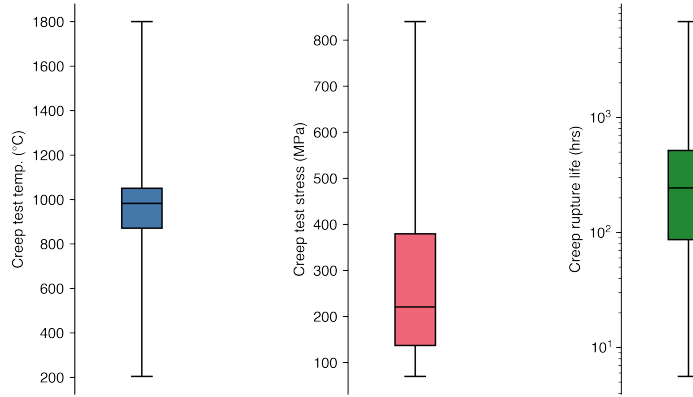


Figure 3.4: Box plots summarising the creep rupture life data for single crystal superalloys in the database. There were 388 total data points spanning 322 distinct alloys.

Other properties compiled in the database are summarised in Fig. 3.4 and Table 3.1. In Chapter 5, the creep rupture life of single crystal superalloys is modelled. This subset of the creep strength data is depicted graphically in Fig. 3.4 (data citations: [33, 83, 88,

¹An example of this type of task would be classification based on crystal structure, e.g. Ref. [172]

Table 3.1: A summary of the properties in the database. No types of superalloy have been excluded from each property summary (compare for Fig. 3.4.)

Creep strength properties				Tensile strength properties				Electron micrographs
Time for 1% creep (hrs)	Rupture life (hrs)	Elongation (%)	Yield stress (MPa)	UTS (MPa)	Elongation (%)			
Total count	81	555	93	148	159	131		361
# of alloys	43	355	51	38	35	32		240
Min value	0.5	5.6	5.3	170	130	1.5	-	-
Median value	72.5	164.7	13.5	815	940	7	-	-
Max value	833	10,000	41	1185	1894	50	-	-
Temp. range (°C)	750 — 1150	204 — 1800	750 — 1150	RT — 1093	RT — 1093	RT	RT	RT
Stress range (MPa)	100 — 840	34 — 840	100 — 840	- —	- —	-	-	-
Phase transition temperatures				Other properties				
Solidus (°C)	Liquidus (°C)	γ' solvus (°C)	Density (g/cm³)	Lattice misfit (%)	SFE (mJ/m²)			
Total count	57	57	50	93	48	41		
# of alloys	57	57	50	93	48	35		
Min value	1139	1290	800	7.75	-1.420	9		
Median value	1305	1365	1125	8.60	-0.023	30		
Max value	1390	1420	1330	9.21	0.876	140		
Temp. range (°C)	-	-	-	-	-	-	RT	- 1050

89, 93, 94, 96, 124, 131, 133–135, 139, 144, 152, 156, 162, 168]). Other creep strength properties are summarised in Table 3.1. Note that in this table, no alloy types have been excluded, e.g. the creep rupture life summary includes both single crystal superalloys and other castings. As discussed in Section 2.2.2, in the literature it is almost always found that both phase chemistry data and other data is reported without errors: as a result no error data is included in the database. Section 2.2.2 also discusses different methods used in experimental data collection: due to scarcity of data (especially for phase chemistry data), measurements obtained via different experimental techniques are included without prejudice.

3.3 Pre-processing

The microstructure GPR models in Chapters 4 & 5 train on *complete* microchemistry data. In the simplest (two-phase) approximation this is the overall superalloy composition, the composition of the matrix (γ) and precipitate (γ') phase, and the fraction of each phase in the alloy. As discussed both above and in Section 2.2.2 there is a great deal of variety in the experimental methods used, particularly those used to measure the microstructure of the superalloys. Some authors report direct measurements for each of these properties, but more often one of these properties is missing. Fortunately, the remaining property can be calculated using the equation:

$$x_i = f x_i^{\gamma'} + (1 - f) x_i^{\gamma} \quad , \quad (3.1)$$

where x_i is the fraction of the i th element in the alloy, $x_i^{\gamma'}$ and x_i^{γ} are the fractions of the same element in the γ' or γ phase respectively, and f is the precipitate fraction for the superalloy. Note that this equations reappears in Chapters 4 (Eqs. 4.2–4.4) & 5 (Eqs. 5.2–5.4): in each instance in discussions of the outputs of the GPR microchemistry models. If f is the missing property it can be calculated via a linear best-fit to the phase compositions 3.1 [154, 158]:

$$f = \frac{\sum_i (x_i - x_i^{\gamma}) (x_i^{\gamma'} - x_i^{\gamma})}{\left(x_i^{\gamma'} - x_i^{\gamma} \right)^2} \quad . \quad (3.2)$$

The same result can be obtained with a Bayesian approach (and the assumption that the phase fraction is a normally distributed variable); this approach also yields an associated

uncertainty:

$$\sigma_f^2 = \frac{\frac{1}{n} \sum_i \left(x_i - f x_i^{\gamma'} - (1-f) x_i^{\gamma} \right)^2}{\sum_i \left(x_i^{\gamma'} - x_i^{\gamma} \right)^2} . \quad (3.3)$$

Calculated phase fractions with uncertainties $\sigma_f > 10\%$ were excluded from the database.

It is important to note that these equations assume there are just two phases in the superalloy ($f_{\text{precipitate}} + f_{\text{matrix}} = 1$), therefore neglecting the small mass fractions of carbides and borides that are present in many superalloys. It also assumes that there is no ‘loss’ when the phases segregate, i.e. that starting from the nominal composition of the alloy $\{x_i\}$, the melting process causes every atom of every element to partition into the bulk of one of the two phases. This might seem trivial but some atoms overwhelmingly partition to grain boundaries and will not be detected by all of the measurement techniques discussed in Section 2.2.2 [3, 33]. In addition, other phases can be present within the superalloys in non-negligible quantities, particularly the TCP phases. Whilst commercial superalloys are typically optimised to contain a minimal amount of TCP material, not all of the superalloys in the database are products of this degree of design optimisation [17, 20, 21, 132, 173]. In the next section, the quality of this inferred microchemistry data is validated using the ML tools developed in the later chapters.

Another inconsistency in the literature which can lead to errors in the database is the format of the values. The composition fractions x_i , x_i^{γ} , $x_i^{\gamma'}$ are reported as either the atomic percentage (at. %) or mass percentage (wt. %). These can easily be converted between using the various elements’ respective atomic masses. The precipitate fraction however is reported as the wt. %, at. %, or volume percentage (vol. %). It is not possible to easily convert vol. % to either of the other formats, but it can be related to the atomic percentage as follows:

$$\begin{aligned} f_{\text{vol}} &\equiv \frac{V^{\gamma'}}{V^{\gamma'} + V^{\gamma}} \\ &= \left(\frac{V^{\gamma}}{V^{\gamma'}} + 1 \right)^{-1} \\ &= \left(\frac{1-f}{f} \left(\frac{a^{\gamma}}{a^{\gamma'}} \right)^3 + 1 \right)^{-1} . \end{aligned} \quad (3.4)$$

Here V and a denote the volume and lattice constant of the respective phases. Writing the lattice constants of each phase as $a^{\gamma} = (1 + 1/2 \delta) \bar{a}$ and $a^{\gamma'} = (1 - 1/2 \delta) \bar{a}$, where $\bar{a} = 1/2(a^{\gamma} + a^{\gamma'})$ is the mean lattice constant and δ is the lattice misfit, conventionally

defined as [21, 124, 155]:

$$\delta = 2 \frac{a^{\gamma'} - a^{\gamma}}{a^{\gamma'} + a^{\gamma}}, \quad (3.5)$$

it is possible to expand Eq. 3.4 as:

$$f_{\text{vol}} = f(1 + 3\delta(1 - f)) + \mathcal{O}(\delta^2) \quad . \quad (3.6)$$

Since typically $|\delta| << 1\%$, (see Table 3.1) the volume and atomic precipitate fraction are equal to within a very small error. This approximation was used to fill out the database.

3.4 Database validation

As well as making predictions, machine learning regression models can also be used to test the quality of a given dataset. This technique makes use of the uncertainties that ML regression models output alongside each prediction [174]. The basic idea is to compare prediction errors with those predictions' uncertainties; if the true value lies far outside of the uncertainty region for a given prediction, it suggests that the associated database entry could be erroneous. Other affects could contribute to this: for example, in instances where the ML model is extrapolating, it could be that its latent space representation of the input space is over-simplified, leading to an ‘over-confidence’ effect. Such cases can be seen in some of the results in the subsequent chapters, e.g. a few of the outlying data points² in Figs. 4.3 & 4.4 in Chapter 4. In this Section, an ML model quality metric (the DUQ) developed in the subsequent chapter is used for validation analysis. It will be seen that this approach can help disentangle the overlapping effects of *model quality* from the effects of *database quality*.

In this section, database validation is carried out to determine the quality of the pre-processing used to infer additional phase chemistry data, as described in Section 3.3.

3.4.1 Using the distribution of uncertainty quality for validation

The distribution of uncertainty quality (DUQ) is developed in Section 4.3.1. It assigns a value between 0 (best) and 1 (worst) to the ‘quality’ of an uncertainty prediction. Combining this with a qualitative analysis of the resulting histograms of the residual to uncertainty ratio, it is possible to assess the extent to which different models are over- or under-predicting uncertainties. The DUQ can also be calculated for different subsets of a single model’s predictions.

²Note that all of these overconfident outliers were investigated by returning to the original data sources and checking for data quality or transcription mistakes.

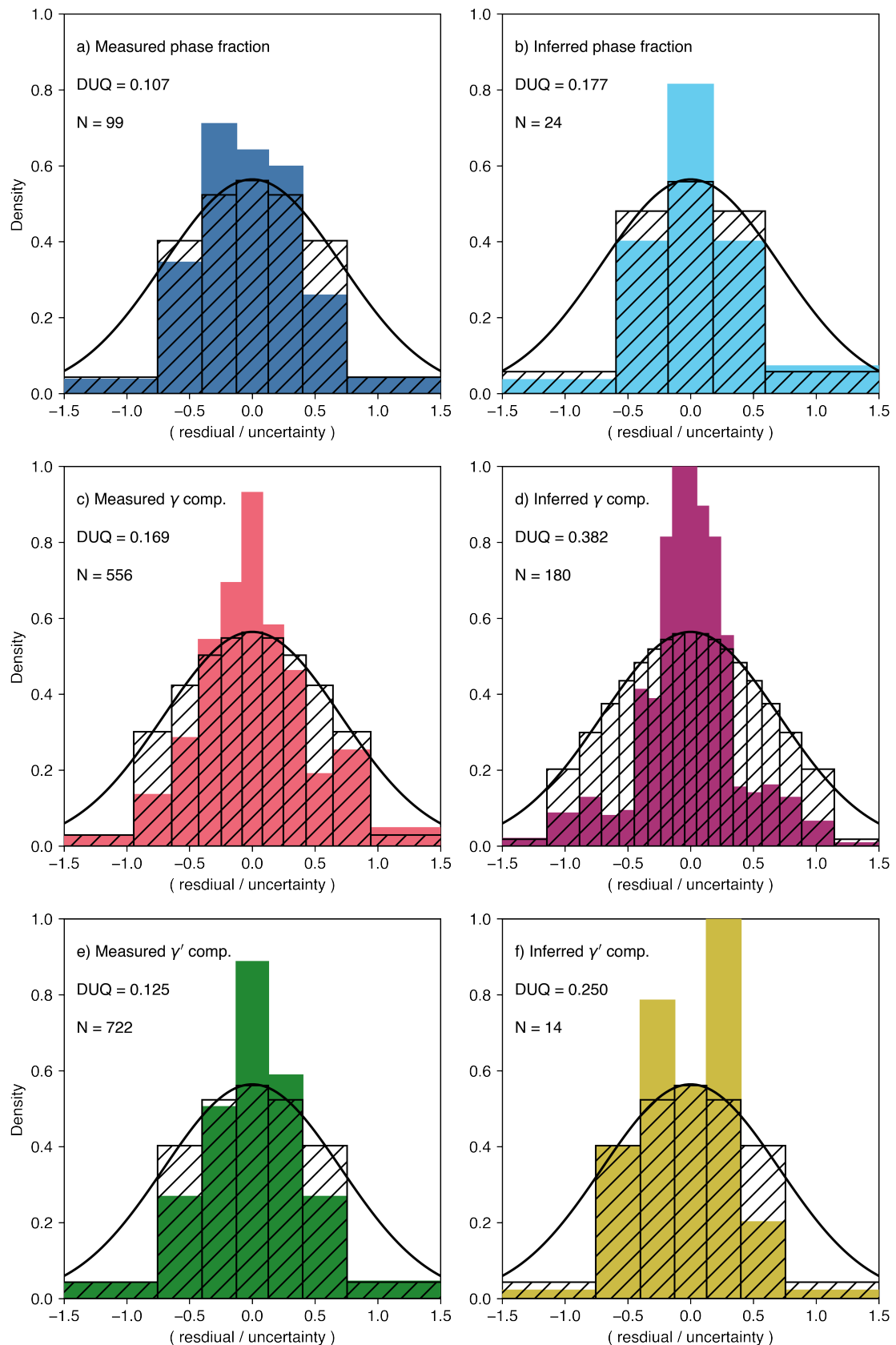


Figure 3.5: DUQ histograms for subsets of the phase chemistry predictions.

Table 3.2: Statistical comparison between alloys with measured/inferred γ' phase fractions.

	Measured	Inferred
γ' phase frac. median	0.40	0.61
γ' phase frac. std	0.22	0.16
% commercial alloys	34	88

In order to validate the quality of the inferred phase chemistry data, the predictions from the phase chemistry model trained via 10-fold cross-validation in Chapter 5 were taken and split into two subsets depending on whether the respective predicted data points were directly measured or inferred. For each subset, the DUQ was calculated and the associated histogram plotted. This analysis was carried out for all three GPR models (precipitate phase fraction, γ phase compositions, γ' phase compositions); the histograms for each subset of each model are shown in Fig. 3.5.

In each case, the DUQ is higher for predictions of the inferred subset. However, the associated histograms reveal that for the inferred subsets, the uncertainties are in fact being overestimated, as characterised by the narrower distributions. The only exception is the inferred γ' compositions, however there are only $N = 14$ data points so this result is less significant. Digging into the statistics for the precipitate phase fractions and γ phase compositions, it is evident that some key statistics reflecting the types of alloy with measured/inferred values differ greatly. In Table 3.2, it can be seen that the alloys with inferred phase fractions are overwhelmingly ‘commercial’ superalloys, which here means superalloys that have been designed for practical applications (as opposed to superalloys that have been designed for the purpose of experimentation). These superalloys typically have similar γ' phase fractions with high values, although they can have great variety in their compositions, especially the number and diversity of components. In effect, the target space volume for the inferred fraction superalloys is smaller, whereas their input (composition) space is just as large (or larger) as for the measured fraction superalloys. This leads to the uncertainty overestimation effect.

Similar analysis for the alloys with inferred γ phase compositions is shown in Table 3.3. Here the statistics are reversed: the alloys with inferred γ compositions are less likely to be high phase fraction commercial alloys. These alloys with simpler overall compositions also have simpler γ phase compositions, which again produces an overestimation effect. In Fig. 3.6 precipitate fraction residual:uncertainty ratios are plotted against the precipitate fraction values. Across the entire range of values, the most notable outliers in fact have measured, not inferred fraction values. This analysis confirms that pre-processing described in Section 3.3 does not produce erroneous database entries.

Table 3.3: Statistical comparison between alloys with measured/inferred γ phase compositions.

	Measured	Inferred
γ' phase frac. median	0.49	0.23
Mean # commercial alloys	6.5	4.9
% commercial alloys	53	24

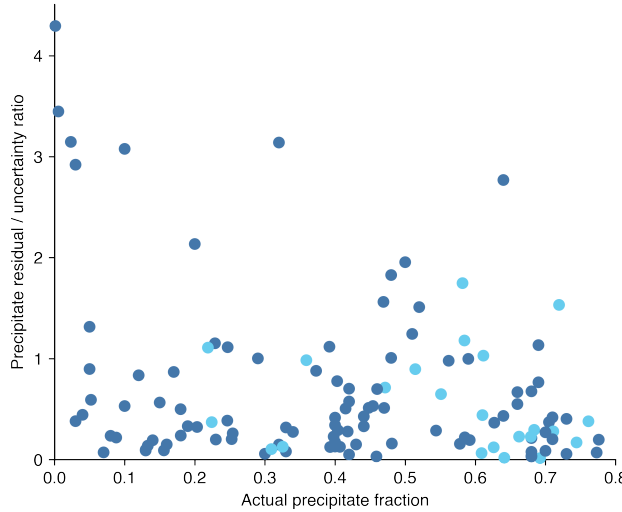


Figure 3.6: A plot of the ratio of precipitate fraction residuals to uncertainties ($|f - \hat{f}|/\sigma_f$) versus the actual precipitate fractions. Dark blue points are alloys with measured phase fractions, light blue those with inferred values.

3.5 Conclusion

This chapter has described how a substantial database of superalloy properties was compiled. In order to fill out the phase chemistry data in the database, pre-processing was carried out. This pre-processing step relied on simple assumptions about the constraints on alloy microchemistry. In order to verify the validity of this procedure, the machine learning tool developed in Chapter 5 was deployed on the database. The resulting analysis confirmed that, taking prediction uncertainty into account, the entries with inferred values did not overwhelmingly constitute outlier predictions when compared to entries with measured values. With a database constructed and validated, it is possible to proceed with the development of the machine learning models in subsequent chapters.

Chapter 4

Machine learning predictions of superalloy phase chemistry

Abstract

Gaussian process regression machine learning with a physically-informed kernel is used to model the phase compositions of nickel-base superalloys. The model delivers good predictions for laboratory and commercial superalloys, with $R^2 > 0.8$ for all but two components of each of the γ and γ' phases, and $R^2 = 0.924$ (RMSE = 0.063) for the γ' fraction. For four benchmark SX-series alloys the methodology predicts the γ' phase composition with RMSE = 0.006 and the fraction with RMSE = 0.020, superior to the 0.007 and 0.021 respectively from CALPHAD. Furthermore, unlike CALPHAD Gaussian process regression quantifies the uncertainty in predictions, and can be retrained as new data becomes available.

This chapter was published as Taylor, P. L. & Conduit, G. Machine learning predictions of superalloy microstructure. *Computational Materials Science* **201**, 110916 (Jan. 2022) [1].

4.1 Introduction

As discussed in Section 2.2, first-principles modelling of superalloys is dependent on accurate prediction of both the amount and chemical composition of both the matrix (γ) and precipitate (γ') phases. Two main methods are used to understand the phase chemistry: physical modelling and curve-fitting. Physical modelling approaches are discussed in Section 2.2.1—the focus of this chapter is on the curve-fitting approach.

The principle curve-fitting approach is the Calculation of Phase Diagrams (CALPHAD) methodology [71, 72]. CALPHAD is an equilibrium thermodynamics approach that uses a free energy model for each phase to explore equilibrium properties [67–69]. This is an inverse problem approach to fitting experimental phase composition data [70]. Consequently the advantage of CALPHAD over other curve-fitting methods is anticipated to be the reproduction of sensible physical limits when extrapolating beyond the range of the training data. However, traditional CALPHAD methods do not calculate uncertainties, so users cannot understand how trustworthy a given prediction is, which limits the usefulness of their predictions. Recent work by Attari *et al* attempted to address this issue by using a Markov Chain Monte Carlo approach to work out the parameter values in a CALPHAD model, and hence infer uncertainties within a Bayesian framework [74]. Another curve-fitting method is the Alloy Design Program developed at NIMS, Japan, by Harada *et al*. The program calculates the phase chemistry of a superalloy from its nominal composition using linear regression models of the partitioning coefficients for each element, and was used to design the TMS-series superalloys [100, 110–114].

Machine learning (ML) is a new approach to curve-fitting data that has recently gained prominence in materials science. The focus has been on using ML to predict the macroscale properties of superalloys, so that the ML models can be used to design new alloy compositions to a given design criteria [8, 10, 19, 20, 108, 109, 175–178]. A wide range of ML approaches have been used, including neural networks and Gaussian process regression (GPR). Other researchers have applied ML to predicting different aspects of superalloy microstructure such as the lattice misfit [179]. Yabansu *et al* used GPR to predict the evolution of the microstructure morphology with ageing, taking as input the time and temperature of the ageing heat treatment [180]. The ML approach is appealing as it can not only address all materials properties, but also estimate the uncertainties in its predictions [100, 181].

In this chapter the best of physical-based methods and machine learning are combined. Our approach is to develop a GPR model with a physically-informed kernel to capture the underlying physical principles. First, a training database is compiled from the freely available scientific literature. Then, the framework of the GPR model used to predict the chemical composition and fractions of each phase is described, including a novel kernel devised to encapsulate some basic physical principles of alloy systems. The

predictions of the GPR model are then initially compared to experimental values before being compared with CALPHAD results on a selection of four experimentally measured SX-series superalloys proposed in Ref. [161] as an uncertainty benchmark.

4.2 Data processing

Machine learning requires data to train on. For this reason it is necessary to compile a database that is drawn from both laboratory and commercial superalloys: with each entry encapsulating information for both the features that the ML method will take as inputs and also the properties that it will predict as outputs. The database used in this work is described in detail in Chapter 3. Each row in said database is a different superalloy. The columns are the alloy's descriptors comprising of composition $\mathbf{x}_c = [x_1, \dots, x_n]^T$ (at. %), ageing heat treatment $\mathbf{x}_h = [x_1^{\text{HT}}, \dots, x_{2m}^{\text{HT}}]^T$, and also its properties that are the components of both the alloy's γ ($\mathbf{x}^\gamma = [x_i^\gamma]^T$) and γ' ($\mathbf{x}^{\gamma'} = [x_i^{\gamma'}]^T$) phases and also the γ' phase fraction f . Since the composition must sum to one, a reduced description $\mathbf{x}_c \mapsto \bar{\mathbf{x}}_c = [x_2, \dots, x_n]^T$ could be used. However principal component analysis (Fig. 4.1) showed that low rank projections of \mathbf{x}_c had more explanatory power than the same rank projections of $\bar{\mathbf{x}}_c$ (blue and red line respectively in Fig. 4.1). For this reason the full set of descriptors were used throughout. The work in this chapter focuses on pure γ/γ' alloys and therefore circumvent consideration of any carbides and secondary phases that could form [3, 17, 20, 21, 33, 132, 173].

Heat treatments are applied to superalloys to control the microstructure morphology, and can be classed as either a solution heat treatment or a precipitation/ageing heat treatment. The solution heat treatment homogenises the microstructure so its temperature and duration is dictated by the superalloy composition [33, 83, 89]. Therefore, in the framework of this model, the solution heat treatment is considered as a property of the overall alloy composition, rather than as an input parameter. Next, ageing heat treatments are applied to further optimise the morphology of the superalloy microstructure. Six features describe the ageing heat treatment: a heat treatment temperature and time, for up to three heat treatment stages per alloy. For alloys with fewer total stages, the remaining ones are specified as being at room temperature for no time. Cooling rates are not included as inputs due to the scarcity of available data; typically, in the experimental literature used to construct the dataset, it is simply specified that the samples were air-cooled after heat treatment. Note that, since the solution heat treatment is not being considered as an input, the fully-solutioned state should be considered the baseline for the model's output; i.e. an input with three null heat treatments corresponds to making phase chemistry predictions for that alloy composition after it has undergone its correct solution heat treatment.

The database used in this chapter is a prototype of that described in Chapter 3.

It comprises 97 experimental superalloy phase fractions and compositions, of which 36 entries correspond to laboratory alloys, 43 to commercial (or modifications of) single-crystal superalloys, and 18 to other commercial polycrystalline superalloys. All of these entries contained both Ni and Al. Other elements occurred in a subset of database entries, between 86-times for Cr to just 5-times for Ru [30, 33, 84–89, 91, 92, 95, 96, 98, 99, 104, 106, 110, 119, 123, 124, 127–129, 131, 139, 142, 145, 146, 148, 152, 155, 158, 159, 161, 165, 166]. See Table 4.1 for a full overview including summary statistics. In order to make the training procedure as robust and user-friendly as possible, no outliers were filtered from the dataset before use in the ML model.

4.2.1 Data parameterisation

With the data curated, the next step is to reparameterise it to both capture underlying physics and also to make it more amenable to machine learning. To express the phase composition logarithmic partitioning coefficients P_i are adopted, P'_i [30, 92, 99, 104, 106, 110, 111]. They are defined as:

$$P_i = \log \left(\frac{x_i^\gamma}{x_i^{\gamma'}} \right), \quad P'_i = \log \left(\frac{x_i}{x_i^{\gamma'}} \right). \quad (4.1)$$

Predicting the logarithm of the partitioning coefficients ensures they always have physical positive values and preserves the symmetry between the γ and γ' phases.

A superalloy comprises n elements and p phases, giving a total of $np + p$ variables of interest. The goal is to calculate them from the nominal composition of the superalloy $\mathbf{x} = [x_1, \dots, x_n, x_1^{\text{HT}}, \dots, x_{2m}^{\text{HT}}]^T$. There are also the following physical constraints on these properties:

Total components sum to unity for each phase.

$$\sum_i x_i^\alpha = 1 \quad (4.2)$$

Total phases sum to unity.

$$\sum_\alpha f_\alpha = 1 \quad (4.3)$$

Sum of all elements in all phases is amount of element in the material.

$$\sum_\alpha f_\alpha x_i^\alpha = x_i \quad (4.4)$$

In our database entries f is often determined from the measured chemical composition of each phase using the n versions of Eq. 4.4, and is hence algebraically over-determined, resulting in an approximate value determined by finding the best fit for f to a rearrangement of Eq. 4.4 [154, 158]. Typically this means Eq. 4.4 does not hold exactly. Another reason this equation may not be fulfilled exactly is that the γ' phase fraction has been measured not only independently of the phase compositions but also via another method—e.g. via

Table 4.1: Summary of the database.

Phase composition (at. %)									
	Ni	Cr	Co	Re	Ru	Al	Ta	W	Ti
Min (> 0)	47.28	3.00	2.50	0.64	1.30	2.00	0.44	0.03	1.12
Max	86.50	24.47	18.80	2.50	3.50	14.20	4.03	5.76	5.84
Median	66.50	12.55	6.65	2.00	3.50	11.20	1.99	1.53	2.70
Mean	67.46	12.30	8.20	1.75	3.06	9.89	1.97	2.88	1.97
Frequency	97	96	59	18	5	97	55	54	61

Heat treatment (°C hrs)									
	#1	#2	#3	#1	#2	#3	#1	#2	#3
Min (> 0)	760	0.25	760	0.25	700	0.5			
Max	1300	1500	1160	264	1050	100			
Median	980	8	850	24	1040	16			
Mean	963.8	305.2	856.9	31.0	941.4	24.8			
Frequency	92	38	7						

Properties									
	Ni	Cr	Co	Re	Ru	Al	Ta	W	Ti
Min	-0.692	0.404	-0.208	0.142	1.169	-6.984	-5.711	-0.411	-5.220
Max	0.133	3.086	1.665	7.078	1.508	-0.488	0.489	1.329	-0.340
Median	-0.154	2.038	1.077	1.794	1.218	-1.500	-1.892	0.311	-1.740
Mean	-0.170	1.926	1.027	2.640	1.267	-1.669	-2.337	0.355	-2.049
Frequency	97	96	59	18	5	97	54	52	59

log partitioning coefficient P_i									
	Ni	Cr	Co	Re	Ru	Al	Ta	W	Ti
Min	-0.297	0.274	-0.037	0.122	0.390	-1.410	-1.208	-0.446	-1.293
Max	0.128	2.610	1.145	3.039	0.722	0.621	0.666	1.116	-0.039
Median	-0.058	1.320	0.508	0.857	0.568	-0.445	-0.356	0.100	-0.423
Mean	-0.063	1.361	0.550	1.194	0.565	-0.518	-0.371	0.173	-0.550
Frequency	97	96	59	15	5	97	54	52	59

γ'									
	Ni	Cr	Co	Re	Ru	Al	Ta	W	Ti
Min	-0.297	0.274	-0.037	0.122	0.390	-1.410	-1.208	-0.446	-1.293
Max	0.128	2.610	1.145	3.039	0.722	0.621	0.666	1.116	-0.039
Median	-0.058	1.320	0.508	0.857	0.568	-0.445	-0.356	0.100	-0.423
Mean	-0.063	1.361	0.550	1.194	0.565	-0.518	-0.371	0.173	-0.550
Frequency	97	96	59	15	5	97	54	52	59

atom probe tomography or chemical analysis for the phase composition versus an ocular determination from SEM imagery for the phase fraction. In both cases Eq. 4.4 should hold to within the experimental tolerances of the independent γ and γ' phase composition and fraction measurements.

Relaxing Eq. 4.4 from a strict constraint means that all but one phase fraction needs to be predicted, and for each phase all but one component, i.e. a total of $np - 1$ predictions. In the subsequent sections the specific case of superalloys will be referred to, with $p = 2$ phases. f will refer to the fraction of γ' or precipitate phase in the alloy, and f^γ can then be inferred by Eq. 4.3. The constraints implied by Eq. 4.4 are revisited in section 4.3.2.

4.3 Computational method

4.3.1 Machine learning methodology

Gaussian process regression (GPR) machine learning is adopted to predict the log partitioning coefficients \hat{P}_i and \hat{P}'_i and the γ' phase fraction \hat{f} (and corresponding uncertainties) of each element i in the alloy from its features. The final values for the phase chemistry can then be calculated to minimise the overall uncertainty. GPR takes a Bayesian approach to ML, in which an optimal posterior distribution—from which predictions are made—is formed from a prior distribution and a likelihood calculated from the training dataset. The prior distribution is assumed to be Gaussian with covariance determined by a kernel function. The functional form of the kernel should be chosen to suit the problem, but its hyperparameters are optimised using the training data. In this chapter, the standard approach of maximising the log marginal likelihood of the training data [12, 182]. The GPR implementation in the Scikit-learn library for Python was used [183].

Specifying the kernel provides an opportunity to incorporate our prior physical knowledge into the machine learning, which should give a more accurate model with less data. Superalloy properties are usually determined mainly by their composition rather than their heat treatment [84–86, 88, 124]. This physical rule of thumb is captured in the following kernel:

$$k(\mathbf{x}, \mathbf{x}') = k_{\text{comp},0}(\mathbf{x}_c, \mathbf{x}'_c) + k_{\text{comp},1}(\mathbf{x}_c, \mathbf{x}'_c) k_{\text{HT}}(\mathbf{x}_h, \mathbf{x}'_h) . \quad (4.5)$$

The first kernel term captures the bulk of the variation due to composition. The second kernel term captures the heat treatment and can be interpreted as an AND operation for the two measures of similarity, coupling heat treatment and composition [13]. A variation of Eq. 4.5 in which the second composition term was a constant was also tested.

Three alternate kernel functions were considered in this work. A simple and popular

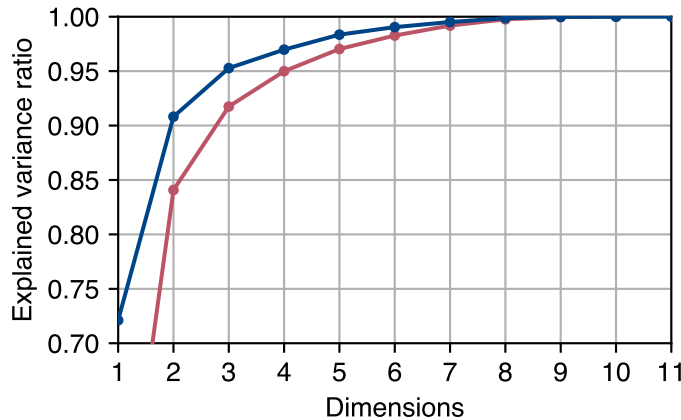


Figure 4.1: Explained variance with the number of dimensions by principal component analysis for the composition of superalloys included in this work. The blue line is for the full composition and the red line is for the composition excluding the base element.

choice of kernel function is the Gaussian radial basis function (RBF):

$$k(\mathbf{x}, \mathbf{x}') = e^{-\|\mathbf{x} - \mathbf{x}'\|^2/l^2} . \quad (4.6)$$

Here $\|\cdot\|$ is the ℓ_2 norm. The kernel has a single hyperparameter to be optimised during fitting: the lengthscale l . Our second choice is the linear kernel:

$$k(\mathbf{x}, \mathbf{x}') = b + \mathbf{x} \cdot \mathbf{x}' , \quad (4.7)$$

collapsing the method to ridge regression when $b = 0$ [12, 13]. This was used as a comparison to the models with more complex kernels. The third choice is motivated by previous work that used GPR to model the effects of alloy heat treatments, which used the automatic relevance determination (ARD) variation on the Gaussian RBF kernel [180, 184]. This kernel introduces a length parameter for each feature, $k(\mathbf{x}, \mathbf{x}') = \exp(-\|(\mathbf{x} - \mathbf{x}') \circ \mathbf{I}^{-1}\|^2)$.

Often the phase behaviour of an alloy is governed by the concentrations of a few elements. This low dimensional structure can be encoded in the kernel by projecting the feature vector to a lower dimensional subspace, $\mathbf{x} \mapsto B\mathbf{x}$, with B being a low rank matrix. B could be found prior to fitting the kernel via principal component analysis, see Fig. 4.1, or it could be optimised as a hyperparameter of the kernel during training [185]. Prior knowledge tells one to anticipate two main groups of elements in a superalloy—Ni-like elements, and Al-like elements—with a possible third group being the refractory elements [3, 17, 30, 99, 186], suggesting that a matrix of around rank 3 would be suitable.

Evaluating the quality of uncertainty prediction

GPR delivers uncertainty σ_y estimates for each of its predictions \hat{y} , so evaluating how close the uncertainties are to the real-life validation data, y , is crucial. The typical error in a prediction $\hat{y} - y$ should follow a Gaussian distribution with standard deviation σ_y . It follows that $(\hat{y} - y)/\sigma_y \sim \mathcal{N}(0, 1)$. This quantity is accumulated over all predictions and then is arranged into a histogram and compared to an ideal ‘Gaussian’ histogram with M bins of equal area $A = 1/M$ such that each bin has equal noise. From this a distribution of uncertainty quality (DUQ) is defined as the absolute sum of the difference in the areas of bins between the two histograms. For N data points this is defined as:

$$\text{DUQ} = \frac{1}{2} \frac{M}{M-1} \sum_{m=1}^M \left| \frac{n_m}{N} - \frac{1}{M} \right| , \quad (4.8)$$

where the number of data points in each real bin, n_m , is normalised such that $\sum n_m = N$. The number of bins is then optimised to achieve minimal value as described in the appendix. A minimal $\text{DUQ} = 0$ indicates a perfect estimate of the uncertainties whereas a peak $\text{DUQ} = 1$ indicates a poor estimate of uncertainty.

4.3.2 Calculation of phase compositions and fractions

Dynamic choice of balance element

For each n component superalloy the relevant GPR models will predict all $2n$ partitioning coefficients $\{\hat{P}_1, \dots, \hat{P}_n, \hat{P}'_1, \dots, \hat{P}'_n\}$ and the γ' fraction, yielding compositions \hat{x}_i^α and also \hat{f} . This is more than the total number of properties needed, meaning for each phase the amount of one element, \hat{x}_i^α , will be calculated using Eq. 4.2—which will be called the balance element, $\hat{x}_{\text{bal},i}^\alpha$. Rather than fixing one component to be the balance element in every alloy, instead, whichever minimises the difference between the component’s balance value and the GPR value is dynamically chosen, accounting for the uncertainty prediction of the GPR model σ_i^α , that is:

$$\min_i \left[\frac{|\hat{x}_{\text{bal},i}^\alpha - \hat{x}_i^\alpha|}{\sigma_i^\alpha} \right] . \quad (4.9)$$

Since the numerator is the same for every element in a given alloy, this is equivalent to choosing the element with maximal uncertainty in its value to be the balance element.

For the final model presented in the next section, the dynamic choice of balance element was compared to a static choice, in this case the conventional choice of Ni. For Ni itself—a crucial element—the static method gave $R^2 = 0.757$ and 0.888 in the γ' and γ phases compared with an improvement of $R^2 = 0.824$ and 0.927 respectively for the dynamic method. For Al there was also an improvement with the static method

giving $R^2 = 0.631$ (γ') and 0.510 (γ) compared with $R^2 = 0.674$ and 0.599 for the dynamic method. This was despite Al being chosen as the balance element for 47 and 15 predictions (out of 97) for the γ' and γ phase respectively using the dynamic method.

Bayesian inferral of a consistent precipitate fraction

Predicting the precipitate fraction \hat{f} , and the phase compositions $\hat{\mathbf{x}}^\gamma$ and $\hat{\mathbf{x}}^{\gamma'}$ gives us a full determination of the phase chemistry. However the composition for each phase may not sum to the total composition—that is Eq. 4.4 will not hold exactly but it should hold approximately [154, 158]. To improve consistency a Bayesian approach was taken to synthesise the information from the output of the ML models for the phase compositions and for f to give the phase composition most likely to be consistent with a valid total composition. The output of the GPR model for f is taken as a prior, and the likelihood is taken to be:

$$P(\mathbf{x}|\hat{\mathbf{x}}^\gamma, \hat{\mathbf{x}}^{\gamma'}, f, \sigma_i) \propto \prod_i \exp \left[-\frac{(x_i - f\hat{x}_i^{\gamma'} - (1-f)\hat{x}_i^\gamma)^2}{2\sigma_i^2} \right] .$$

With the standard deviation σ_i calculated from the uncertainties on the compositions as $\sigma_i^2 = \hat{f}^2\sigma_i^{\gamma'^2} + (1-\hat{f})^2\sigma_i^{\gamma^2}$, a conjugate prior to the likelihood is produced and hence the posterior is also a Gaussian, with mean value and standard deviation:

$$\hat{f} = \frac{\hat{f} + \sum_i (x_i - \hat{x}_i^\gamma)(\hat{x}_i^{\gamma'} - \hat{x}_i^\gamma) \left(\frac{\sigma_f}{\sigma_i}\right)^2}{1 + \sum_i (\hat{x}_i^{\gamma'} - \hat{x}_i^\gamma)^2 \left(\frac{\sigma_f}{\sigma_i}\right)^2} \quad (4.10)$$

$$\tilde{\sigma}_f^2 = \frac{\sigma_f^2}{1 + \sum_i (\hat{x}_i^{\gamma'} - \hat{x}_i^\gamma)^2 \left(\frac{\sigma_f}{\sigma_i}\right)^2} , \quad (4.11)$$

which are taken as the final values for the precipitate fraction and its uncertainty. Note that in the limit $\sigma_f \gg \sigma_i$, Eq. 4.10 agrees with the method of Reed et al [154, 158]. The method described above can be viewed as transforming Eq. 4.4 from a strict constraint into a ‘soft’ probabilistic constraint. A flowchart overview of how the final phase compositions and fractions are predicted for a given input composition is shown in Fig. 4.2.

4.4 Results and discussion

Variations of the GPR model with different kernels were trained on the database described in section 4.2. For each GPR model 5-fold cross validation was carried out. This procedure was used to fairly assess the quality of the different models in a way that will also highlight possible issues with over-fitting owing to a large number of variables. The

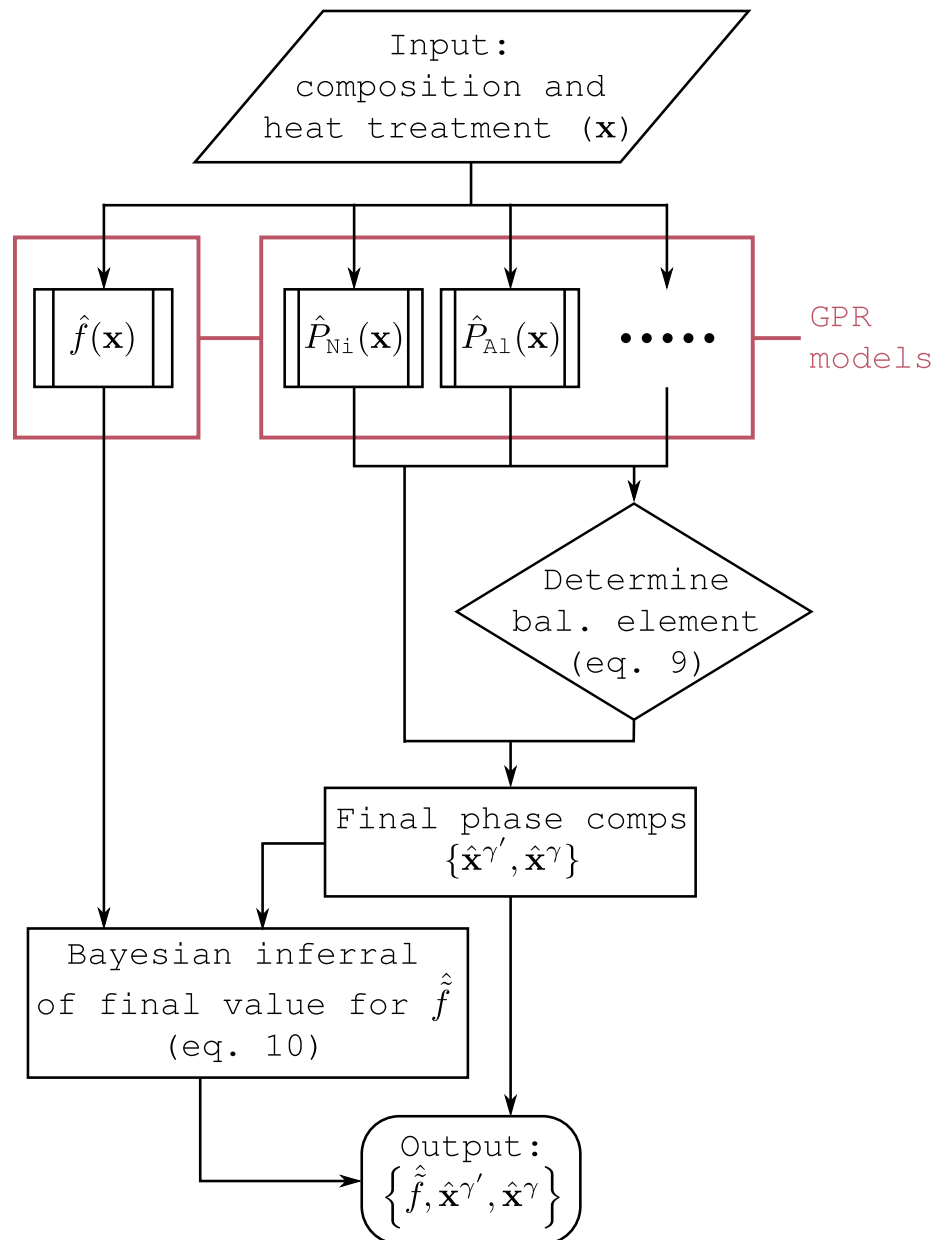


Figure 4.2: Flowchart outlining how phase chemistry predictions are made for a given alloy composition.

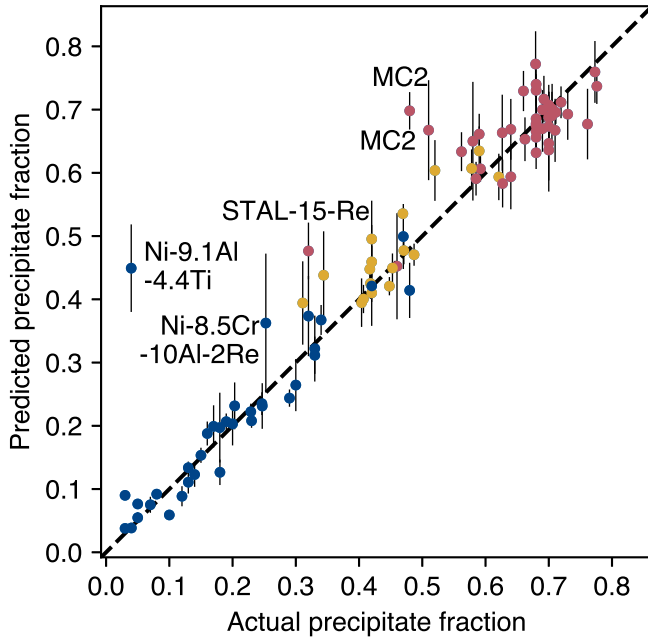


Figure 4.3: Predicted precipitate (γ' phase) fraction with error bars for validation data from GPR models fitted across 5-folds, with kernel scheme Eq. 4.5 and functional form Eq. 4.12. Colours refer to different types of superalloy: blue are laboratory alloys, yellow are other polycrystalline superalloys, and red are single-crystal superalloys. We highlight the composition of one particular superalloy.

step-by-step procedure is:

1. 80% of the initial dataset is selected at random as *training* data, with the remaining 20% being *validation* data.
2. A GPR model is trained with the training data without sight of the validation data. Here the training procedure is to fit the kernel hyperparameters so as to maximise the log marginal likelihood of the training data [12, 182].
3. The GPR model is tested against the validation data to get a measure of the accuracy. If the training data was over-fitted owing to a large number of model variables then the model will deliver poor accuracy against the blind validation data. Similarly, if the model has not captured the underlying physics of the dataset, it will perform comparatively poorly on the validation data.
4. The procedure 1–3 is repeated five times with non-intersecting validation datasets so as to produce a validation prediction for all the data that is available, and the accuracy of each validation is stored.
5. The accuracy of predictions on each of the five validation datasets are combined to

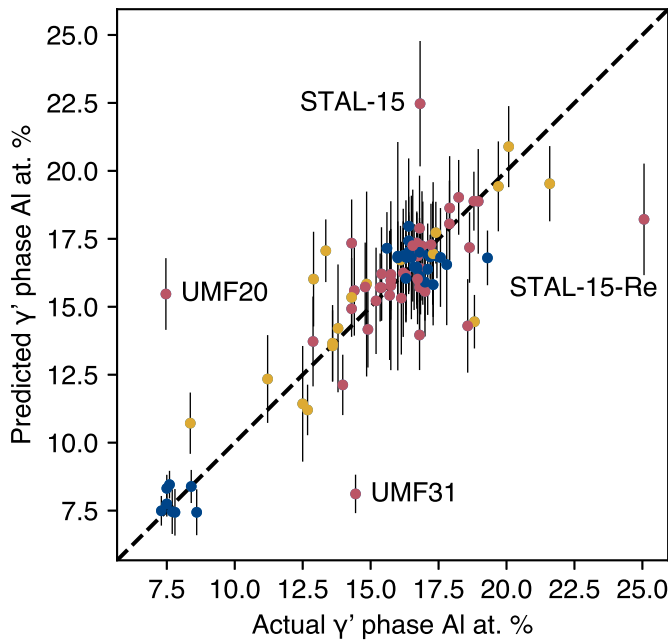


Figure 4.4: Predicted Al at. % in the γ' phase for validation data from GPR models fitted across 5-folds, with kernel scheme Eq. 4.5 and functional form Eq. 4.12. Colours refer to different types of superalloy: blue are lab alloys, yellow are other polycrystalline superalloys, and red are single-crystal superalloys.

deliver an overall coefficient of determination (R^2 value) calculated over the entire dataset.

Throughout the following section the R^2 value calculated in this manner has been used as the metric to compare the different GPR models. We have also introduced the distribution of uncertainty quality (DUQ) described in section 4.3.1 as a metric to further explore the quality of a model’s predictions. Training on the full database took two minutes on a laptop with an Intel Core i7 CPU—once trained predictions can be made effectively instantaneously.

The Gaussian RBF (Eq. 4.6), linear (Eq. 4.7), and ARD kernels were initially tested for the composition only, $k(\mathbf{x}, \mathbf{x}') = k(\mathbf{x}_c, \mathbf{x}'_c)$. The results for selected properties are shown in Table 4.2. Using the linear kernel is broadly the same as the Alloy Design Program [100, 110–114], which gave good results for the γ' fraction, but was less accurate for some elements in the γ phase. The RBF kernel gave slight improvements for Ni and Al in both phases as well as the γ' fraction. The ARD kernel performed slightly worse than the standard RBF kernel overall, this is due to overfitting, as has been noted in previous work [187]. In the case of Gaussian RBF kernels, it was found overfitting could be reduced by setting the minimum value of the length scale to $l = 0.3$, corresponding to about half the phase diagram [13].

Kernel $k(\mathbf{x}, \mathbf{x}')$	γ phase elements		γ' phase elements		γ' frac.
	Ni	Al	Ni	Al	
Linear	0.921	0.040	0.669	0.591	0.900
RBF	0.940	0.371	0.704	0.676	0.905
ARD	0.936	0.349	0.724	0.658	0.896
Optimal (Eq. 4.12)	0.927	0.599	0.824	0.674	0.917

Table 4.2: Comparison of coefficients of determination (R^2) for different kernels, including the optimal final kernel. Refer to text for explicit form of kernels.

With both linear and RBF kernels working well, a systematic approach was then taken to combining them according to the kernel scheme given in Eq. 4.5. The best results were found for the following kernel, henceforth referred to as the optimal kernel:

$$k(\mathbf{x}, \mathbf{x}') = b + a_0 \mathbf{x}_c \cdot \mathbf{x}'_c + a_1 e^{-\|B(\mathbf{x}_c - \mathbf{x}'_c)\|^2/l_1^2} \cdot e^{-\|\mathbf{x}_h - \mathbf{x}'_h\|^2/l_2^2} . \quad (4.12)$$

The first part is a linear kernel and the second an RBF kernel that combines composition and heat treatment, B is a low rank matrix found from principal component analysis [13]. A projection onto the first 3 principal components was found to be optimal, in agreement with the discussion in section 4.3.1.

Kernel Eq. 4.12 gave excellent results for the γ' fraction with $R^2 = 0.917$, and for all components $R^2 > 0.8$ (the full set of R^2 values for this model are given in Fig. 4.5) except Al in the γ' phase ($R^2 = 0.674$) and Al, Ta and Ti in the γ phase ($R^2 = 0.599, 0.546, 0.766$ respectively). This is due to the role of these three elements as γ' formers. This role leads to their at. % in the γ' phase being more constant between different alloys, resulting in a smaller variance and hence lower R^2 , most notably for Al. Analysis of the root mean-squared error (RMSE) showed it to be comparable to the other components. If Al, Ta, and Ti concentrations in the γ' phase have a strong physical correlation to the alloy composition, this is not the case for the γ phase content—the remaining amount of each element that does not form the γ' phase is dissolved into the γ phase—and for this reason it is less strongly correlated to the overall alloy composition which results in the generally lower R^2 values for the γ' forming elements in the γ phase (Table 4.2).

The predicted γ' fractions found from this model are compared to the experimental values in Fig. 4.3. Agreement is on the whole excellent. The most significant outlier is lab alloy Ni-9.1Al-4.4Ti. This alloy is peculiar in having a low number of components with similar at. % values across both phase compositions and the nominal composition, which leads to a large error and uncertainty according to eqs. 4.10–4.11 [84]. Two other outliers are similar to training set alloys but with the addition of Re, suggesting more data for Re-bearing alloys may be required to explain its anomalous effect [85, 158]. Finally, two outliers correspond to the commercial single-crystal superalloy MC2 with extreme 3rd stage heat treatments (1050°C for 10 hours and 100 hours respectively) [127]—again,

more data is needed for extreme outlying heat treatment regimes, especially in the 3rd stage.

A variant of the optimal kernel Eq. 4.12 was also tested without the heat treatment term of the kernel which was set to 1. It performed similarly to the optimal kernel for phase composition predictions but was significantly outperformed for predictions of the γ' phase fraction: it achieved an $R^2 = 0.767$ compared to 0.917 for the optimal kernel. This tells us the optimal model is capturing the variance due to heat treatment, even if it is not capturing the full physics of complex heat treatment regimes such as the case of MC2 described above.

Fig. 4.4 shows the predictions for one crucial component—the Al content of the γ' phase. Al is the principal former of the γ' phase and the primary constituent of the secondary sublattice in this phase [3, 33]. Significant outliers are highlighted in the figure. Of these UMF20 and UMF31 are unusual compared to the other alloys because Ti rather than Al is the primary γ' phase forming element in their composition [106, 123, 165]. In the case of STAL-15 and STAL-15-Re, they have similar input compositions whilst their reported phase compositions differ greatly hinting that they are either near to a phase transition or a possible anomalous result [158].

A key feature of GPR is the ability to estimate uncertainty in its predictions. Therefore, in Fig. 4.6 we compare the error in a prediction measured against the experimental value to the uncertainty in the prediction, which should take a single value. We study both the precipitate fraction and the chemical compositions. The area under each histogram is normalised to 1. For compositions the distribution is symmetrical and similar to the Gaussian distribution, with a comparatively small DUQ = 0.075 (see Eq. 4.8) . For the precipitate fraction f the DUQ is larger at 0.220, and the distribution has a skew to under/overestimation.

A practical advantage of having quantified uncertainties is that predictions can be filtered based on this uncertainty [188, 189]. Fig. 4.7 shows an example of this for the precipitate fraction. By focusing on only the most certain results, the RMSE reduces significantly, and is closer to the theoretical lower bound for the reduction than the upper bound. The lower and upper bound are given by filtering the data in the order that minimises or maximises respectively the RMSE. The steps in the blue curve in Fig. 4.7 occur as significant outlying predictions are filtered out. Each step corresponds to a significant outlier that can be identified on Fig. 4.3 by the magnitude of its uncertainty; for example the step at the highest fraction of data predicted corresponds to Ni-8.5Cr-10Al-2Re, the next MC2, then Ni-9.1Al-4.4Ti, etc. Step-like behaviour would vanish if all the predictions with the largest errors had the largest uncertainties, i.e. the lower bound curve in yellow. This method is useful when the model’s predictions are to be used to choose new alloy compositions for experimental testing, as it allows the alloy designer to only test compositions below a certain predicted error threshold and to focus on the

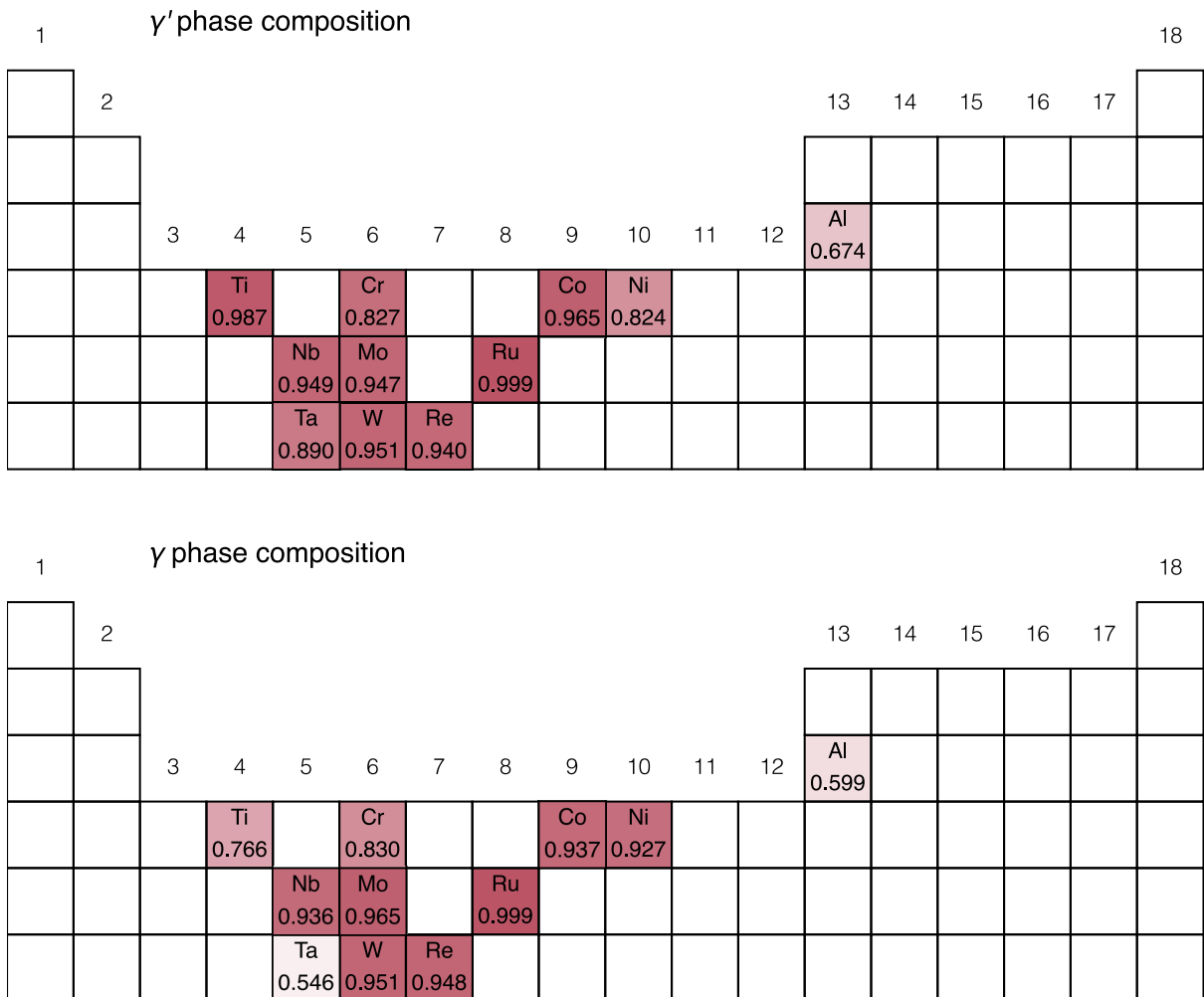


Figure 4.5: Overview of R^2 values obtained for predictions of phase composition using the final GPR model. Elements have their respective R^2 listed below them and have also been colour coded to reflect this value (darker is better). The data has been superimposed on the periodic table to reflect how the results correlate to element groupings (group numbers are at the top of each column).

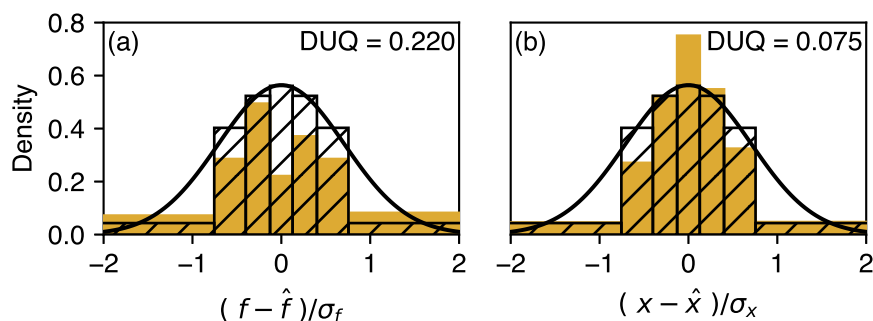


Figure 4.6: Histograms for the uncertainties associated with predictions. The yellow histogram is for the data and the hatched histogram is for an ideal normal distribution (solid bold line) with the same bins. Left (a): histogram for precipitate fraction data. Right (b): Histogram for all the chemical composition data (all elements across both phases).

predictions most likely to fulfil the target tolerance in an experiment.

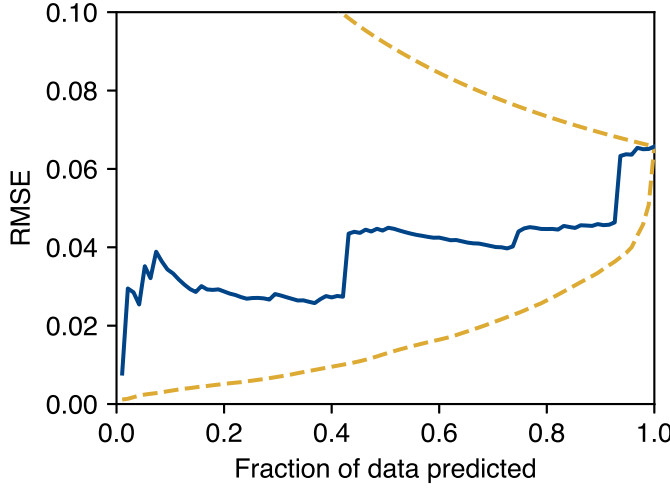


Figure 4.7: Plot of the calculated RMSE when predictions with the highest uncertainty are filtered out (blue line). The yellow dash-dotted lines give theoretical upper and lower bounds.

4.4.1 Comparison to CALPHAD

The final GPR model was trained on the full database with 93 entries. It was then tested against unseen experimental atom probe tomography data collected by Sulzer *et al* for the SX-series alloys specifically for benchmarking the performance of CALPHAD [161]. In that test two thermodynamic databases were tested, TTNi8 and TCNi8 [71]. For each prediction tool, the root mean-squared error (RMSE) was calculated over all the elements in each phase in each SX-series alloy, as well as the precipitate fraction f , giving three metrics for each method (Table 4.3). For both the γ and γ' phases and the precipitate fraction f , the GPR model is more accurate than CALPHAD.

Method	γ' phase (RMSE)	γ phase (RMSE)	γ' fraction f (RMSE)
TCNi8	0.0106	0.0354	0.0371
TTNi8	0.0072	0.0324	0.0205
This work	0.0065	0.0321	0.0201

Table 4.3: Root mean-squared error (RMSE) for the predictions of the GPR model of this work and CALPHAD models on the SX-series superalloys using the TCNi8 and TTNi8 databases.

The composition of the SX series alloys in Ref. [161] had been chosen to explore a new region of composition space with high Cr content, and consequently both the

GPR model and the two CALPHAD models were extrapolating in this region. Due to the inherent inclusion of physical laws it was anticipated that CALPHAD would be superior for extrapolative predictions, so it is particularly impressive that the GPR model outperforms CALPHAD. A further advantage of the GPR method is that it quantifies the uncertainty associated with predictions.

4.5 Conclusion

A Gaussian process regression model was developed to predict the phase chemistry (phase compositions and fractions) of nickel-base superalloys. It inputs the nominal composition of a superalloy and the ageing heat treatments, to then predict the chemical composition of the key γ and γ' phases, and their relative abundance. The composition predictions are combined via a probabilistic approach to produce the final output composition. Cross-validation was used to compare a number of different kernel schemes for the GPR models, with the optimal kernel achieving a coefficient of determination $R^2 = 0.917$ for the precipitate fraction.

The real life utility of the GPR model was demonstrated by predicting the composition of the benchmark SX-series superalloys. The GPR model outperformed CALPHAD predictions using both the TTNi8 and TCNi8 databases [161]. This demonstrates the benefits of combining the best of physical and statistical approaches. The GPR model has a number of additional advantages over CALPHAD:

- Returns quantified uncertainty estimates for each prediction.
- No prior thermodynamic knowledge is required to construct the model.
- Model can easily be retrained as more data becomes available.
- Additional non-equilibrium effects can be incorporated in the model.
- Once trained, no free energy minimisation step is required to make predictions from the model.
- The trained model can be used to identify outliers in the initial dataset by highlighting property entries that lie the furthest from the model's predictions [174].

As discussed above our GPR model made better predictions when the kernel included a heat treatment component, however further work is required to determine whether it can precisely capture the evolution of an alloy's microstructure with different applied ageing heat treatments. Training and assessing the model on this problem is difficult due to the paucity of experimental data where phase composition has been determined for superalloys with the same nominal composition but different ageing heat treatments [86,

[127]. A better representation of the heat treatment descriptors could improve this. Thermodynamic modelling approaches to predicting the effects of heat treatments do exist but their use in optimising heat treatments for alloys of pre-determined composition is involved [18, 190].

In this chapter, the most straightforward dynamic method that makes use of the uncertainty in the initial predictions was used, Eq. 4.9. It was found that this gave improved results for crucial elements such as Ni and Al compared to a fixed balance element model (Section 4.3.2). Alternate dynamic schemes for balancing the total phase composition in order to fulfil Eq. 4.2 can be devised, which may produce further improvements.

The GPR model is completely generic and can be applied to other material systems, meaning that it can be extended to predict other properties as well as thermodynamic ones. This would enable the development of a complete machine learning tool able to design practical alloys that simultaneously satisfy a range of target properties.

4.A Appendix: supplementary work to paper

4.A.1 Distribution of uncertainty quality

The distribution of uncertainty quality (DUQ) as defined in the paper (Eq. 4.8) has a minimum value of 0 and a maximum value of 1. The maximum value can be shown by considering the possible values of the occupation of each bin n_m to form a vector $\mathbf{n} = [n_1, \dots, n_M]^T \in \mathcal{R}^M$. Then the DUQ is proportional to the ℓ^1 norm of the vector $\mathbf{n}/N - \mathbf{a}$, where $\mathbf{a} = A \cdot \mathbf{1}$. Since we require $\sum n_m = N$ this can visually be depicted on a simplex plot, see fig. A1. By the ℓ^1 metric the furthest distance from \mathbf{a} is found at $\mathbf{n} = [0..0, N, 0..0]^T$. At these values the full DUQ Eq. 4.8 achieves a value of 1.

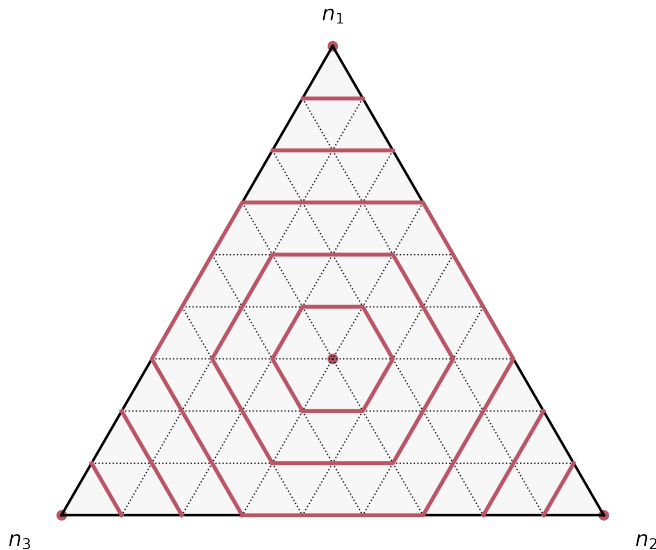


Figure A1: Ternary simplex plot representing the DUQ as an ℓ^1 norm. The red curves are ℓ^1 metric contour lines. The levels monotonically increase from the centre (DUQ = 0), giving the highest value at each of the points $n_m = N$ (DUQ = 1).

For both the ideal and real histogram the edges of each bin z_m are defined such that:

$$\int_{z_{m-1}}^{z_m} \varphi(z) dz = A \quad , \quad (A1)$$

where $\varphi(z)$ is the PDF for the Gaussian distribution $\mathcal{N}(0, 1)$, and the area of each ideal bin is $A = 1/M$. This ensures the histogram for the ideal distribution has a total area of

1. For an odd number of bins the rightmost edges z_m with $z_m > 0$ are given by:

$$z_m = \operatorname{erf}^{-1} \left((2m-1) \frac{1}{M} \right) , \quad (\text{A2})$$

where $m = 1, 2, \dots, (M+1)/2$.

The number of bins is optimised by minimising a quantity related to the DUQ:

$$\frac{1}{2} \sum_m^M \left| \frac{n_m}{M} - \frac{1}{M} \right| + \int_{\infty}^{\infty} |h(z) - \varphi(z)| dz , \quad (\text{A3})$$

where $h(z)$ is the height of the ideal bin at position z . The second term accounts for the difference in area between the ideal bins and the normal distribution, which favours larger numbers of bins. Minimising the DUQ directly will always lead to the minimum number of bins being used.

Eq. A2 leads to the outermost bins having infinite width and zero height. For visualisation purposes this is undesirable so a cutoff can be introduced that gives all the bins finite width whilst not affecting the optimal number of bins. We found a cutoff $z_c = \pm \operatorname{erf}^{-1}(0.999999) = \pm 3.459$ to be a suitable choice.

4.A.2 Bayesian inferral of consistent phase chemistry

The prior is taken to be the prediction of the GPR model for precipitate fraction at input \mathbf{x} :

$$P(f|\mathbf{x}) = \frac{1}{\sqrt{2\pi\sigma_f(\mathbf{x})^2}} \exp \left[-\frac{(f - \hat{f}(\mathbf{x}))^2}{2\sigma_f(\mathbf{x})^2} \right] . \quad (\text{A4})$$

The likelihood expresses Eq. 4.4 probabilistically:

$$P(\mathbf{x}|\hat{\mathbf{x}}^\gamma, \hat{\mathbf{x}}^{\gamma'}, f, \sigma_i) \propto \prod_i \exp \left[-\frac{(x_i - f\hat{x}_i^\gamma - (1-f)\hat{x}_i^{\gamma'})^2}{2\sigma_i^2} \right] . \quad (\text{A5})$$

The posterior probability can then be calculated from the product of eq. A4 and eq. A5 according to Bayes' Theorem:

$$P(f|\mathbf{x}, \hat{\mathbf{x}}^\gamma, \hat{\mathbf{x}}^{\gamma'}) \propto \exp \left[-\frac{(f - \hat{f})^2}{2\sigma_f^2} - \sum_i \frac{(x_i - f\hat{x}_i^\gamma - (1-f)\hat{x}_i^{\gamma'})^2}{2\sigma_i^2} \right] . \quad (\text{A6})$$

The exponent can then be rearranged to complete the square:

$$\begin{aligned}
& \frac{(f - \hat{f})^2}{2\sigma_f^2} + \sum_i \frac{(x_i - f\hat{x}_i^{\gamma'} - (1-f)\hat{x}_i^{\gamma})^2}{2\sigma_i^2} \\
&= f^2 \left[\frac{1}{2\sigma_f^2} + \sum_i \frac{(x_i^{\gamma'} - x_i^{\gamma})^2}{2\sigma_i^2} \right] - 2f \left[\frac{\hat{f}}{2\sigma_f^2} + \sum_i \frac{(x_i - x_i^{\gamma})(x_i^{\gamma'} - x_i^{\gamma})}{2\sigma_i^2} \right] + \frac{\hat{f}^2}{2\sigma_f^2} + \sum_i \frac{(x_i - x_i^{\gamma})^2}{2\sigma_i^2} \\
&= \frac{1}{2\tilde{\sigma}_f^2} (f - \hat{f})^2 - \frac{\hat{f}^2}{2\tilde{\sigma}_f^2} + \frac{\hat{f}^2}{2\sigma_f^2} + \sum_i \frac{(x_i - x_i^{\gamma})^2}{2\sigma_i^2} .
\end{aligned}$$

Here \hat{f} and $\tilde{\sigma}_f$ are the mean and standard deviation of the posterior:

$$\hat{f} = \frac{\hat{f} + \sum_i (x_i - \hat{x}_i^{\gamma}) (\hat{x}_i^{\gamma'} - \hat{x}_i^{\gamma}) \left(\frac{\sigma_f}{\sigma_i}\right)^2}{1 + \sum_i (\hat{x}_i^{\gamma'} - \hat{x}_i^{\gamma})^2 \left(\frac{\sigma_f}{\sigma_i}\right)^2} \quad (A7)$$

$$\tilde{\sigma}_f^2 = \frac{\sigma_f^2}{1 + \sum_i (\hat{x}_i^{\gamma'} - \hat{x}_i^{\gamma})^2 \left(\frac{\sigma_f}{\sigma_i}\right)^2} . \quad (A8)$$

Note that this requires the standard deviation of the likelihood σ_i to have a form independent of f . The approximation used in this work is:

$$\sigma_i^2 = \hat{f}^2 \sigma_i^{\gamma'^2} + (1 - \hat{f})^2 \sigma_i^{\gamma^2} .$$

This is the familiar requirement that the prior is conjugate to the likelihood.

Chapter 5

Machine learning superalloy properties from physical descriptors

Abstract

An element-agnostic set of descriptors to model superalloy properties with Gaussian process regression models are proposed. Furthermore, a correction method is developed to deliver the best and most physical predictions for phase chemistry in multi-phase alloys. The model's performance in predictions is confirmed for superalloy phase chemistry and strength properties. When including new, unseen elements in the test data, the models still give good predictions; such extrapolations into new chemical-space are impossible with component-based descriptors.

This chapter was published as Taylor, P. L. & Conduit, G. Machine learning superalloy microchemistry and creep strength from physical descriptors. *Computational Materials Science* **227**, 112265 (Aug. 2023) [2].

5.1 Introduction

Hume-Rothery first developed his eponymous set of rules in 1935 [191, 192]. They describe whether any two elements could alloy together to form a stable solid solution. For substitutional alloys there are four rules: they concern the similarity of atomic radius, crystal structure, valency, and electronegativity. Further developments to solubility rules include the Pettifor scale and its 2016 proposed update by Glawe et al [193, 194]. The Hume-Rothery rules highlight the opportunity for fully element-agnostic models of phase composition that would enable them to be applied to any material, even those containing elements not before considered. However, the Calculation of Phase Diagram (CALPHAD) methodology—which has become the industry standard approach due to the promulgation of software such as ThermoCalc—typically relies on thermodynamic models that have been constructed element-by-element, limiting their broad applicability [67, 70, 71].

The same duality exists in applications of machine learning to alloys. Some researchers have adopted the approach of using alloy components directly as descriptors in their ML models. Such models have been used to model Ni-based superalloy phase chemistry, and design superalloys for a diverse range of applications [1, 8, 10, 111, 176, 195]. Other researchers have taken the approach of mapping alloy components to physical descriptors based on domain knowledge [172, 196–200]. This strategy greatly improves models trained on small datasets, whereas models trained on suitably large datasets were already able to self-encode the physical descriptions of a system in their latent space [201], see Hart et al (2021) for a thorough review [107].

Superalloys are precipitation hardened—their important bulk properties, such as high-temperature creep and yield strength, derive from their two-phase microstructure [3, 33, 49, 54, 202]. Hence, accurate prediction of the relative phase fraction and phase compositions is a crucial first-step towards property prediction. However, each generation of superalloys has typically included additional elements [4], the most recent being the inclusion of ruthenium [30, 92, 132, 154, 163]. The trend of additional elements improving properties is naturally extended by high-entropy superalloys (HESAs) [203–207]. Machine learning models that better transfer their inherent knowledge of alloy chemistry to new composition-space could accelerate the further development of superalloys.

In this chapter, a physics-inspired set of descriptors to describe superalloys that is element-agnostic is proposed. Gaussian process regression machine learning is then used to predict superalloy properties. For phase composition, Chapter 4 is built upon to develop and demonstrate a probabilistic correction method. In addition to interpolative scoring of the models in the usual cross-validated manner (via a withheld, randomly selected, test dataset), models are also scored on their ability to extrapolate to datasets containing alloy components not seen during training. Finally, creep strength models of Ni superalloys are developed using similar physics-inspired descriptor sets.

5.2 Computational method

In this section the computational method developed to predict phase behaviour is detailed. First, the physical descriptor-set used as input features to the machine learning models is described, then details are given of the Gaussian Process Regression models. Next, there is discussion of some particular problems with representing phase microchemistry data in machine learning models, and the novel correction method developed in this chapter to address them. Finally, this chapter’s approach to physical descriptor GPR models of creep strength is described.

5.2.1 Data representation

The first task was to predict superalloy microchemistry. This is described by the phase fraction, f^ϕ , and the corresponding composition of each phase, x_i^ϕ . Following other authors and the work of Chapter 4, partitioning coefficients are adopted in place of phase composition, $k_i^\phi = x_i^\phi/x_i$ [1, 30, 92, 99, 104, 106, 110, 111]. The partitioning coefficients give a simpler encoding of physical information—for a given element, its partitioning coefficients across many different alloys are typically more similar than its various phase component percentages. In order to use variables that are more normally distributed, a further transformation of f^ϕ is used, k_i^ϕ from their respective intervals to the real line:

$$p_i^\phi = \ln\left(x_i^\phi/x_i\right) \quad , \\ q^\phi = \operatorname{arctanh}\left(2f^\phi + 1\right) \quad .$$

As well as being necessary mappings, they also capture the physical symmetry: $f^\phi \rightarrow 1 - f^\phi \iff q^\phi \rightarrow -q^\phi$ and $k^\phi \rightarrow k^{\phi^{-1}} \iff q^\phi \rightarrow -q^\phi$.

The dataset used in this work is an updated version of that in Ref. [1], containing 123 entries with complete phase chemistry data (matrix and precipitate phase composition and fractions) [30–33, 85–87, 89, 95, 106, 110, 119, 124–127, 129, 130, 135, 137, 138, 141, 142, 146, 151, 152, 154, 155, 158, 160, 161, 164, 165, 167]. The phase composition dataset is presented in the conventional form, with the nominal alloy compositions and heat treatments being the inputs to the model, and the phase fractions and respective compositions being the output. However, in this chapter the dataset is ‘reshaped’ into a single-target format. This is represented graphically in Fig. 5.1 as a two-step process. First the dataset is reshaped so that for a single-phase ML model, each partitioning coefficient is considered to be a separate output, and the input gains an additional column labelling the output element. Note that in the GPR framework, this is equivalent to a multi-output Gaussian process (MOGP) [208]. This model will subsequently be referred to as the ‘plain method’. Secondly, the data is transformed into a physical representation, which is a function of composition and label, but does not explicitly preserve the label

as a feature. This means that predictions can be made for labels (i.e. components) not present in the training data—so long as the physical descriptors are carefully chosen. This model will be referred to as the ‘descriptor method’.

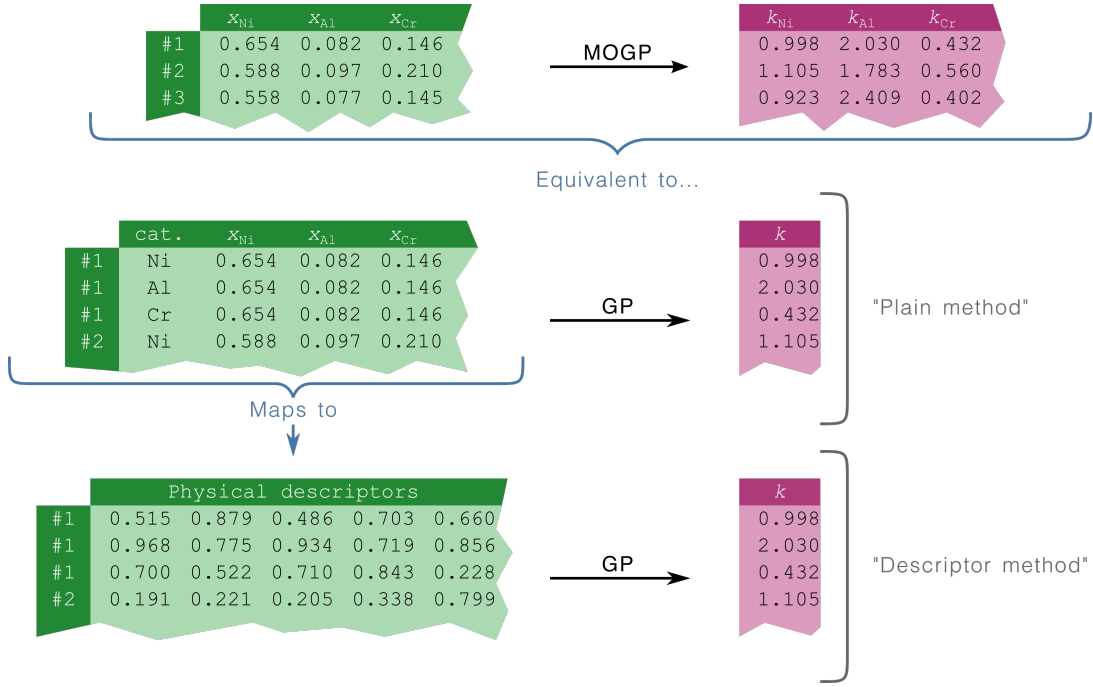


Figure 5.1: An overview of how the Gaussian process regression models in this work were formulated.

5.2.2 Physical descriptors

To fully understand the phase behaviour both the phase fraction, and also the partitioning of each element between the phases, must be predicted. The model for each property requires different inputs: for the phase fraction model, inputs were composition and heat treatment data; for the partitioning coefficient model, each entry gains a further feature corresponding to the component-label of the target, see Fig. 5.1 and Section 5.2.1. In the model, both this label and the composition are converted into element-agnostic descriptors. The most natural choice of physical descriptors would be based on the lattice structure and atomic arrangement of an alloy, but these are *a priori* unknown. Instead, a given alloy—for which, in this case, only the nominal composition is known—can be thought of an “atomic soup”, see Fig. 5.2. Inspired by ab initio electronic structure methods used in physics and chemistry, the atomic soup can be represented by the distribution of the constituent atoms’ electronic properties. Said distributions can be approximately specified by their mean, standard deviation; and higher order moments if necessary. This is how the descriptors (descriptor set A in Fig. 5.2) for modelling phase fraction were formulated. For the GPR model of partitioning coefficients, the atomic species labels were

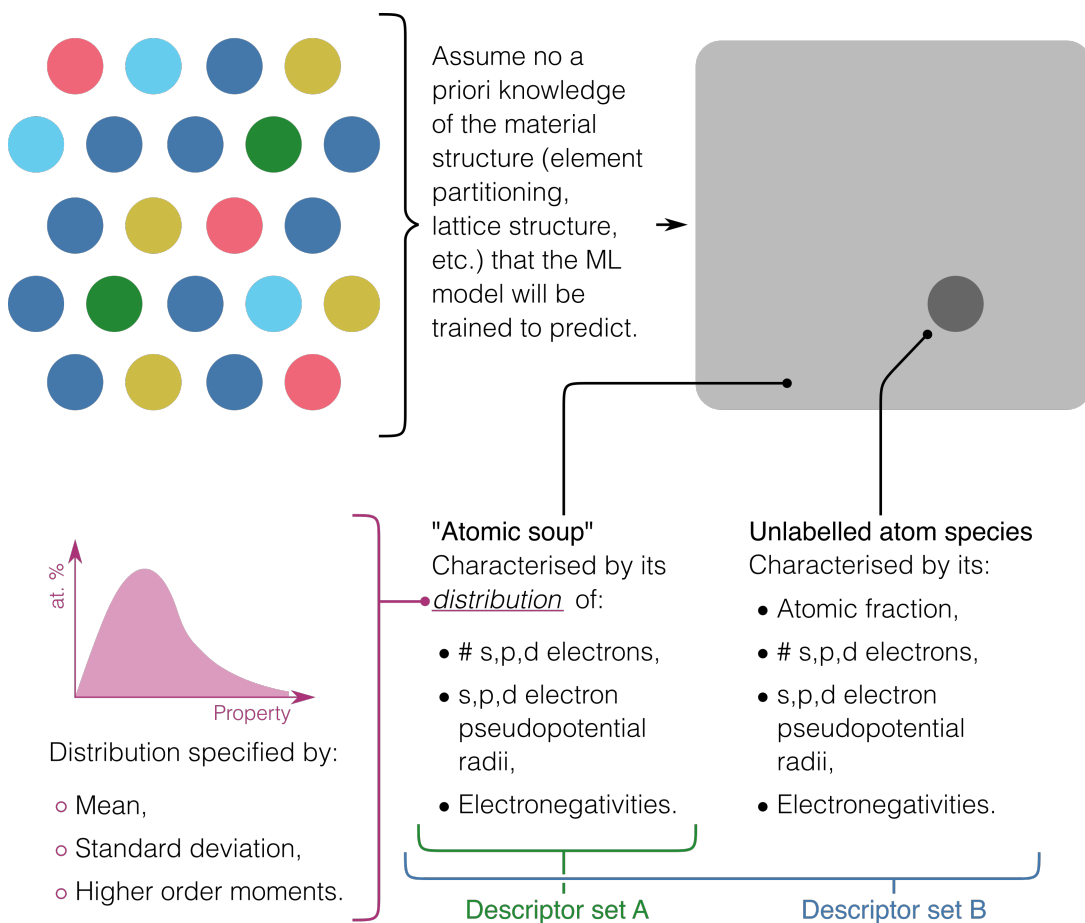


Figure 5.2: How physics-based descriptors were selected for this work. Descriptor sets A and B were used for different aspects of phase chemistry modelling. Descriptor set A was used to model phase fraction, B was used to model the partitioning coefficients.

also transformed to physical descriptors (Fig. 5.1 and Section 5.2.1), chosen following a similar logic (descriptor set B in Fig. 5.2).

The choice of descriptors bore a strong similarity to the popular descriptor-set MAGPIE [209]. Those used by Ling et al [210] and Liu et al [175] to model nickel superalloy properties are also similar. Much like these descriptor sets, electronic structure inspired descriptors are found to be especially powerful. Data used to construct the descriptors was taken from Refs. [211, 212].

Alongside its nominal composition, the precipitation heat treatments applied to an alloy will also affect its final composition and properties [1]. Up to three heat treatment stages were used as input features for each alloy; each comprising a treatment temperature (T_j) and time (τ_j), for a total of six features. Some assumptions are made about the solution heat treatment—see Section 4.2 for details. The theory of Ostwald ripening gives a theoretical dependence on heat treatment time and temperature for an alloy's

phase compositions [149, 213–215]:

$$\langle \Delta x_i^\phi \rangle^3(t) \sim \frac{e^{-\varepsilon_i/k_B T}}{T} t \quad ,$$

where ε_i is an activation energy associated with the diffusion of species i . The model's targets are the log partitioning coefficients; heat treatment times in the database varied over several orders of magnitude (from around 15 mins to 1000 hours). Putting this altogether, in this chapter it is proposed to represent m_{HT} -stage heat treatments with the following descriptors:

$$h'_j = \begin{cases} \sum_{k=1}^j \ln(\tau_k) - \ln(T_k) & , j \leq m_{\text{HT}} \\ 1/T_j & , m_{\text{HT}} < j \leq 2m_{\text{HT}} \end{cases} . \quad (5.1)$$

This retains the same total number of descriptors as in the initial input. In Section 5.3.3, it is shown that this set of heat treatment descriptors accurately capture the evolution of the alloys' phase chemistries and fractions.

5.2.3 Gaussian process regression

A large number of physical descriptors were proposed for use in the GPR model: much more than the number of input columns in the dataset (18 for the dataset with component and heat treatment inputs). To ensure that the GPR models were selecting the minimal set of relevant features during hyperparameter optimisation, an automatic relevance determination (ARD) Matérn kernel was used [13]. In cases where the ARD kernel lengthscale l for some of the features was found to be very large, $l \gtrsim 10^3$, small improvements in the model's score could be obtained by retraining the model without using said features at all. The GPyTorch library was used for GPR [117]. Both the L-BFGS and ADAM algorithms were tested for hyperparameter optimisation, with L-BFGS being found to give both better results for a small trade-off in training time.

5.2.4 Probabilistic correction to phase compositions

There are three physical constraints that alloy phase compositions—i.e. the output predictions of the GPR models for phase chemistry—must obey [1, 67]:

$$\sum_i x_i^\phi = 1 \quad , \quad (5.2)$$

$$\sum_\phi f^\phi = 1 \quad , \quad (5.3)$$

$$\sum_\phi f^\phi x_i^\phi = x_i \quad , \quad (5.4)$$

where there are m phases labelled ϕ and n components labelled i . Eqs. (5.2) & (5.3) are hard constraints that the total concentration and total phase fractions must each sum to unity. Eq. (5.4) can be interpreted as a soft constraint representing an assumption of minimal material loss in the forging process. Gaussian process regression does not present an obvious way to impose such constraints—in Section 4.3.2 they were imposed on the final model outputs. In particular, a Bayesian approach was taken to apply constraint Eq. (5.4) via a correction to the predicted phase fraction. In this work, the same approach is extended to apply a simultaneous correction to the phase fractions f^ϕ and the phase compositions x_i^ϕ . The output of the GPR models for phase fraction and phase composition are taken to be independent Gaussian processes, which for each alloy gives a prior:

$$\exp \left[-\frac{1}{2} (\mathbf{q} - \hat{\mathbf{q}})^T \Sigma_q (\mathbf{q} - \hat{\mathbf{q}}) \right] \prod_{\phi} \exp \left[-\frac{1}{2} (\mathbf{p}^\phi - \hat{\mathbf{p}}^\phi)^T \Sigma_{p^\phi} (\mathbf{p}^\phi - \hat{\mathbf{p}}^\phi) \right] , \quad (5.5)$$

and a likelihood relating to the soft constraint, where τ_i is a tolerance for ‘allowed’ component loss, and $\sigma_i^{(3)}$ is an estimated uncertainty on the sum on the LHS of Eq. 5.4

$$\prod_i \exp \left[-\frac{1}{2} \left(\frac{x_i - \sum_{\psi} f^{\psi} x_i^{\psi}}{\tau_i x_i + \sigma_i^{(3)}} \right)^2 \right] . \quad (5.6)$$

Combining these to give a posterior, expanding the exponent of the likelihood to quadratic order in $\Delta p_i^\phi = p_i^\phi - \hat{p}_i^\phi$, $\Delta q^\phi = q^\phi - \hat{q}^\phi$, and finally completing the square gives a new Gaussian probability distribution. This is equivalent to maximising the log-posterior probability with respect to the corrections to $\hat{\mathbf{q}}$ and $\hat{\mathbf{p}}$. This maximisation can be carried out subject to hard constraints for Eqs. (5.2) & (5.3). Doing so produces a correction to each of p_i^ϕ and q^ϕ , as well as a new, valid covariance for a given prediction, which in turn yields the associated uncertainties.

5.2.5 Creep strength modelling

A dataset of creep strength properties for single crystal Ni superalloys was compiled. Entries were drawn from academic literature and commercial databases. A substantial contribution to the dataset was from the open source creep rupture life dataset compiled by Liu et al [175] (266 entries). Database entries included multiple properties characterising creep strength, including elongation at rupture (82 entries), time to 1% creep (79), and minimum secondary creep rate (55). There were significantly more entries available for creep rupture life (388), reflecting the importance of this particular property as the primary metric of creep strength [3, 216]. For this reason, this chapter solely focuses on modelling creep rupture life. Each entry had two corresponding experimental conditions,

a temperature and applied stress. Other authors have found that direct ML models of the creep rupture life are more effective than modelling the Larson-Miller parameter [200]. The same approach is adopted here, which meant both experimental conditions were included as input features.

Three approaches were taken to create a GPR model for creep strength:

- Plain composition descriptors (directly analogous to the plain method described above).
- Physical descriptor set derived from the input composition only (analogous to the descriptors used for modelling phase fraction).
- Physical and metallurgical descriptors derived both from the input composition and from the fitted GPR phase chemistry model.

Atomistic microstructural properties, in combination with precipitate morphology, are known to determine the physical mechanisms by which creep occurs [3, 33]. This motivated the use of the third model. In this model the precipitate fraction predicted by the phase chemistry model was used directly as a descriptor. Other derived descriptors were used: the lattice misfit between the two phases was calculated using the Vegard coefficients [19, 217, 218]. The matrix phase stacking fault energies were approximated using fcc and hcp formation energies for each element [3, 94, 106, 219]. The formation energies were calculated via density functional theory using the PBSE SOL functional [220]. The mean and standard deviation of melting points for elements in the precipitate phase were included as proxies for the γ' solvus [156, 221]. The mean interdiffusivity metric and the mean metal d-level metrics used in the alloys-by-design procedure were also used as descriptors [19, 20, 25, 222, 223]. The necessary phase chemsity predictions were made using the GPR model described in the previous sections, trained on the full phase chemistry database excluding any entries overlapping with the creep rupture life dataset.

This GPR model incorporated more explicit high-level domain knowledge than any of the other models, which was only possible because the physical mechanisms that govern creep deformation have been well studied by metallurgists. However, the descriptors of this type that were used are not an exhaustive list, and for this reason physics-based descriptors that did not use explicit metallurgical domain knowledge were also used in this model (see Fig. 5.8).

5.3 Results

With the data curated, descriptors selected, and machine learning formalism in place, the next step is to test the performance of the machine learning algorithms. First, the

performance of phase chemistry prediction is studied, before turning to study the creep strength.

Table 5.1: Comparison of the root mean squared error (RMSE) for different components between the GPR model using descriptors and that using plain composition.

		Phase frac. (at. %)	Composition (at. %)					
			Ni	Cr	Co	Al	Ti	Heavy els.
Phase 1	Descriptor method	-	4.8	4.8	3.4	1.7	1.2	0.6
	Plain method	-	5.4	5.2	3.2	1.6	1.3	0.6
Phase 2	Descriptor method	4.4	3.8	2.7	2.7	2.4	1.5	0.5
	Plain method	6.3	3.8	3.0	3.0	2.4	2.0	0.6

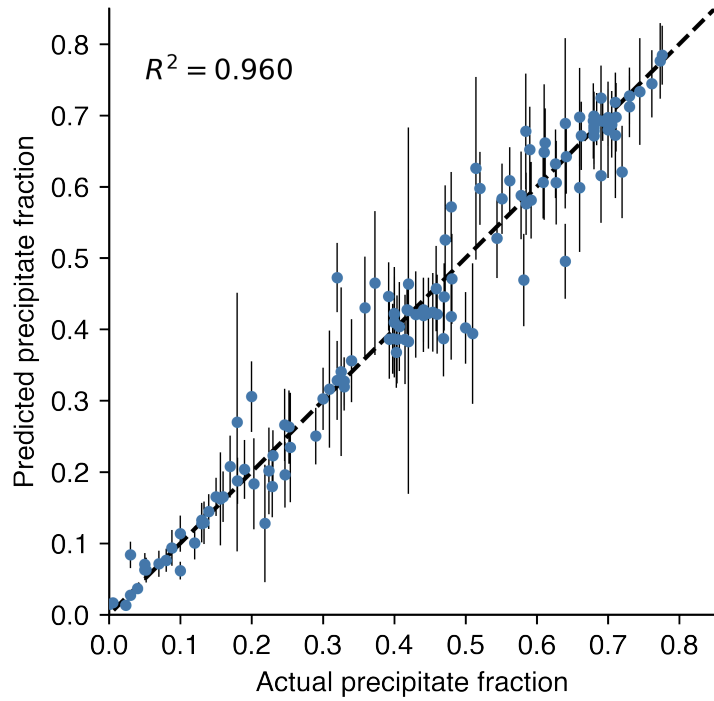


Figure 5.3: Predicted precipitate fractions from the descriptor model versus the actual values. The vertical bars are the model’s uncertainties.

To compare the performance of the proposed physical-descriptor model to the plain model that uses composition features, two rounds of tests on the phase chemistry data were performed: firstly on blind validation data where all elements had been present in the training data, and secondly for extrapolating to new materials that contain fresh elements not present in the training dataset.

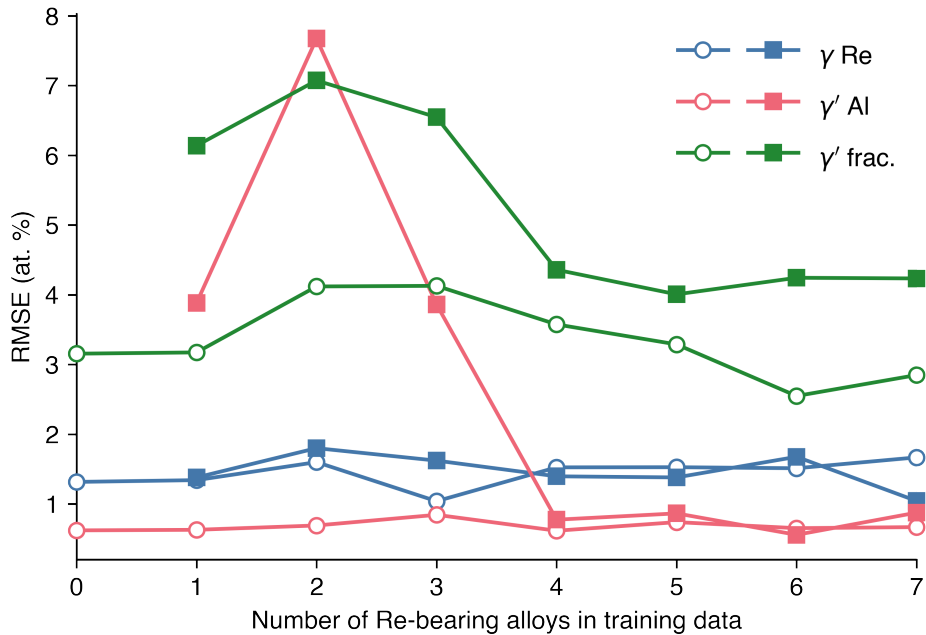


Figure 5.4: Predictions on a test dataset of Re bearing superalloys made by models trained on a dataset of 85 superalloys without Re plus a number of alloys with Re (indicated on the x-axis). The points with open-circles are the physical descriptor model and with squares are the plain composition descriptor model.

5.3.1 Performance when all elements available

First, the performance of the physical descriptor model is tested when information about all elements is available at training. Two models were trained: one that uses physical descriptors as inputs and a second that inputs the plain composition. Ten-fold cross validation was carried out on the available phase chemistry data (123 database entries). For each fold, the model was trained via log-likelihood maximisation over the training dataset, then predictions were made on the withheld validation set. These results were combined to give a single set of predictions for the entire dataset. The correction method from section 5.2.4 was applied in the same way to both models.

The root mean squared error (RMSE) was used to compare the two models due to its ease of interpretation for percentage-like properties. The RMSE for each element and fraction component of the phase chemistry is given in Table 5.1. The physical descriptor model was significantly better than the plain composition model for predicting phase fraction, improving the RMSE from 6.3% to 4.4%. The predicted versus actual phase fraction is plotted in Fig. 5.3, which confirms not only the quality of predictions, but also the accuracy of the uncertainty estimates. The phase fraction is the most crucial measure of a superalloy's microstructure given its physical influence on yield and creep strength. The descriptor-based model shows a smaller improvement for phase composition

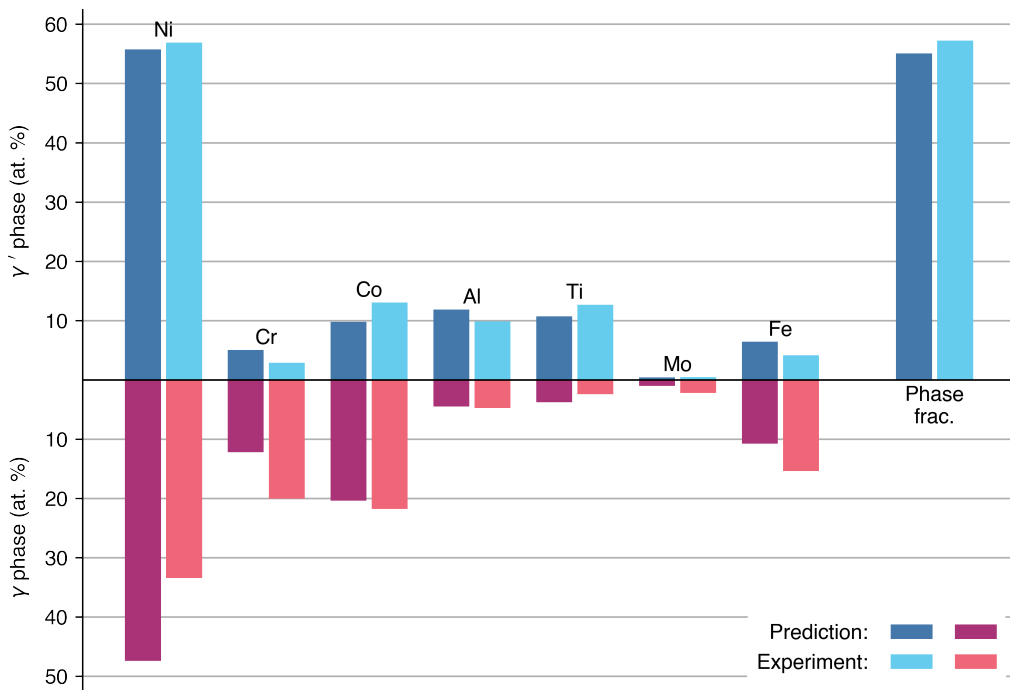


Figure 5.5: Predictions for the phase composition of a high-entropy superalloy (HESA) [224] from the physical descriptor model.

predictions when compared with the plain method, although it does still achieve the same or better RMSE for almost every element.

The selected kernel hyperparameters were also confirmed. A Matérn kernel with smoothness parameter $\nu = 2.5$ gave the best results for the log partitioning coefficient models and the phase fraction model. The fact that a smoother kernel gives better predictions when using physical descriptors is because the the models are ‘forced’ to find the best physical descriptors rather than relying on the kernel’s complexity to fit the data. In turn, the combination of a simpler, smoother model with a superior ‘understanding’ of chemistry allows the model to extrapolate well.

5.3.2 Extrapolative predictions in composition-space

To test whether descriptors improve the ability of the model to extrapolate in composition-space, the simple approach of testing our GPR model on superalloy families outside the training dataset was adopted. Two categories of alloys are focused on: Re/Ru-bearing Ni-superalloys, and high-entropy superalloys (HESA).

The addition of Re and Ru to commercial superalloy compositions was one of the key innovations of the most recent generations of conventionally developed single-crystal superalloys [3, 226–228]. Here, the training process is repeated, starting from a database

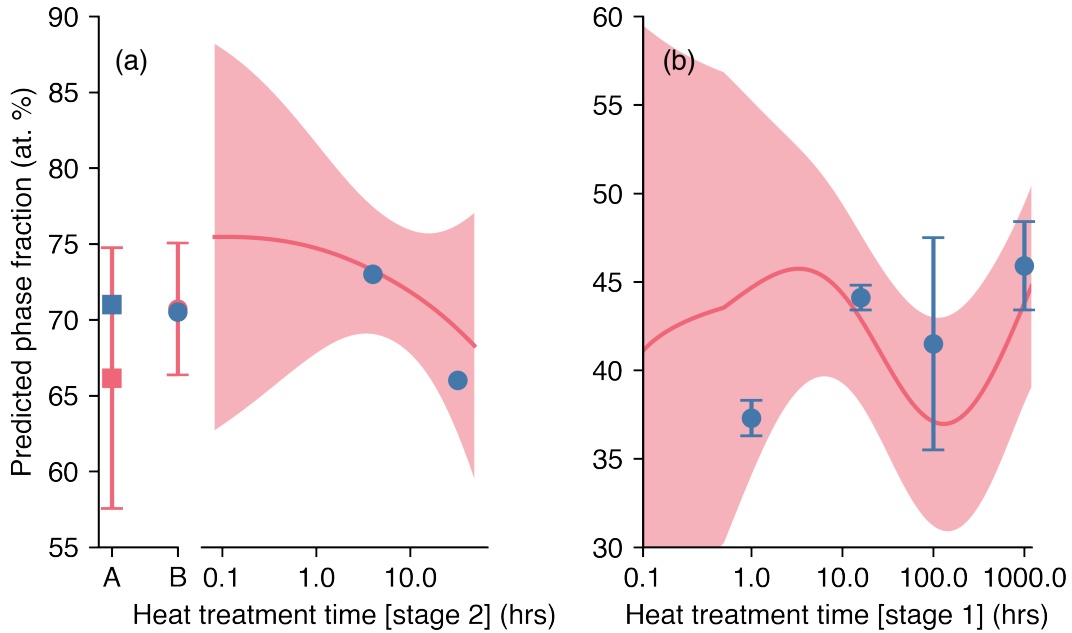


Figure 5.6: Predicted (red points/series) and experimental (blue points) data for phase fraction evolution with applied heat treatments in two superalloys. The vertical bars and shaded region give the standard uncertainty in the model’s predictions. (a) the commercial superalloy SRR99. Point A is for a sample that has only had a solid solution heat treatment applied, point B has undergone a single precipitation heat treatment at 870°C, and all following data points have undergone the same 870°C heat treatment preceded by a 1080°C heat treatment for the time indicated [86]. (b) an experimental superalloy. Each alloy has undergone a single precipitation heat treatment at 760°C for the number of hours indicated [225].

comprising 88 historic superalloys that contain neither Re nor Ru. Of the data on contemporary superalloys containing Re and Ru, 6 were randomly selected to form a test set, and the remaining were added incrementally to the training set so as to expose the importance of adding fresh alloys during a research project. Fig. 5.4 shows the RMSE vs. number of Re-bearing alloys in the training data. The initial predictions by the physical descriptor model are extremely impressive, giving about the same RMSE on the test data as it attains with any amount of Re-bearing alloy data. When a few data-points for Re alloys are added, the plain-descriptor model overfits so gives a higher RMSE than the physical descriptor model. For the crucial prediction of the γ' phase fraction, this improvement persists up to the maximum number of additional training data points.

High-entropy superalloys are a more recent development in alloy design, combining the design principles of high-entropy alloys and precipitation-strengthened alloys [224, 229]. HESAs typically contain Fe as one of their entropy of mixing-boosting components. For a review on HESAs see Ref. [205]. HESAs are a prime target for the physical descriptor model owing to the large number of element permutations that cannot all be

represented in the training dataset. The GPR model was trained on the full conventional superalloy database, that did not contain a single HESA entry, nor any entries containing Fe. The model was then tested on the HESA data collected by Zhang et al [224] that includes Fe-bearing superalloys, with results shown in Fig. 5.5. The results are overall in excellent agreement, capturing the behaviour of the elements known to the model well, and notably making good predictions for Fe, which would have been impossible with the plain descriptor model. For both experimental HESAs, the RMSE for γ' phase elements was 1.8% and for γ phase elements was 7.0%. Once again, predictions for the γ' phase are better than for the γ phase, reflecting the stronger influence of physical factors on this phase's formation. Such a prediction would be simply impossible to make with a plain composition descriptor model.

5.3.3 Heat treatments

To assess how well our heat treatment descriptors (Eq. 5.1) capture the evolution of phase chemistry during a heat treatment, the model is tested against two sets of experimental data [86, 225]. In each case, the physical descriptor model was retrained on the full database excluding the respective set of test alloys.

The first test case was a commercial superalloy SRR99, aged under a variety of conditions. Our model captured both the qualitative and quantitative trends in the evolution of the γ' fraction, see Fig. 5.6(a). Surprisingly, it exhibited both the largest uncertainty and error for heat treatment A, the un-aged specimen. This could be reflective of a spurious correlation in the training data, since data for commercial superalloy phase chemistries are typically presented for fully heat treated specimens, whereas “experimental” alloy compositions are less frequently fully heat treated.

The second test case was for an experimental five-component superalloy, where each specimen was aged at 760°C for increasingly long durations, shown in Fig. 5.6(b). Our model captured not only the trend towards an increased γ' phase fraction with treatment time, but also the observed decrease in precipitate fraction at intermediate ageing times. It captured this qualitative trend despite the fact that it is opposite to that observed for the alloy SRR99; which furthermore was one of the only alloys in the training data with more than two different heat treatments applied to the same composition. Our new proposed physical description of heat treatments, Eq. 5.1, outperformed other descriptors for both test datasets, including a plain time and temperature descriptor and other Ostwald ripening-based descriptors, as well as giving better results for the five-fold cross-validation testing described above.

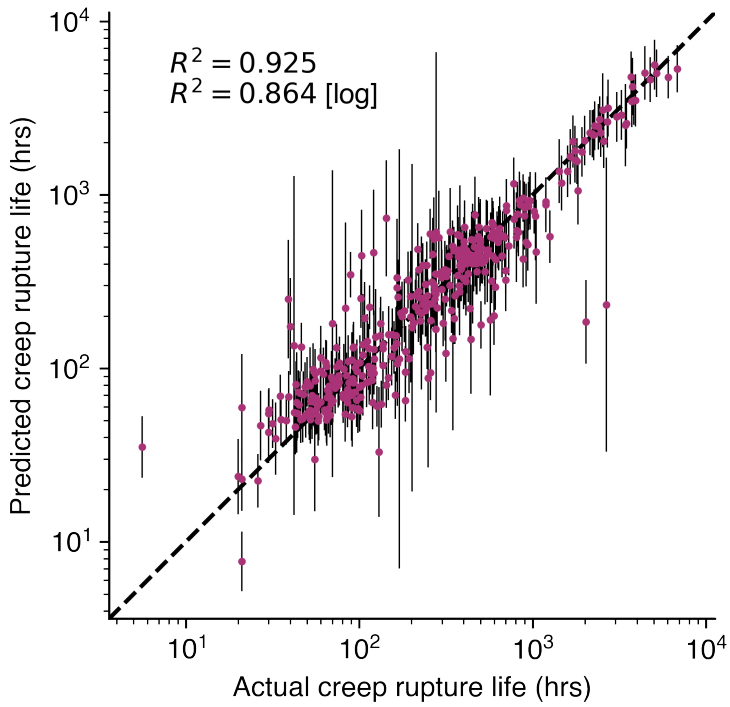


Figure 5.7: Predicted creep rupture life from a descriptor model including phase chemistry-based descriptors. The vertical bars are the model’s uncertainties.

5.3.4 Creep rupture life model

GPR models for the creep rupture life of signal crystal superalloys were trained. The accuracy of each model was assessed with ten-fold cross validation in the manner described in subsection 5.3.1. As the creep rupture life data spans multiple orders of magnitude, R^2 scores are given for both the actual values and log values. An ARD Matérn kernel was used in the Gaussian processes; but for the creep models, unlike those for phase chemistry, the optimal kernel smoothness parameter was found to be $\nu = 1.5$. The decreased smoothness of the kernel is likely because creep rupture life data spans multiple scales and testing regimes. For example, it is known that creep in single crystal superalloys occurs by two main mechanisms, dislocation and diffusion creep, with the former mechanism dominating at low temperatures and the latter at high temperatures.

Table 5.2: A summary of the coefficients of determination for GPR models of creep rupture life using different descriptors.

Descriptors	R^2
Physics + metallurgy-based descriptor method	0.864
Physics-based descriptor method	0.856
Plain method	0.840

Firstly, a plain composition descriptor GPR model was trained, which achieved $R^2 =$

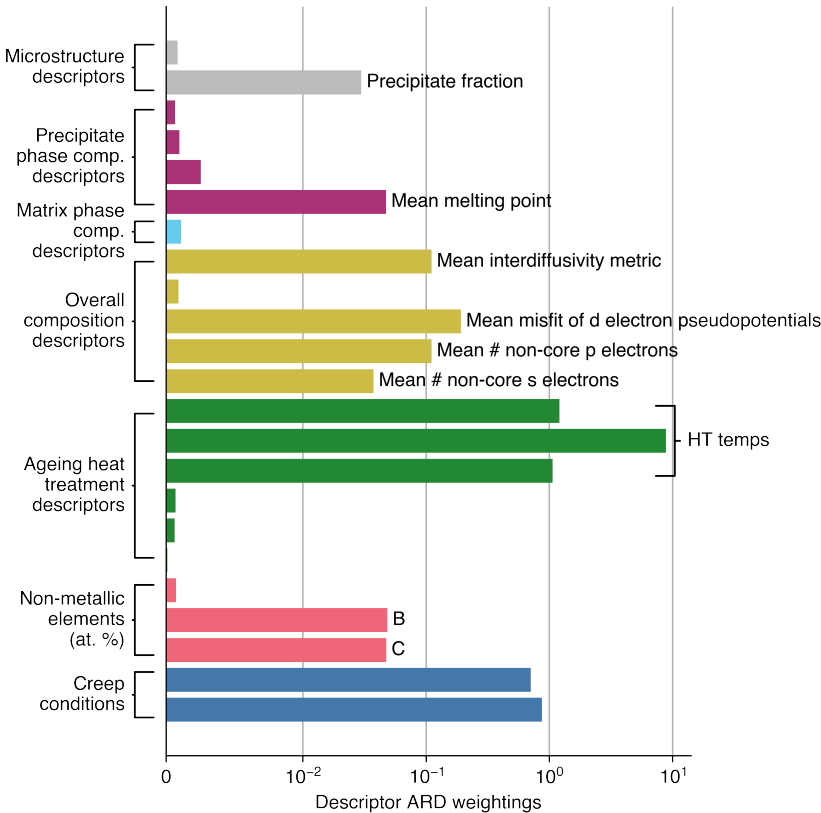


Figure 5.8: Feature weightings (inverse of ARD lengthscales) determined for a creep rupture life model trained on the full dataset.

0.840. Next, a model using a similar physics-based descriptor set to that used for phase chemistry, i.e. using descriptors calculated solely from each alloy’s nominal overall composition, was trained. This delivered an improvement on the plain descriptor method, achieving $R^2 = 0.856$.

This physics-based descriptor set was then further refined to include more high-level domain knowledge, summarised in Fig. 5.8. Metallurgy-based descriptors developed in Section 5.2.5 were added, some of which were calculated using phase compositions and fractions predicted by the pre-trained phase chemistry model described in the preceding sections. This model achieved a further improvement of $R^2 = 0.864$ (Fig. 5.7).

The relevance of various descriptors in this model as determined by the ARD kernel lengthscales are given in Fig. 5.8. Many of the expected important descriptors are found to be relevant: the precipitate fraction, the overall mean interdiffusivity, and the mean melting point of the precipitate phase are selected. However, other descriptors that were expected to be highly relevant are not selected, including the lattice misfit, mean metal d-level, and the matrix phase stacking fault energy (SFE). The mean metal d-level is a metric used to estimate susceptibility to TCP phase formation during creep: commercial single-crystal superalloys have long been designed to avoid this behaviour, which will limit the influence of this descriptor for a model fitted to a dataset of largely

commercial superalloys. The matrix SFE descriptor is unlikely to be sufficiently accurate: our estimate used an average of the difference between zero-point formation energies. This neglects thermal effects and uses an approximation to the SFE in fcc alloys. The lattice misfit is likely found to be irrelevant for both of those reasons. Of the non-metallic trace elements, the B and C at. % are relevant, whereas Y is not. The same heat treatment descriptors used for the phase chemistry modelling were again used, but the Ostwald ripening inspired descriptors that were key to capturing phase chemistry evolution with ageing are not found to be relevant (although it should be noted that they indirectly enter the model via the predicted precipitate fraction descriptor). Three physics-based descriptors calculated from the nominal composition are found to be relevant. They are three descriptors that are also selected by the phase chemistry GPR model, so they may be relevant due to their influence on microstructure morphology, which is not explicitly modelled.

5.4 Conclusion

In this chapter a set of physical descriptors for composition and heat treatment have been proposed for use in machine learning models of superalloy phase chemistry. A model using physical descriptors outperforms a model using plain composition descriptors when making *interpolative* predictions, see Table 5.1. Furthermore, when making *extrapolative* predictions, the model significantly outperforms the plain descriptor model, notably not suffering from such a severe overfitting effect (Fig. 5.4). Moreover, it can also make predictions for alloys containing elements that were not even present in its training dataset (Fig. 5.5). Such predictions are completely impossible to make using a plain descriptor model since they are not *element-agnostic*. This means the model can make useful predictions for cutting-edge superalloys, such as high-entropy superalloys or superalloys containing new heavy elements.

As well as standing up on its own, the model has a number of advantages over traditional CALPHAD. Previously identified benefits include the ability to easily retrain the GPR model, incorporate non-equilibrium features such as heat treatments, and most importantly its inherent quantification of uncertainties [1]. The model presented in this chapter captures both qualitative and quantitative effects of ageing on phase chemistry, see Fig. 5.6(a–b). A further benefit of the model is that it is possible to easily incorporate computational data, whilst still treating it as distinct from empirical data. This can be achieved by simply adding an extra feature to the inputs: a binary descriptor encoding the method by which an entry has been obtained. The process of fitting the Gaussian process will determine how relevant the computational composition data is to predicting ‘true’ compositions.

In addition to the phase chemistry model, a GPR model for the creep rupture life

of single crystal nickel superalloys has been developed. This model builds on that developed for phase chemistry in two ways. Firstly, it explicitly incorporates predictions of the phase chemistry model as descriptors, and finds them to be relevant to making predictions, providing a direct use-case for the usefulness of the GPR approach. Secondly, it expands on the domain knowledge paradigm by making use of descriptors that encapsulate metallurgical theories and principles. By incorporating such high-level domain knowledge, the ARD lengthscales of the fitted Gaussian process can be used to infer greater physical understanding about the properties it models. With a coefficient of determination of $R^2 = 0.864$ for the log creep rupture lifes, this model is itself useful for making predictions of this key strength property of single crystal superalloys. Like the phase chemistry model, its predictions include uncertainties, a crucial feature for its intended usage in alloy design [1, 188, 189].

Currently the model only calculates partitioning into two pre-determined phases, a use-case that has been identified as most critical to superalloy design. Other authors have constructed machine learning models to classify alloys by phase stability [172]. This points towards development of a fully-fledged, generic, and probabilistic approach to the Calculation of Phase Diagrams problem. Beyond alloys, this approach could be extended to phase separation in other systems including polymer/polymer, polymer/filler, and aqueous two-phase mixtures [230–233].

5.A Appendix: supplementary work to paper

5.A.1 Bayesian correction for constraints

Calculating the Bayesian correction described in Section 5.2.4 is equivalent to minimising the following Lagrangian expanded to second order in the small corrections:

$$\begin{aligned} \mathcal{L} = & \exp \left[-\frac{1}{2} \Delta \mathbf{q}^T \Sigma_q \Delta \mathbf{q} \right] \prod_{\phi} \exp \left[-\frac{1}{2} \Delta \mathbf{p}^{\phi T} \Sigma_{p^{\phi}} \Delta \mathbf{p}^{\phi} \right] \\ & \cdot \prod_i \exp \left[-\frac{1}{2} \left(\frac{x_i - \sum_{\psi} \frac{1}{2} (\tanh(\hat{q}^{\psi} + \Delta q^{\psi}) - 1) \exp(\hat{p}_i^{\psi} + \Delta p_i^{\psi})}{\tau_i x_i + \sigma_i^{(3)}} \right)^2 \right] \\ & + \sum_{\phi} \nu^{\phi} \left(1 - \sum \exp(\hat{p}_i^{\phi} + \Delta p_i^{\phi}) \right) , \end{aligned} \quad (\text{A1})$$

with respect to the components of $\Delta \mathbf{p}^{\phi}$, $\Delta \mathbf{q}$, and ν^{ϕ} , then solving the resulting system of linear equations. Note that the second constraint, E.g 5.3, is enforced simply by making an arbitrary choice to make predictions for just one of the two alloy phases (the precipitate phase in this work); from now on it shall be continued to assume the alloy has just two phases. The resulting system of linear equations whose solution gives the

correction vector $\Delta \mathbf{p}'$ can be written as:

$$\left[\left(\text{diag} (\Sigma_q, \Sigma_{p^{(1)}}, \Sigma_{p^{(2)}}) \right)^{-1} + A_m \right] \Delta \mathbf{p}' = \mathbf{b}_m . \quad (\text{A2})$$

Where the matrix A_m and vector \mathbf{b}_m are calculated by minimising Eq. A1. The formula for each of these depends on the number of non-zero alloy elements m . For speed of calculation purposes, formulas for A_m and \mathbf{b}_m up to $m = 20$ were pre-computed using the SymPy python library [234], then stored. The rank of Eq. A2 is $2m + 2$, and since the number of alloy components is typically small, the correction can be rapidly solved at time-of-prediction.

5.A.2 Further analysis of the phase chemistry GPR model

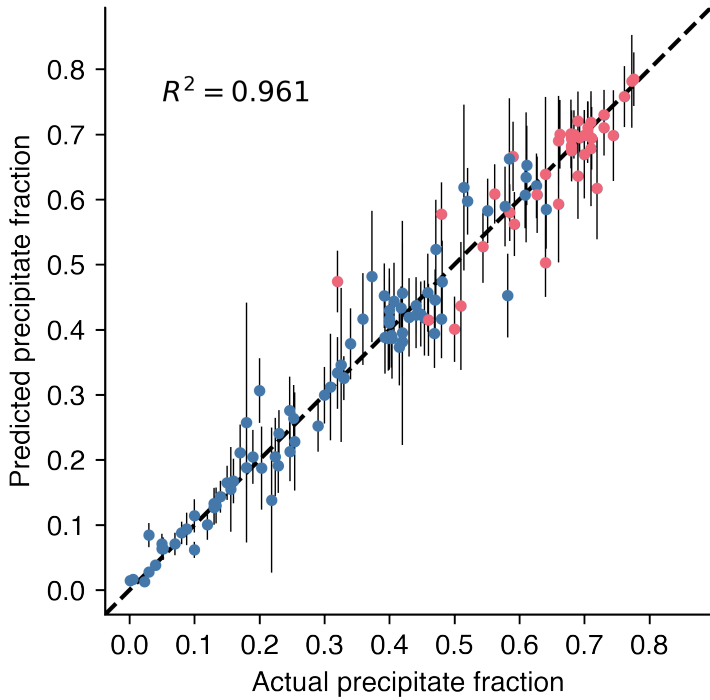


Figure A1: Predicted precipitate fractions from the descriptor model versus the actual values. The vertical bars are the model's uncertainties. Colours indicate casting type (blue for conventional casting, red for single crystal).

In the phase chemistry model, both single crystal and conventionally cast polycrystalline superalloys were used in the training dataset without distinction. Their distribution in the dataset is shown in Fig. 3.3. In order to test the validity of this assumption, the phase chemistry model was retrained with the inclusion of an extra descriptor categorising each alloy based on the nature of its casting. All other methods were the same as described in Section 5.3. The resulting ten-fold validated model for precipitate fraction

is shown in Fig. A1; The R^2 was improved by just 0.001 (compare with Fig. 5.3). The RMSE values for phase composition saw a similar improvement of about 0.1% for the first phase, and none for the second phase (compare with Table 5.1).

The corresponding feature ARD lengthscales (obtained from a phase chemistry model trained on all the training data) are shown in Fig. A2. The lengthscale that corresponds to casting type is found to be very long, implying low relevance for this feature. From a metallurgical perspective, this suggests that, after being correctly solution heat treated, and any subsequent precipitation heat treatments, the way a superalloy was cast has little impact on the resulting phase chemistry.

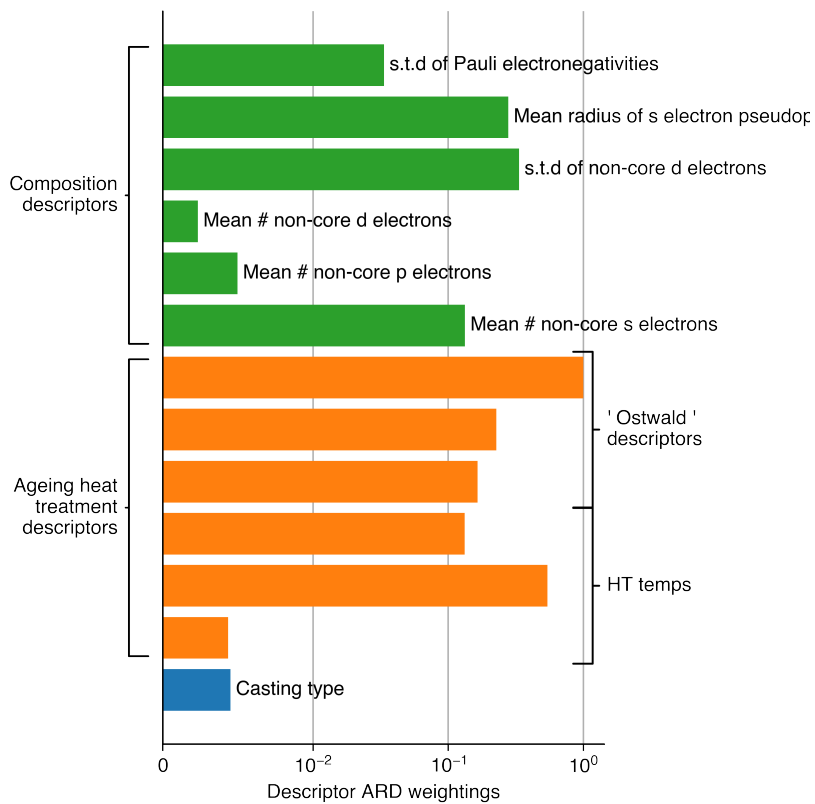


Figure A2: Descriptor ARD lengthscales in the phase fraction GPR model, including a categorical descriptor for casting type.

5.A.3 GPR model of solidus and liquidus temperatures

The solidus and liquidus temperatures of nickel superalloys play an important role in characterising their printability for additive manufacturing purposes [25, 235]. The solidus and γ' solvus temperatures give an effective window for solutioning heat treatments [33]. For these reasons, melting temperature models are crucial to the design of conventional and next-generation superalloys.

As described in Section 3.2, the database included around 52 datapoints each for

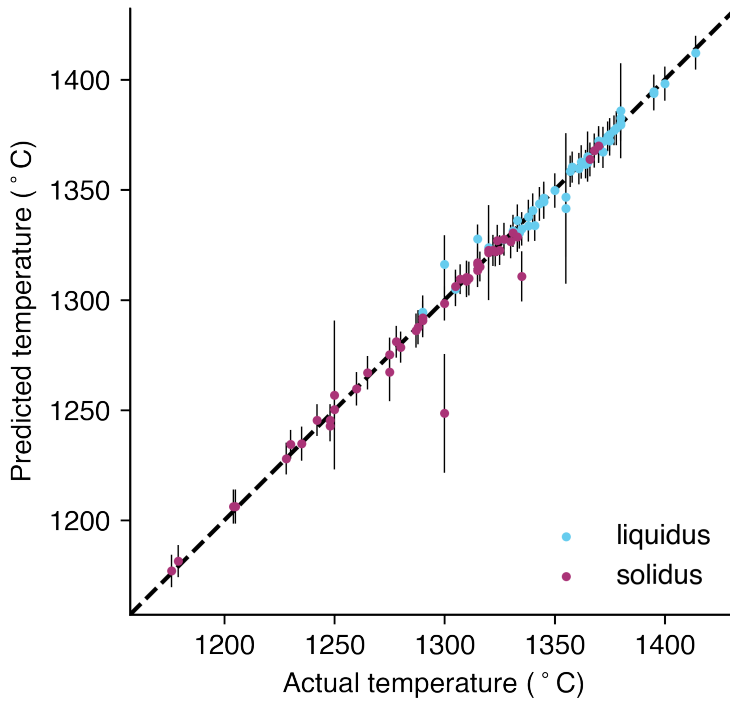


Figure A3: Predicted melting temperatures for 52 superalloys.

superalloy solidus and liquidus temperatures. A GPR model was trained to predict both temperatures at once, using the GP–MOGP equivalence described in Section 5.2.1. The input alloy compositions were mapped to physical descriptors; heat treatments were neglected from the description.

The predictions of the trained GPR model are shown in Fig. A3. A RMSE of 8.5°C and 4.4°C was attained for the solidus and liquidus values respectively. The small descriptor set was chosen by mixing the “best” (highest-weighted) descriptors for the phase chemistry GPR models with physically motivated descriptors based on the elemental melting temperatures (T_m). The descriptor set was then refined by removing less relevant features, which left just a single descriptor based on T_m . Fig. A4 summarises the ARD lengthscales for the optimal GPR model. The “type” descriptor refers to the label used to distinguish solidus/liquidus predictions.

The GPR model for melting points demonstrates that a very small number of carefully chosen descriptors can lead to a very accurate model for simple properties.

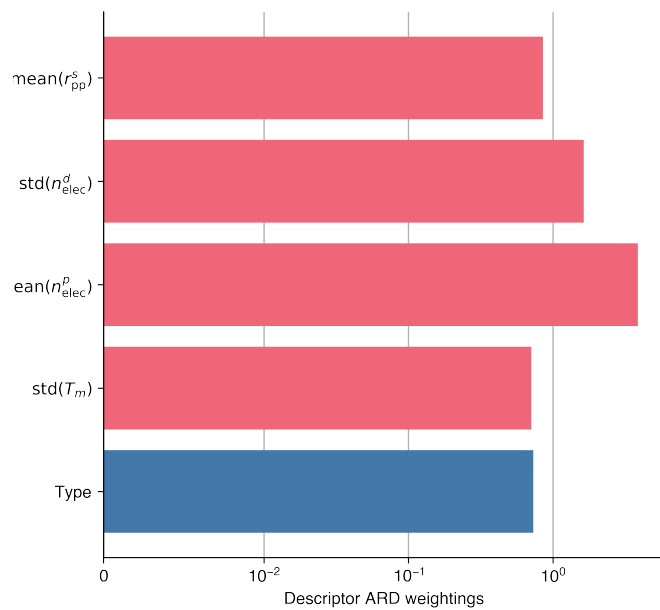


Figure A4: Descriptor ARD lengthscales in the combined solidus-liquidus GPR model.

Chapter 6

Designing a new superalloy

6.1 Introduction

The preceding chapters have concerned the development of machine learning models of superalloy phase chemistry and single crystal superalloy creep strength. The goal of this chapter is to demonstrate a proof of concept of how these models can be used to design a new superalloy to a given criteria. The chapter is presented as a case study, focusing not only on selecting compositions and heat treatments with optimal properties, but also on how to make use of uncertainties and statistical analysis in a way that can aid the designer. This means leveraging the full predictive and probabilistic capabilities of the machine learning models to find candidate alloys that are both novel and likely to meet the desired design criteria.

A review into superalloy design was carried out in Section 2.3. This chapter makes use of the probabilistic cost function approach described by Conduit et al [8, 10], and draws on alloy design principles used by all of the researchers referenced in Section 2.3 [10, 19, 20, 111, 236].

6.1.1 Design criteria

For proof-of-concept purposes, the decision was made to focus on creep rupture life as the primary strength property to select an alloy against—other authors have noted that the overall trend in single-crystal superalloy design has been towards optimising for this property [3]. Density is also an important thermomechanical property: lower mass turbine

Table 6.1: The composition of two third generation single crystal superalloys [236].

Alloy	Composition (wt. %)											Density (g/cm ³)
	Ni	Cr	Co	Mo	W	Ta	Re	Nb	Al	Ti	Hf	
CMSX-10	Bal.	2	3	0.4	5	8	6	0.1	5.7	0.2	0.03	9.05
René N6	Bal.	4.2	12.5	1.4	6	7.2	5.4	-	5.75	-	0.15	8.98

Table 6.2: Criteria for the alloy designed in this section.

Property			Target	Rationale	
Creep rupture life (hrs)	913 °C	360 MPa	> 1510	CMSX-10	[236]
		280 MPa	> 3990	CMSX-10	[236]
	1010 °C	250 MPa	> 346	CMSX-10	[236]
		145 MPa	> 2970	CMSX-10	[236]
Density (g/cm ³)			< 8.14	CMSX-10 (10% reduction)	[236]
TCP formation metric	Overall		< 0.980	Critical value	[19, 156]
	γ phase		< 0.903	Critical value	[19, 156]
γ' phase fraction (at. %)			> 60	Suggested for SX superalloys	[3, 33]

blades have smaller moments of inertia and hence experience less stress. And fortunately, these are also properties for which models were developed in Chapter 5. A direct GPR model for creep rupture life was developed, whilst density is simple to calculate from microchemistry predictions using a lever rule, see subsequent Section 6.2.

The design criteria used in this research are based on the third generation commercial superalloy CMSX-10, a proprietary alloy of the Canon-Muskegon Corporation [236]. CMSX-10 has a long creep rupture life at elevated temperatures, but also a very high density, owing to the comparatively high concentrations of heavy elements in its composition: see Table 6.1. For this reason, the design criteria for the new alloy was chosen to be the same elevated temperature creep rupture life as CMSX-10, with a 10% lower density. It was hoped that by choosing an ambitious target, the optimisation tool would be pushed to explore a comparatively extrapolative region in composition space and hence select a more novel alloy composition as optimal.

An inspection of the feature relevance in the GPR model for creep rupture life—see Fig. 5.8 and surrounding discussion—reveals that the precipitate fraction and TCP phase formation metrics are given comparatively little weight compared to what would be expected from the literature on single crystal superalloy design [3, 19, 33, 156]. This reflects a bias in the data that arises due to the fact that commercial single crystal superalloys have typically already been designed with these criteria in mind. For this reason, the design criteria also included constraints on the mean metal-d level for both the overall composition and the γ phase, as well as a preference for a large γ' phase fraction between 60% and 75%. The full design criteria are given in Table 6.2.

The bounds on composition and heat treatments supplied to the optimiser were chosen to be broadly reflective of the commercial single crystal superalloys included in the database, see Chapter 3. Since the chosen design criteria did not include hot corrosion resistance, it was decided to use a comparatively high lower bound on Cr content, and to exclude Ti from the considered components. A full list of bounds on heat treatments and

Table 6.3: Optimiser bounds for the various alloy components.

	1st precipitation		2nd precipitation	
	heat treatment	Temp. (°C)	heat treatment	Time (hrs)
Bounds	900–1180	0.5–12	800–1160	0.5–48
	Composition (wt. %)			
	Ni	Cr	Co	Re
Bounds	> 0.485	5.0–24.6	0.0–19.0	0.0–7.5
	Composition (wt. %) cont.			
	W	Mo	Nb	Hf
Bounds	0.0–18.6	0.0–22.2	0.0–2.6	0.0–5.6
	Composition (wt. %) cont.			
	C	B		Y
Bounds	0.0–0.7	0.0–0.3		0.0–0.04

compositions is given in Table 6.3.

6.2 Computational method

The quantity that the alloy was optimised for was the log probability of criteria fulfilment [10], $\log(p_c)$. Specifically, this quantity was maximised. It is calculated using the predictions for each target in the criteria \mathbf{f}_c , and the associated covariance matrix Σ_c , which fully describes the normally distributed predictions for a given trial alloy. The cumulative multivariate normal distribution function then gives the probability of fulfilling the target criteria, \mathbf{t} :

$$p_c = F((\mathbf{f}_c - \mathbf{t})^T \Sigma_c^{-1} (\mathbf{f}_c - \mathbf{t})) , \quad (6.1)$$

where it should be noted that this strictly applies to criteria that are bounded from above (maximum-type targets), and would need to be modified for minimum-type or range-type targets. For the creep predictions, the covariance matrix of the predictions returned by the GPR model was used directly. For the sake of simplicity, the predicted density, phase fraction, and mean metal-d values were treated as uncorrelated.

Minimisation of $-\log(p_c)$ was performed using simulated annealing. The `scipy` implementation of this algorithm was used (the `dual_annealing` function was used with the `no_local_search` option switched on) [237–240]. Trial alloy compositions excluded the balance element Ni; since the `scipy` implementation of simulated annealing does not allow for linear constraints on the inputs, the objective function was setup to return a very large number whenever a trial composition was chosen that would sum up to a value exceeding the lower bound on the balance component.

After some experimentation, it was found that the optimal parameters for the sim-

ulated annealing algorithm was a high initial temperature, $T_q(0) = 5.0 \times 10^4$ and a low visiting parameter $q_v = 1.5$. This combination makes sense, since a large part of the optimisation landscape is effectively out of bounds due to the pseudo-constraint on composition. A high temperature ensures the whole landscape is explored, whilst a low visiting parameter means the algorithm will rapidly hone in on the viable regions.

6.3 Results

Table 6.4: The selected heat treatments and composition (wt. % and at. %) of the optimised superalloy.

	1st precipitation heat treatment		2nd precipitation heat treatment		Composition (wt. %)										
	Temp (°C)	Time (hrs)	Temp (°C)	Time (hrs)	Ni	Cr	Co	Re	Ru	Al	Ta	W	Mo	Nb	Hf
Values	1180	0.69	872	1.12	68.8	5.0	0.2	7.5	5.4	5.5	1.2	0.7	0.1	0.1	5.4
Composition (at. %) cont.															
Values	72.7	6.0	0.2	2.5	3.3	12.6	0.4	0.3	0.1	0.1	1.9				

The superalloy and composition selected by the optimisation procedure described above is given in Table 6.4. Note that the amount of C, B and Y selected was 0% for each. The selected optimal superalloy is characterised by a relatively large amount of Re, Ru, and Hf, and a comparatively small amount of other heavy elements and also Co. The selected heat treatments use fairly standard temperatures but for short durations (41 mins and 67 mins respectively).

Predicted properties of the superalloy are shown in Table 6.5. Whilst it predicted very high creep rupture lives, the tool selected an alloy with a density far outside the desired window. This is due to difficulties estimating the uncertainties associated with density. The model used a straightforward calculation using a lever rule, atomic masses and Vegard coefficients, and each superalloy's predicted microchemistry; uncertainties were propagated through from the microchemistry uncertainties. However this method underestimates the very high degree of correlation associated with the respective phase compositions, hence dramatically overestimating density uncertainty. This leads to the tool not sufficiently penalising densities outside the criteria window.

The model predicts low values of the average metal-d level (TCP formation metric). This is because the tool selected a superalloy with high amounts of Re and Ru to promote

Table 6.5: Predicted properties of the selected optimal superalloy.

Property		Predicted value	Uncertainty region
Creep rupture life (hrs)	913 °C	360 MPa	2423 997–5887
		280 MPa	6544 3345–12,803
	1010 °C	250 MPa	585 360–951
		145 MPa	6203 3771–10,205
Density (g/cm ³)			9.040 6.665–11.415
TCP formation metric	Overall		0.968 -
γ' phase fraction (at. %)	γ phase		0.830 0.582–1.078
			75.0 20.3–97.2

creep rupture life, but offset these with a high quantity of Hf to minimise TCP formation.

Table 6.6: A comparison between the selected optimal alloy and the two most similar superalloys in the database [156].

Alloy	Composition (at. %)											
	Ni	Cr	Co	Re	Ru	Al	Ta	W	Ti	Mo	Nb	Hf
MC544	73.3	4.7	0.0	1.3	2.4	13.6	1.7	1.7	0.6	0.6	-	-
MC645	71.6	5.9	0.0	1.3	3.0	13.7	1.7	2.0	0.6	-	-	-
This work	72.7	6.0	0.2	2.5	3.3	12.6	0.4	0.3	-	0.1	0.1	1.9

In Table 6.6, the two superalloys (drawn from the database compiled in this work) with compositions most similar to the selected optimal superalloy are shown. These are MC544 and MC645 ¹ [156].

A notable feature of the GPR microchemistry model from this work is its ability to accurately capture the dependence of phase chemistry on complex multi-stage heat treatments: see Chapter 5, and in particular Fig. 5.6. For this reason, it is of interest to explore the phase fraction landscape that arises by varying each heat treatment. The γ' phase fraction as a function of heat treatments times and temperatures is shown in Fig. 6.1. In each plot, phase fraction is calculated for differing first stage or second stage heat treatments, whilst the other heat treatment remains fixed. It can be seen that both selected heat treatments produce a high γ' phase fraction. The first heat treatment is near the extreme corner of the search region, and appears to have been selected almost solely to maximise γ' phase fraction. The second heat treatment is at a similar treatment temperature to the standard for MC645, but for a shorter time which again increases γ' fraction.

A detailed analysis of creep rupture life for the selected optimal superalloy is shown via a contour plot in Fig. 6.2. Compared to other single crystal superalloys, it is predicted

¹There is a paucity of available data on these two superalloys. They are worth comparing to the selected optimal superalloy because they were both designed via a more traditional alloys-by-design type approach.

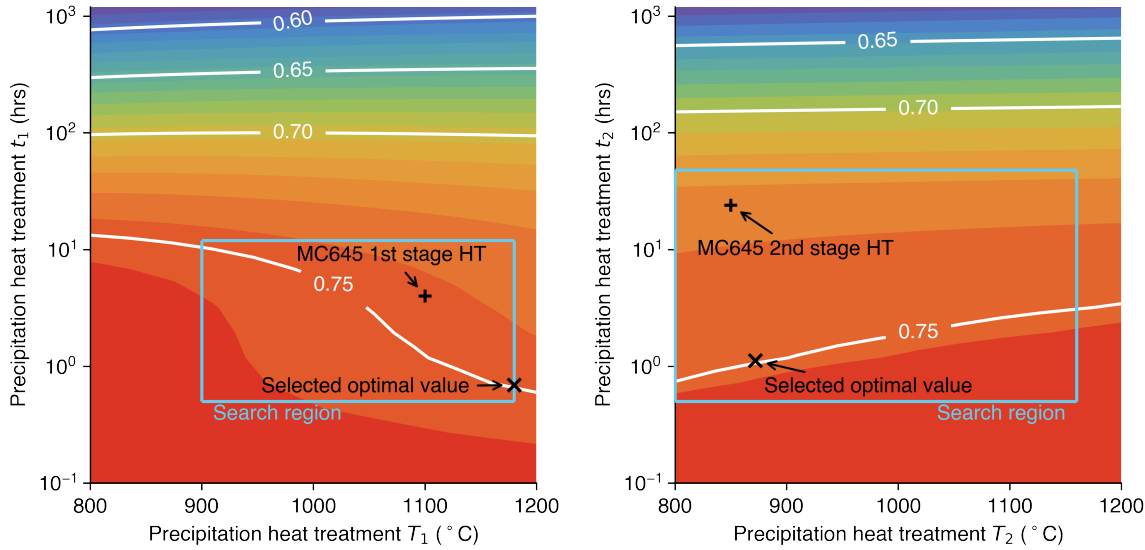


Figure 6.1: Contours plots showing how varying the first and second precipitation heat treatments effects the predicted phase fraction. The selected optimal heat treatments are marked with ‘x’.

to have a high 1000 hour creep strength capability—similar to TMS-162 and MC-NG in the low stress / high temperature regime. Note that the $t_r = 100$ hour and 1000 hour isolines show the expected Larson-Miller relationship:

$$\frac{P_{LM}}{T} = \log(t_r) + C \quad ,$$

but this breaks down for the 10,000 hour isoline, reflecting the fact that less data is available for the low temperature / low stress creep regime.

6.4 Conclusion

In this chapter, it has been demonstrated that the GPR models developed in Chapter 5 can be used to design a new superalloy to a set of criteria. The superalloy that the optimisation tool selected had both a novel composition and a novel heat treatment regimen. However, it failed to precisely fulfil some of the design criteria, notably density, which is due to the way that property’s associated uncertainty was calculated. Further work is required on this front, but one simple fix might be to use a Bayesian model for density, such as GPR or Bayesian Ridge Regression.

The optimisation tool is able to select an optimal precipitation heat treatment, due to the inclusion of heat treatments in the GPR models’ inputs. This provides an advantage over the alloy design approaches that make use of equilibrium thermodynamic modelling, such as the alloys-by-design methodology [19, 20, 25]. The necessity of this approach

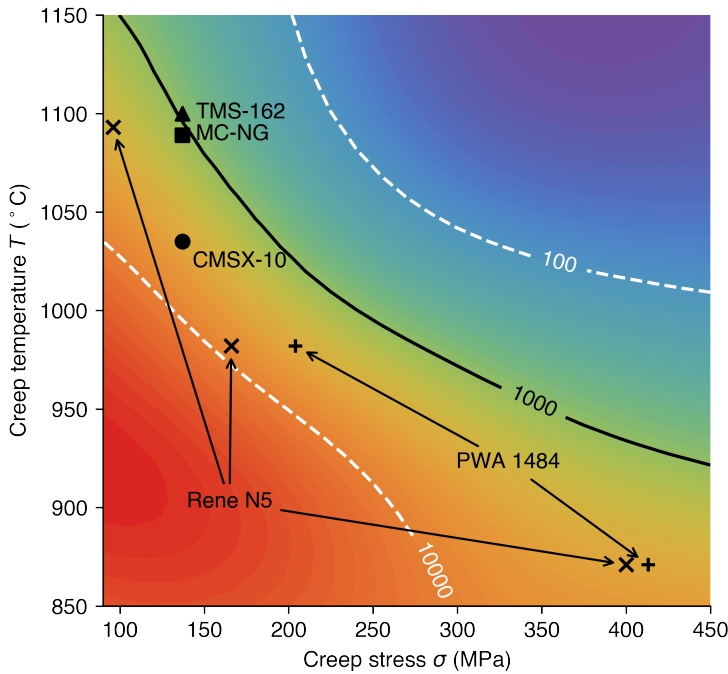


Figure 6.2: Contour plot showing the creep rupture life (hrs) of the selected alloy with creep stress and temperature. The marked points show the 1000 hour creep rupture lives of the respective named single crystal superalloys [3, 241].

is evidenced by the significant effect that different heat treatment regimens have on the superalloy that was selected here, see Fig. 6.1—it is also evident from a physical point of view that such effects cannot be decoupled from the superalloy's composition.

Chapter 7

Conclusion

This thesis has focused on the development of new machine learning models to aid superalloy design. To this end, Gaussian process regression (GPR) models have been developed for elements of superalloy phase chemistry (Chapters 4 & 5). The two phase microstructure of nickel superalloys underlies their phenomenal high temperature properties, and hence an accurate calculation of the phase separation that a particular alloy will undergo is a crucial first step towards modelling overall strength properties (Section 2.2). In addition, microstructural features such as the γ' phase fraction and the γ phase mean metal-d level feature in numerous superalloy design criterion [8, 10, 19, 20, 25, 156]. In the literature, extensive usage is made of equilibrium thermodynamic models (CALPHAD) for phase chemistry calculations [67, 161, 242]: the GPR models developed in this work have a number of advantages over such approaches, including prediction speed, re-trainability, mixing simulated and experimental training data, and uncertainty prediction (refer to Sections 4.5 & 5.4 for discussion). The GPR models also have a quantitative edge over CALPHAD models—see Table 7.1.

A full summary of the quantitative results of these new GPR models is provided in Table 7.1. In the ‘best results’ column, full interpolation tests refer to randomised ten-fold cross-validation tests carried out on the full available training dataset. Limited tests refer to tests of the models on smaller datasets, mainly for the purposes of testing their extrapolatory capability.

Physical descriptors have previously been used in machine learning models of various alloys and alloy properties, including superalloys [107, 175, 201]. In this work, a simple set of physical descriptors influenced by electronic structure-type considerations (for the microchemistry GPR model, see Section 5.2.2) and principles from the metallurgical literature on superalloys (for the creep strength model, see Section 5.2.5) have been used. These descriptors also included a physically influenced remapping of the precipitation heat treatment features; in turn, the usage of these descriptors allows the GPR microchemistry model to accurately capture the dependence of phase separation on complex multi-stage heat treatments (Section 5.3.3). The use of an ML model to accurately capture the effects

Table 7.1: A summary of the quantitative results obtained for models developed in this thesis. *Whilst comparable models exist, such as CALPHAD models, they cannot be scored on interpolation since their training datasets are unknown.

Model	Description	Input	Metric	Full interpolation test		Best results		Limited test	
				This thesis	Comparison	This thesis	Comparison	Dataset	
Phase fraction	Composition	R^2	0.943	*	2.0%	2.1% [161]		New alloys (S4.4.1)	
	Descriptor	R^2	0.961	*	3.4%	None	Heat treatment extrapolation (S5.3.2)		
Phase composition	Composition	avg. RMSE	2.68%	*	1.9%	2.0% [161]		New alloys (S4.4.1)	
	Descriptor	avg. RMSE	2.51%	*					
Creep rupture life	Composition	R^2	0.843						
	Descriptor	R^2	0.864	0.9176 [175]					

of complex, multi-stage, precipitation heat treatments is novel to this work.

In addition to phase chemistry, GPR models for the creep strength of single crystal superalloys were also developed (Sections 5.2.5 & 5.3.4). Creep strength has been a crucial design target during the development of successive generations of superalloys. The model made use of physical descriptors, including descriptors derived from the GPR phase chemistry models. This built on the work of other researchers by producing a model that yielded uncertainties associated with each prediction and was readily interpretable. The probabilistic nature of the creep rupture life model was made use of in a tool to design an optimal superalloy to a set of engineering criteria (Chapter 6). As can be seen in Table 7.1, an ML model of creep rupture life that score better on a similar dataset has been developed by other researchers [175]. However, their use of a divide-and-conquer strategy limits the interpretability of their model, as well as its ability to quantify uncertainty.

All of the GPR models in this thesis were trained using data drawn from a purpose-built open source database, that was hand-curated from existing databases (academic and industrial) and academic literature (see Section 3.2). In turn, the GPR phase chemistry tools were then used to validate the databases on which they were trained. In particular, the pre-processing that was applied to produce significant fractions of the phase chemistry data was validated (Section 3.4).

This thesis also includes some new theory. A metric for quantifying the distribution of uncertainty quality (DUQ) in a machine learning model has been expanded on and applied to the task of database validation (Section 4.3.1). Probabilistic correction methods have been developed to enforce necessary constraints (both hard and soft) on phase chemistry model predictions (Sections 4.3.2 & 5.2.4). Chapters 4 & 5 have been published in a peer reviewed journal [1, 2].

Future work

There are two routes for expansion of the work in this thesis. The first is to develop further models of superalloy properties, making use of methods from this work such as the phase chemistry corrections and use of physical descriptors. Additional properties to those modelled in this thesis, that would typically be included in the design criteria for a new alloy, include the hot corrosion resistance, yield strength, elastic properties, solidus, γ' solvus, and processability. Further measures of creep strength—time to 1% elongation, creep rates during different stages, elongation at rupture, and reduction in area at rupture—are also used to select alloys for creep strength, and have not been modelled in this work. Chapter 6 demonstrated that it is beneficial to predict various alloy properties along with a full covariance between them [8, 10]. A multi-output Gaussian process (MOGP) would naturally predict this covariance, so having regression models

output predictions for all properties included in the design criteria could easily be achieved within the framework developed in this thesis (the possible equivalence between GPR and MOGP models is illustrated in Section 5.2.1 along with Fig. 5.1).

Throughout this thesis possibility of utilising training data obtained via (expensive) computational simulations has also been discussed (e.g. Fig. 1.2). This presents another opportunity for future work on modelling superalloys. Such simulations could supplement experimental data and allow for better transferability of ML models into experimentally un-explored composition space. Recent developments in the field of machine learning interatomic potentials have opened up the possibility of carrying out useful atomistic simulations of four or five component alloys [60, 64, 65, 243]. This could be a viable area of composition space for new superalloys such as the proposed high entropy superalloys (HESAs) [205, 224, 229].

In Chapters 4 & 5, the important two-phase microstructure of nickel superalloys was modelled. Specifically, the easily quantifiable phase microchemistry. But the morphology of the microstructure also plays an important role in determining higher level properties [33]. Other researchers have modelled such microstructure based on expert categorical ratings of observed morphology [180]. An alternative approach might be to train an unsupervised model on available electron microscope imagery in order to obtain a much lower dimensional representation of said data. This can be thought of as applying a fancy principal component analysis to the raw image data. A pre-trained image encoder could even be used as a first stage of the model. It would then be possible to train a regression model to map alloy composition to this low dimensional representation of morphology, in exactly the same manner as was done for the other properties modelled in this work. The database curated in this work includes electron microscope images of superalloys, see Chapter 3 and Table 3.1, that could be used for this purpose.

The second main avenue of future work would be to extend the models developed in this thesis for use with a wider range of materials. There are a few ways to approach this. A great deal of discussion has been devoted to the ways in which model uncertainty can be assessed and made use of. Active learning is a ML strategy that makes use of model uncertainty to optimally select new alloys to augment the model's training database [244–246]. These alloys are then experimentally prepared, analysed, and tested, and the data is fed back into the ML model. This feedback loop between model and experiment would serve as an effective means of experimentally verifying the usefulness of the models in this work; and, if the models are good extrapolators, this method should lead to effective sampling of new, ‘interesting’ regions of alloy composition space, hence furthering the experimental science too.

Chapters 4 & 5 critique the CALPHAD methodology and expound GPR models as an alternative. In summary, CALPHAD models don't predict uncertainties; can't easily combine training data from a mixture of sources, such as experimental and computational

data; and are based on equilibrium thermodynamics, making it difficult to include the non-equilibrium effects such as heat treatments that are crucial in real applications of materials. GPR models don't suffer from these limitations, but the models in this thesis do not go the full way to replacing CALPHAD. They assume that the input alloys will partition into γ and γ' phases—a reasonable assumption for alloys that look like superalloys. Adding a separate ML model that first predicts which phases the input alloy will partition into would be a simple way to expand the methodology in such a way that it could fully replace CALPHAD. Just such a model has been developed by Lee et al [172].

The models in Chapter 5 make use of physical descriptors. A question for future work to answer is just how far such descriptors can allow a predictive model to transfer. Phrased in another way, would it be possible to develop a set of physical descriptors that could allow an ML model to transfer its predictions across multiple classes of alloys, including classes of alloys not included in the model's training data? Nickel superalloys belong to a larger class of alloys called precipitation strengthened alloys, which make use of similar metallurgical principles related to the role of precipitate phases in the alloy. Developing a general ML model of this class of alloys, and demonstrating its transferability to new classes of precipitation strengthened alloys, might be a suitable initial goal for such future work to pursue.

Appendix A

Embedded atom model potentials for Re and Ru

A.1 Introduction

Throughout this thesis, the discussion of machine learning approaches to superalloy modelling has included the possibility of using ‘expensive’ simulations of superalloys to supplement the available experimental data and in turn improve the transferability of the machine learning models into under-explored regions of composition space. Fig. 1.2 schematically shows how such simulations could be integrated into the overall workflow. Note that such simulations would be separate to the usage of descriptors in the ML model; the idea is that a separate simulation would be carried out for a separate input alloy composition, using a suitable simulation supercell construction. This appendix chapter contains some exploratory work towards the goal of accurately simulating superalloy properties. Following the discussion of pros and cons of various simulation approaches in Section 2.2.1, the atomistic simulation method selected for this work was molecular dynamics [230, 247–250].

A.2 Theory

Embedded atom model (EAM) potentials are one of the most common choices of potentials for simulating transition metals. EAM potentials are inspired by density functional theory: each atom is associated with a fixed electron density, with one contribution to the energy coming from the embedding of an atom within the electron cloud due to all the other atoms. The other contribution to the energy comes from an explicit two-body

interaction term [251–253]. The energy of the system is:

$$E = \sum_i F(\rho_i) + \frac{1}{2} \sum_{\substack{i, j \\ i \neq j}} \phi(r_{ij}) \quad (\text{A.1})$$

$$\rho_i = \sum_j f(r_{ij}) \quad . \quad (\text{A.2})$$

Here $\phi(r_{ij})$ is the pair interaction, $f(r)$ is the electron density associated with each atom, and $F(\rho)$ is the embedding term. Equations (A.1) and (A.2) have an associated gauge transformation [247]:

$$\phi(r) \mapsto \phi(r) - 2k f(r) \quad (\text{A.3})$$

$$f(r) \mapsto s f(r) \quad (\text{A.4})$$

$$F(\rho) \mapsto F(\rho/s) + \frac{k}{s} \rho \quad , \quad (\text{A.5})$$

with gauge parameters k, s , that preserves the total energy Eq. A.1.

This method can be extended to multi-species EAM potentials, e.g. for binary alloys of species a and b Eq. A.1 becomes:

$$E = \sum_{i^a} F^a(\rho_i) + \sum_{i^b} F^b(\rho_i) + \frac{1}{2} \sum_{\substack{i^a, j^a \\ i^a \neq j^a}} \phi^{aa}(r_{ij}) + \frac{1}{2} \sum_{\substack{i^b, j^b \\ i^b \neq j^b}} \phi^{bb}(r_{ij}) + \sum_{i^a, j^b} \phi^{ab}(r_{ij}) \quad , \quad (\text{A.6})$$

where $\phi^{ab} = \phi^{ba}$ is the inter-species pair potential. This obeys a gauge transformation $\phi^a(r) \mapsto \phi^a(r) - 2k^a f^a(r)$, $F^a(\rho) \mapsto F^a(\rho) + k^a \rho$ (and likewise for species b) so long as the inter-species pair potential is related to the two single-species pair potentials by:

$$\phi^{ab} = \frac{1}{2} \left(\frac{f^b(r)}{f^a(r)} \phi^{aa}(r) + \frac{f^a(r)}{f^b(r)} \phi^{bb}(r) \right) \quad . \quad (\text{A.7})$$

Note that there is no equivalent of the scaling gauge transformation controlled by the gauge parameter s in eqs. (A.3) to (A.5) because the embedding functions $F^a(\rho)$ and $F^b(\rho)$ are not generally linear in density ρ . Requiring the gauge transformation to hold then using Eq. A.7 to generate an inter-species pair potential from previously fitted single species pair potentials provides a simple method of generating EAM potentials for use simulating binary (or more) alloys [247, 249, 254–256].

This work uses a set of EAM potentials fitted as single element potentials, then extended to include inter-species pair potentials in the manner described above. The potentials for Ni, Co, Al, Ti, Ta, Mo, and W were developed by Zhou et al and the Cr

potential by Lin et al [249, 255, 257]. They share a common functional form:

$$\phi(r) = \frac{A \exp(-\alpha(r/r_e - 1))}{1 + (r/r_e - \kappa)^{20}} - \frac{B \exp(-\beta(r/r_e - 1))}{1 + (r/r_e - \lambda)^{20}} \quad (\text{A.8})$$

$$f(r) = \frac{f_e \exp(-\beta(r/r_e - 1))}{1 + (r/r_e - \lambda)^{20}} \quad (\text{A.9})$$

$$F(\rho) = \begin{cases} \sum_{i=0}^3 F_{ni} \left(\frac{\rho}{\rho_n} - 1 \right)^i, & \rho < \rho_n \\ \sum_{i=0}^3 F_i \left(\frac{\rho}{\rho_e} - 1 \right)^i, & \rho_n \leq \rho < \rho_o \\ F_e (1 - \eta \ln(\rho/\rho_s)) \left(\frac{\rho}{\rho_s} \right)^\eta, & \rho_o \leq \rho \end{cases}. \quad (\text{A.10})$$

The spline describing the embedding function Eq. A.10 is continuous in value, first, and second derivative. Additionally it is required that $F(0) = 0$, for obvious physical reasons, and that $F'(\rho_e) = 0$. This second requirement is due to ρ_e corresponding to the equilibrium density, and ensures that the force contribution due to the embedding function is zero at equilibrium. This is a total of 8 constraints on the embedding function, so that of the 11 parameters required to fully specify it, only 3 are independent. In original versions of the EAM, $\rho_s = \rho_e$, which leaves just two independent parameters that need to be fitted. For hcp materials, $\lambda = 1.0$, $\kappa = 2.0$. For all the materials f_e was taken to be $E_c/\Omega^{1/3}$ where E_c is the cohesive energy and Ω is the atomic volume [254]. This leaves just 6 independent parameters in the EAM potential: A , B , α , β , F_0 , η .

A.3 Development of new potentials for Re and Ru

New potentials were fitted for Re and Ru using the atomicrex code [258]. All 6 of the parameters listed above were optimised for each element. The fitted properties and experimentally determined targets are listed in table A.1. Note that the original authors did not fit the c/a ratio (only relevant for hcp materials), and instead fitted the pressure derivative of the bulk modulus. For hcp materials this has to be calculated from an equation of state fitted for the materials, which was not available for Re or Ru. The Voigt modulus is the upper bound for the shear modulus calculated from the elastic constants and for hcp materials is given by [259]:

$$G_V = \frac{1}{30} (C_{11} + C_{12} + 2C_{33} - 4C_{13} + 12C_{44} + 12C_{66}) \quad .$$

This calculated property was fitted to the actual shear modulus measured for Re and Ru. ρ_e was found via DFT—the density of a single isolated Re/Ru atom convolved with the positions of atoms in the hcp lattice.

The pair potential, Eq. A.8, and density function, Eq. A.9, include cutoff terms (the denominators). However in the functional form above the cutoff functions have an unfor-

Properties	Ru			Re		
	Target	Achieved	Error (%)	Target	Achieved	Error (%)
Cohesive energy (eV/atom)	-6.74	-6.7323	0.11	-8.03	-7.2868	9.26
Bulk modulus (GPa)	220	231.46	5.21	370	350.30	5.32
Lattice parameter (Å)	2.706	2.60261	3.82	2.761	2.74929	0.42
c/a ratio	1.582	1.63261	3.20	1.614	1.63316	1.19
Voigt shear modulus (GPa)	173	150.11	11.70	178	176.20	1.01
Vacancy formation energy (eV)	3.64	4.4495	22.24	5	6.16	23.2

Table A.1: Experimentally determined target values and those achieved for fitting new EAM potentials for Re and Ru. Vacancy formations energies from [260, 261] respectively.

tunate property which is that the cutoff function does not go to exactly zero at any point. This posed a problem when fitting using the atomicrex code which required the cutoff function to strictly reach zero at a hard cutoff value r_c for numerical reasons. For this reason the cutoff function was reparameterised as $1 - 1/(1 + ((r - r_c)/h)^m)$ by matching the mid point of the slopes and the 1st order series expansion at this point. The 1st order series expansion had to be approximately matched, again due to numerical practicalities. Both cutoff functions are shown in Fig. A.1.

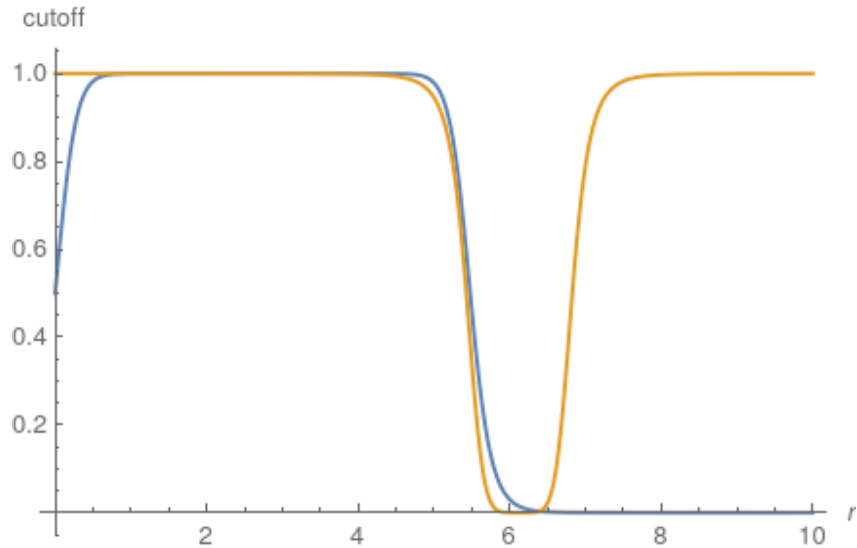


Figure A.1: Original EAM cutoff function in blue and reparameterised cutoff in orange.

The procedure above fits potentials to properties of pure materials, then Eq. A.7 can be used to extend the potentials to any arbitrary combination of elements, without any extra fitting. This was found to produce quite poor potentials for Ni-Re and Ni-Ru.

However eqs. (A.3) to (A.5) give a method to systematically improve the inter-species potentials since they are a gauge transformation for pure elements (energy given by Eq. A.1) but not for binary alloys (energy given by Eq. A.6). Note that this is only the case if $s \neq 1$, otherwise eqs. (A.3) to (A.5) are still gauge transformations for Eq. A.6. Therefore it is possible to optimise s^a, k^a for a certain element to better fit alloy properties without affecting the already fitted properties for the pure elements.

This fitting procedure was implemented using a dual annealing optimisation strategy [262–264]. The objective function to minimise was chosen to be:

$$\sum_i \left(\frac{y_i(k, s) - \hat{y}_i}{\epsilon_i} \right)^2 ,$$

where i indexes the target properties, \hat{y}_i is the target property and y_i the calculated property, and ϵ_i is the tolerance for a given target. It was then used to fit Ni–Re and Ni–Ru potentials by optimising s^{Re} , k^{Re} , s^{Ru} , k^{Ru} . The target properties to fit to were obtained from DFT rather than experimentally: there are in fact no stable Ni–Re or Ni–Ru crystals in nature [265, 266]. The PBESOL functional and OTF pseudopotentials generated by CASTEP were used. Target properties were the lattice constants of fcc ($L1_2$) Ni_3Re and Ni_3Ru and the difference in formation enthalpy between fcc Ni_3X and hcp Ni_6X_2 (the same crystal structure as Ti_3Al , space group $P6_3/\text{mmc}$ [194]), where X is Re or Ru. The second property was chosen due to its relation to the SFE, see section 2.2.2. The original and improved potentials are depicted in Fig. A.2. Note that the embedding function for Ru changes from having near constant value at high densities to instead having an embedding function similar in shape to that for Re, Mo (depicted), and the other elements. The target and achieved properties are given in table A.2. Parameters to fully specify the EAM potential used in this work given in table A.3.

Properties	Ni–Re			Ni–Ru		
	Target	Initial	Achieved	Target	Initial	Achieved
$E_{\text{hcp}} - 2E_{\text{fcc}}$ (eV)	-0.1070	-0.0291	1.0593	-0.9747	9.6462	0.0599
Lattice constant (Å)	3.5498	3.7076	3.6781	3.5753	3.6878	3.6896

Table A.2: Target values for Ni–X alloys from DFT, initial values from fitting pure material properties, and those achieved by optimising the gauge choice for each element.

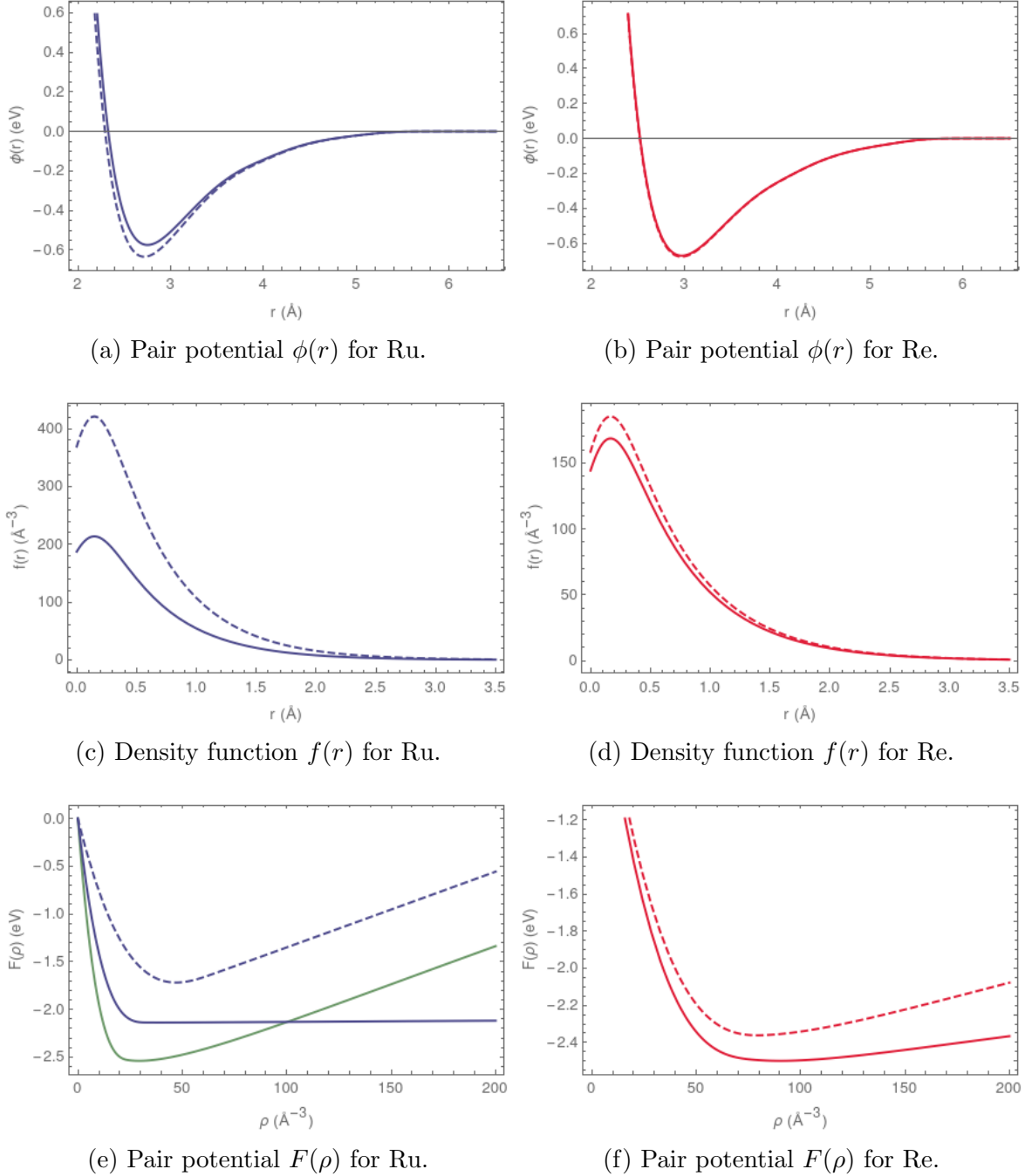


Figure A.2: Constituent parts of the EAM potential for Re and Ru. The solid line represents the original fit to pure element properties and the dashed line the improved fit to Ni-X properties. The green line in subFig. A.2e is $F(\rho)$ for Mo as fitted in the original paper [254].

	Ni	Cr	Co	Al	Ta	W	Ti	Mo	Re	Ru
r_e	2.488746	2.493879	2.505979	2.863924	2.74084	2.933872	2.7281	2.739521	2.650403	
f_e	2.007018	1.793835	1.975299	1.403115	3.086341	3.48734	1.8632	2.72371	2.601233	2.242417
ρ_e	27.562015	17.641302	27.206789	20.418205	33.787168	37.234847	25.565138	29.354065	90.324416	39.062186
ρ_s	27.562031	19.60545	27.206789	23.19574	33.787168	37.234847	25.565138	29.354065	90.324416	39.062186
α	8.383453	8.604593	8.679625	6.613165	8.489528	8.900114	8.775431	8.393531	7.75245	7.58578
β	4.471175	7.170494	4.629134	3.527021	4.527748	4.746728	4.68023	4.47655	4.70899	5.11809
A	0.429046	1.551848	0.421378	0.314873	0.611679	0.882435	0.373601	0.708787	1.99411	1.5815
B	0.633531	1.827556	0.640107	0.365551	1.032101	1.394592	0.570968	1.120373	2.54106	2.54106
κ	0.443599	0.18533	0.5	0.379846	0.176977	0.139209	0.5	0.13764	0.5	0.5
λ	0.820658	0.277995	1	0.759692	0.353954	0.278417	1	0.27528	1	1
F_{n0}	-2.693513	-2.022754	-2.541799	-2.807602	-5.103845	-4.946281	-3.203773	-3.692913	-2.49247	-2.13834
F_{n1}	-0.076445	0.039608	-0.219415	-0.301435	-0.405524	-0.148818	-0.198262	-0.178812	-0.078568	-0.002328
F_{n2}	0.241442	-0.183611	0.733381	1.258562	1.112997	0.365057	0.683779	0.38045	-0.26045	-0.007568
F_{n3}	-2.375626	-2.245972	-1.589003	-1.247604	-3.585325	-4.432406	-2.321732	-3.13365	-2.15345	-2.12845
F_0	-2.7	-2.02	-2.56	-2.83	-5.14	-4.96	-3.22	-3.71	-2.4901	-2.13854
F_1	0	0	0	0	0	0	0	0	0	0
F_2	0.26539	-0.056517	0.705845	0.622245	1.640098	0.661935	0.608587	0.875874	0.255734	-0.007788
F_3	-0.152856	0.439144	-0.68714	-2.488244	0.221375	0.348147	-0.75071	0.776222	0.232779	-0.005971
η	0.44547	0.456	0.694608	0.785902	0.848843	0.582714	0.558572	0.790879	-0.462922	-0.086771
F_e	-2.7	-2.020038	-2.559307	-2.824528	-5.141526	-4.961306	-3.219176	-3.712093	-2.49905	-2.13854
k	0	0	0	0	0	0	0	0	0.00173	0.01552
s	1	1	1	1	1	1	1	1	1.09911	1.97138

Table A.3: Parameters for the EAMs used in this work. Ni, Co, Al, Ta, W, Ti, Mo from [249, 255]. Cr from [257]. Re & Ru parameters from this work.

A.4 Supercells for alloy simulation

An alternative to generating SQS supercells is to generate a larger supercell with the elements pseudorandomly distributed in a solid solution. This completely neglects any clustering effects in the alloy, as well as segregation to boundary regions. There is some empirical evidence to suggest that clustering effects, particularly of Re, can play an important role in Ni superalloys [28, 29]. The method presented here—from here on referred to as the pseudorandom supercell method—should therefore be considered a low order approximation to a realistic solid solution alloy.

Without generating an SQS supercell, how can an appropriate lower bound be placed on the size of supercells generated using the pseudorandom method? The method proposed here is to estimate the required supercell size to make it likely that a certain atomic configuration will occur at least once, $P(\text{Configuration}) \approx 1$. There are many configurations that could be chosen but the simplest choice is a low order binary configuration, i.e. two atoms being first-nearest-neighbour (1NN). A physically motivated choice would be two atoms of the same species, of which there is a low fraction in the alloy but which are known to have an impact on the thermomechanical properties of the superalloy. The choice of binary configurations can be justified by considering the types of potentials in use: simple EAM potentials have no explicit inclusion of 3-body interactions (modified EAM potentials or MEAM potentials do).

Consider a finite periodic lattice, referred to as the supercell, with coordination number z , and with atoms of species type X being placed on it. This reflects the computational approach in which for each atom species X, a number of atoms of that species are placed on lattice sites pseudorandomly chosen from the remaining lattice sites which have not yet had atoms placed onto them. The integer number of atoms of species X within the supercell is $N_X \simeq x_X N$, where x_X is the atomic fraction of element X in the relevant alloy phase being simulated, and N is the total number of atoms in the supercell. The relationship is approximately true for large N and a fraction x_X with finite resolution. Species X can be considered the first atom type placed onto the lattice, such that all lattice sites are available for placement. As each atom is placed the probability that an atom of species X is placed next to another atom of species X is:

$$P(\text{X placed with 1NN X}) = z \frac{n_X}{N} , \quad (\text{A.11})$$

where n_X is the number of atoms of species X that have already been placed on the lattice. The probability that every atom of type X is placed without another first nearest

neighbour of type X is:

$$\begin{aligned} P(\text{Number of X-X 1NN is } 0) &= \prod_{n_X=0}^{N_X} \left(1 - z \frac{n_X}{N}\right) \\ &\approx 1 - \frac{z}{N} \sum_{n_X=0}^{N_X} n_X \end{aligned} \quad (\text{A.12})$$

$$\begin{aligned} &= 1 - \frac{z}{2N} N_X(N_X + 1) \\ &\approx 1 - \frac{1}{2} z N x_X^2 \quad . \end{aligned} \quad (\text{A.13})$$

Here Eq. A.12 has been found by taking $n_X \ll N$ and expanding to first order, which holds since $N_X/N = x_X \ll 1$ for the smallest species fraction. From Eq. A.13 the probability that there is at least one neighbouring pair of species X atoms is:

$$\begin{aligned} P(\text{Number of X-X 1NN} > 0) &= 1 - P(\text{Number of X-X 1NN is } 0) \\ &= \frac{1}{2} z N x_X^2 \quad . \end{aligned} \quad (\text{A.14})$$

It is desired that this probability should go to 1,

$$P(\text{Number of X-X 1NN} > 0) = \frac{1}{2} z N x_X^2 \simeq 1 \quad , \quad (\text{A.15})$$

which gives the lower bound for N :

$$N_{\min} = \frac{2}{z x_X^2} \quad . \quad (\text{A.16})$$

As an example for the γ phase where the smallest amount of any element in the phase is about 1 at. %, and $z = 12$ for an fcc lattice, this condition gives $N_{\min} = 1700$.

It might seem that Eq. A.15 cannot be correct since N can keep increasing to give a probability greater than one. Approaching the problem in a slightly different way shows that this is not the case. Again considering atoms of species X in the dilute limit $x_X \ll 1$, starting from a small value for N —and consequently N_X too—the expected number of X-X atom first nearest neighbours (1NN) should be roughly proportional to the total number of lattice sites neighbouring an X atom. This goes as $z N_X = z x_X N$. The probability of at least one pair of X atoms being first nearest neighbours should follow the same relationship. At some point this linear relationship will break down as the expected number of such neighbouring pairs becomes greater than 1. This is shown in Fig. A.3.

In the γ' phase atoms of different species segregate strongly onto different sublattices of the L1₂ lattice structure [3, 267]. The two sublattices are the Al (sublattice 1) and Ni (sublattice 2) sites in pure Ni₃Al: the Al atoms have $z_{12} = 12$ first nearest neighbour Ni

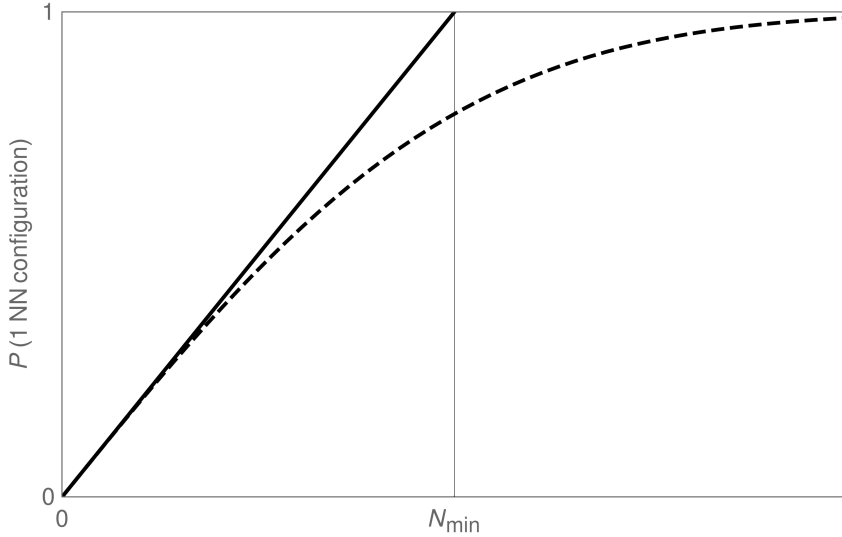


Figure A.3: Probability of at least one 1NN configuration of two X–X atoms in a size N supercell (dashed line) and estimation of N_{\min} given in the text (solid line).

atoms and no Al ones, whereas the Ni atoms have $z_{21} = 4$ first nearest neighbour Al atoms as well as 8 Ni ones. Considering Al has no nearest neighbours on its own sublattice and that cross-sublattice interactions must be physically important—most fundamentally for stability of the L1₂ structure—the configuration that should occur at least once in the γ' phase should be a first nearest neighbour between element X on sublattice 1 and Y on sublattice 2. As above this gives:

$$\begin{aligned}
 P(\text{Number of X–Y 1NN is } 0) &= \prod_{n_X=0}^{N_X} \left(1 - z_{12} \frac{N_Y}{N_2} \right) \\
 &= (1 - z_{12} x_{(Y,2)}^{N_X}) \\
 &\simeq 1 - z_{12} N_x x_{(Y,2)} \\
 \Rightarrow P(\text{Number of X–Y 1NN} > 0) &= z_{12} N_x x_{(Y,2)} \\
 &= z_{12} N_1 x_{(X,1)} x_{(Y,2)} , \tag{A.17}
 \end{aligned}$$

where $N_1 = N/4$ and $N_2 = 3N/4$ are the number of lattice sites on the 1st and 2nd sublattice, N_X and N_Y are the number of X atoms on the 1st sublattice and Y atoms on the 2nd sublattice, $x_{(X,1)}$ and $x_{(Y,2)}$ are the fraction of X atoms on the 1st sublattice and Y atoms on the 2nd sublattice respectively. The expression is symmetric for $X \leftrightarrow Y$ since $z_{12} N_1 = z_{21} N_2$. Setting Eq. A.17 $\simeq 1$ gives $N_{\min} = 4/z_{12} x_{(X,1)} x_{(Y,2)}$, or about double the total number of atoms for the fcc γ phase.

Bibliography

1. Taylor, P. L. & Conduit, G. Machine learning predictions of superalloy microstructure. *Computational Materials Science* **201**, 110916. ISSN: 0927-0256 (Jan. 2022).
2. Taylor, P. L. & Conduit, G. Machine learning superalloy microchemistry and creep strength from physical descriptors. *Computational Materials Science* **227**, 112265. ISSN: 0927-0256. <https://linkinghub.elsevier.com/retrieve/pii/S0927025623002598> (Aug. 2023).
3. Reed, R. C. *The superalloys fundamentals and applications* eng. ISBN: 1-107-16725-6 (Cambridge University Press, Cambridge, UK ; New York, 2006).
4. Sims, C. T. *A history of superalloy metallurgy for superalloy metallurgists* in *Superalloys 1984* (1984).
5. Bradley, A. & Taylor, A. An X-ray investigation of aluminium-rich iron-nickel-aluminium alloys after slow cooling. *J. Institute Metals* **66**, 53–65. <https://discovery.nationalarchives.gov.uk/details/r/e1d44ebd-dbb2-4325-b236-3a059770e2a0> (1940).
6. Graybill, B. *et al.* Additive manufacturing of nickel-based superalloys in *ASME 2018 13th International Manufacturing Science and Engineering Conference, MSEC 2018* **1** (American Society of Mechanical Engineers (ASME), Sept. 2018). ISBN: 9780791851357.
7. Kulkarni, A. Additive Manufacturing of Nickel Based Superalloy. <http://arxiv.org/abs/1805.11664> (May 2018).
8. Conduit, B. D. *et al.* Probabilistic neural network identification of an alloy for direct laser deposition. *Materials and Design* **168**, 107644. ISSN: 18734197 (Apr. 2019).
9. Caron, P. & Khan, T. *Evolution of Ni-based Superalloys for Single Crystal Gas Turbine Blade Applications* tech. rep. () .
10. Conduit, B. D., Jones, N. G., Stone, H. J. & Conduit, G. J. Design of a nickel-base superalloy using a neural network. *Materials and Design* **131**, 358–365. ISSN: 18734197 (Oct. 2017).
11. Pollock, T. M. & Van Der Ven, A. The evolving landscape for alloy design. *MRS Bulletin* **44**, 238–246. ISSN: 08837694 (Apr. 2019).
12. Rasmussen, C. E. & Williams, C. K. *Gaussian processes for machine learning* eng. ISBN: 0-262-26107-3 (MIT Press, Cambridge, Mass., 2006).
13. Duvenaud, D. K. *Automatic model construction with Gaussian processes* eng. PhD thesis (University of Cambridge, Cambridge, 2014).
14. Géron, A. *Hands-on machine learning with Scikit-Learn, Keras, and TensorFlow : concepts, tools, and techniques to build intelligent systems* Second edition. eng. ISBN: 978-1-4920-3264-9 (2019).

15. Wilson, A. G. & Adams, R. P. Gaussian Process Kernels for Pattern Discovery and Extrapolation (2013).
16. *Appreciate the Significance of Single-Crystal Turbine Blades* <https://www.foundrymag.com/molds-cores/media-gallery/21931762/appreciate-the-significance-of-singlecrystal-turbine-blades>.
17. Wang, W. Z. *et al.* Role of Re and Co on microstructures and γ' coarsening in single crystal superalloys. *Materials Science and Engineering A* **479**, 148–156. ISSN: 09215093 (Apr. 2008).
18. Collins, D. M. & Stone, H. J. A modelling approach to yield strength optimisation in a nickel-base superalloy. *International Journal of Plasticity* **54**, 96–112. ISSN: 0749-6419 (Mar. 2014).
19. Reed, R. C., Tao, T. & Warnken, N. Alloys-By-Design: Application to nickel-based single crystal superalloys. *Acta Materialia* **57**, 5898–5913. ISSN: 13596454 (Nov. 2009).
20. Reed, R. C., Mottura, A. & Crudden, D. J. *Alloys-By-Design: Towards Optimization of Compositions of Nickel-based Superalloys in Superalloys 2016* (2016), 15–23.
21. Zhang, L., Huang, Z., Pan, Y. & Jiang, L. Design of Re-free nickel-base single crystal superalloys using modelling and experimental validations. *Modelling and Simulation in Materials Science and Engineering* **27**. ISSN: 1361651X (May 2019).
22. Sung, P. K. & Poirier, D. R. Estimation of densities and coefficients of thermal expansion of solid Ni-base superalloys. *Materials Science and Engineering A* **245**, 135–141. ISSN: 09215093 (Apr. 1998).
23. Chauvet, E. *et al.* Hot cracking mechanism affecting a non-weldable Ni-based superalloy produced by selective electron Beam Melting. *Acta Materialia* **142**, 82–94. ISSN: 1359-6454 (Jan. 2018).
24. Boswell, J. H., Clark, D., Li, W. & Attallah, M. M. Cracking during thermal post-processing of laser powder bed fabricated CM247LC Ni-superalloy. *Materials & Design* **174**, 107793. ISSN: 0264-1275 (July 2019).
25. Tang, Y. T. *et al.* Alloys-by-design: Application to new superalloys for additive manufacturing. *Acta Materialia* **202**, 417–436. ISSN: 13596454 (Jan. 2021).
26. Sun, Z. *et al.* Reducing hot tearing by grain boundary segregation engineering in additive manufacturing: example of an $\text{Al}_x\text{CoCrFeNi}$ high-entropy alloy. *Acta Materialia* **204**, 116505. ISSN: 1359-6454 (Feb. 2021).
27. Clementl, N. *et al.* *Local Order and Mechanical Properties of the Gamma Matrix of Nickel-Base Superalloys* tech. rep. () .
28. Mottura, A., Wu, R. T., Finnis, M. W. & Reed, R. C. A critique of rhenium clustering in Ni-Re alloys using extended X-ray absorption spectroscopy. *Acta Materialia* **56**, 2669–2675. ISSN: 13596454 (June 2008).
29. Wu, X. *et al.* Unveiling the Re effect in Ni-based single crystal superalloys. *Nature Communications* **11**. ISSN: 20411723 (Dec. 2020).
30. Tin, S. *et al.* *Atomic partitioning of ruthenium in Ni-based superalloys* tech. rep. (Superalloys 2004: 10th International Symposium on Superalloys, 2004).
31. Bagot, P. A. *et al.* An Atom Probe Tomography study of site preference and partitioning in a nickel-based superalloy. *Acta Materialia* **125**, 156–165. ISSN: 1359-6454 (Feb. 2017).
32. Llewelyn, S. C. *et al.* The effect of Ni:Co ratio on the elemental phase partitioning in γ - γ' Ni-Co-Al-Ti-Cr alloys. *Acta Materialia* **131**, 296–304. ISSN: 1359-6454 (June 2017).

33. Durand-Charre, M. *The microstructure of superalloys* eng. ISBN: 9789056990978 (CRC Press, Boca Raton, Fl, USA, 1997).
34. Lahiri, A. Phase-field Modeling of Phase Transformations in Multicomponent Alloys: A Review. *Journal of the Indian Institute of Science* 2022 102:1 **102**, 39–57. ISSN: 0019-4964. <https://link.springer.com/article/10.1007/s41745-022-00288-y> (Mar. 2022).
35. Sethian, J. A. & Smereka, P. Level set methods for fluid interfaces. *Annu. Rev. Fluid Mech* **35**, 341–72. www.annualreviews.org (2003).
36. Bertin, N., Sills, R. B. & Cai, W. Frontiers in the Simulation of Dislocations. *Annual Review of Materials Research* **50**, 437–464. ISSN: 1531-7331 (July 2020).
37. Chatterjee, S., Li, Y. & Po, G. A discrete dislocation dynamics study of precipitate bypass mechanisms in nickel-based superalloys. *International Journal of Plasticity* **145**, 103062. ISSN: 0749-6419 (Oct. 2021).
38. Schuch, N. & Verstraete, F. Computational complexity of interacting electrons and fundamental limitations of density functional theory. *Nature Physics* **5**, 732–735. ISSN: 17452481. www.nature.com/naturephysics (Aug. 2009).
39. Van De Walle, A. *et al.* Efficient stochastic generation of special quasirandom structures. *Calphad: Computer Coupling of Phase Diagrams and Thermochemistry* **42**, 13–18. ISSN: 03645916 (Sept. 2013).
40. Kaufman, J. L. *et al.* Stacking fault energies of nondilute binary alloys using special quasirandom structures. *Physical Review B* **95**, 094112. ISSN: 24699969 (Mar. 2017).
41. Zhao, S., Stocks, G. M. & Zhang, Y. Stacking fault energies of face-centered cubic concentrated solid solution alloys. *Acta Materialia* **134**, 334–345. ISSN: 13596454 (Aug. 2017).
42. Chen, E. *et al.* Modeling antiphase boundary energies of Ni₃Al-based alloys using automated density functional theory and machine learning. *npj Computational Materials* 2022 8:1 **8**, 1–10. ISSN: 2057-3960. <https://www.nature.com/articles/s41524-022-00755-1> (Apr. 2022).
43. Van de Walle, A. & Ceder, G. Automating first-principles phase diagram calculations. *Journal of Phase Equilibria* **23**, 348–359. ISSN: 10549714 (2002).
44. Van de Walle, A. Multicomponent multisublattice alloys, nonconfigurational entropy and other additions to the Alloy Theoretic Automated Toolkit. *Calphad: Computer Coupling of Phase Diagrams and Thermochemistry* **33**, 266–278. ISSN: 03645916 (June 2009).
45. Woodward, C., van de Walle, A., Asta, M. & Trinkle, D. First-principles study of interfacial boundaries in Ni–Ni₃Al. *Acta Materialia* **75**, 60–70. ISSN: 1359-6454. <https://www.sciencedirect.com/science/article/pii/S1359645414003073?via%3Dhub#f0015> (Aug. 2014).
46. Sun, R. & Van De Walle, A. Automating impurity-enhanced antiphase boundary energy calculations from ab initio Monte Carlo. *Calphad: Computer Coupling of Phase Diagrams and Thermochemistry* **53**, 20–24. ISSN: 03645916 (June 2016).
47. Nguyen, M. C. *et al.* Cluster-Expansion Model for Complex Quinary Alloys: Application to Alnico Permanent Magnets. *Physical Review Applied* **8**. ISSN: 23317019 (Nov. 2017).
48. Wang, R. *et al.* Density functional theory study of the thermodynamic and elastic properties of Ni-based superalloys. *J. Phys.: Condens. Matter* **27**, 295401 (2015).
49. Crudden, D. J., Mottura, A., Warnken, N., Raeisnia, B. & Reed, R. C. Modelling of the influence of alloy composition on flow stress in high-strength nickel-based superalloys. *Acta Materialia* **75**, 356–370. ISSN: 13596454 (Aug. 2014).

50. Yu, X. X. & Wang, C. Y. The effects of alloying elements on generalized stacking fault energies, strength and ductility of γ' -Ni 3Al. *Materials Science and Engineering A* **539**, 38–41. ISSN: 09215093 (Mar. 2012).
51. Breidi, A., Allen, J. & Mottura, A. First-principles modeling of superlattice intrinsic stacking fault energies in Ni3Al based alloys. *Acta Materialia* **145**, 97–108. ISSN: 13596454 (Feb. 2018).
52. Gorbatov, O. I. *et al.* Effect of composition on antiphase boundary energy in Ni3Al based alloys: Ab initio calculations. *Physical Review B* **93**. ISSN: 24699969 (June 2016).
53. Zhang, X., Grabowski, B., Körmann, F., Freysoldt, C. & Neugebauer, J. Accurate electronic free energies of the 3 d, 4 d, and 5 d transition metals at high temperatures. *Physical Review B* **95**, 165126. ISSN: 24699969. <https://journals.aps.org/prb/abstract/10.1103/PhysRevB.95.165126> (Apr. 2017).
54. Dodaran, M. *et al.* Effect of alloying elements on the γ' antiphase boundary energy in Ni-base superalloys. *Intermetallics* **117**. ISSN: 09669795 (Feb. 2020).
55. Eurich, N. C. & Bristowe, P. D. Segregation of alloying elements to intrinsic and extrinsic stacking faults in γ' -Ni3Al via first principles calculations. *Scripta Materialia* **102**, 87–90. ISSN: 1359-6462 (June 2015).
56. Gubaev, K., Podryabinkin, E. V., Hart, G. L. & Shapeev, A. V. Accelerating high-throughput searches for new alloys with active learning of interatomic potentials. *Computational Materials Science* **156**. ISSN: 09270256 (2019).
57. Deringer, V. L., Caro, M. A. & Csányi, G. Machine Learning Interatomic Potentials as Emerging Tools for Materials Science. *Advanced Materials* **31**, 1902765. ISSN: 0935-9648. <https://onlinelibrary.wiley.com/doi/10.1002/adma.201902765> (Nov. 2019).
58. Zuo, Y. *et al.* Performance and Cost Assessment of Machine Learning Interatomic Potentials. *Journal of Physical Chemistry A* **124**, 731–745. ISSN: 15205215. <https://pubs.acs.org/doi/full/10.1021/acs.jpca.9b08723> (Jan. 2020).
59. Rosenbrock, C. W. *et al.* Machine-learned interatomic potentials for alloys and alloy phase diagrams. *npj Computational Materials* **7**, 1–9. ISSN: 20573960. <https://doi.org/10.1038/s41524-020-00477-2> (Dec. 2021).
60. Dusson, G. *et al.* Atomic cluster expansion: Completeness, efficiency and stability. *Journal of Computational Physics* **454**, 110946. ISSN: 0021-9991 (Apr. 2022).
61. Grabowski, B. *et al.* Ab initio vibrational free energies including anharmonicity for multicomponent alloys. *npj Computational Materials* **5**, 1–6. ISSN: 20573960. <https://doi.org/10.1038/s41524-019-0218-8> (Dec. 2019).
62. Balyakin, I. A., Yuryev, A. A., Gelchinski, B. R. & Rempel, A. A. Ab initio molecular dynamics and high-dimensional neural network potential study of VZrNbHfTa melt. *Journal of Physics: Condensed Matter* **32**, 214006. ISSN: 0953-8984. <https://iopscience.iop.org/article/10.1088/1361-648X/ab6f87%20https://iopscience.iop.org/article/10.1088/1361-648X/ab6f87/meta> (Feb. 2020).
63. Liu, X. *et al.* Monte Carlo simulation of order-disorder transition in refractory high entropy alloys: A data-driven approach *. *Computational Materials Science* **187**, 110135. <https://doi.org/10.1016/j.commatsci.2020.110135> (2021).
64. Pandey, A., Gigax, J. & Pokharel, R. Machine Learning Interatomic Potential for High-Throughput Screening of High-Entropy Alloys. *JOM* **74**, 2908–2920. ISSN: 15431851. <https://link.springer.com/article/10.1007/s11837-022-05306-z> (Aug. 2022).

65. Liu, X., Zhang, J. & Pei, Z. Machine learning for high-entropy alloys: Progress, challenges and opportunities. *Progress in Materials Science* **131**, 101018. ISSN: 0079-6425. <http://arxiv.org/abs/2209.03173> (Jan. 2023).
66. Li, M., Coakley, J., Isheim, D., Tian, G. & Shollock, B. Influence of the initial cooling rate from γ' supersolvus temperatures on microstructure and phase compositions in a nickel superalloy. *Journal of Alloys and Compounds* **732**, 765–776. ISSN: 09258388 (Jan. 2018).
67. Kattner, U. R. The CALPHAD method and its role in material and process development. *Tecnologia em Metalurgia Materiais e Mineração* **13**, 3–15. ISSN: 2176-1515. <http://tecnologiammm.com.br/doi/10.4322/2176-1523.1059> (Feb. 2016).
68. Hillert, M. Empirical methods of predicting and representing thermodynamic properties of ternary solution phases. *Calphad* **4**, 1–12. ISSN: 03645916 (Jan. 1980).
69. Chang, Y. A. *et al.* Phase diagram calculation: Past, present and future. *Progress in Materials Science* **49**, 313–345. ISSN: 00796425 (Jan. 2004).
70. Bajaj, S., Landa, A., Söderlind, P., Turchi, P. E. & Arróyave, R. The U-Ti system: Strengths and weaknesses of the CALPHAD method. *Journal of Nuclear Materials* **419**, 177–185. ISSN: 00223115 (Dec. 2011).
71. Andersson, J. O., Helander, T., Höglund, L., Shi, P. & Sundman, B. Thermo-Calc & DICTRA, computational tools for materials science. *Calphad: Computer Coupling of Phase Diagrams and Thermochemistry* **26**, 273–312. ISSN: 03645916 (June 2002).
72. Sundman, B., Kattner, U. R., Palumbo, M. & Fries, S. G. *OpenCalphad - a free thermodynamic software* Dec. 2015. <https://link.springer.com/article/10.1186/s40192-014-0029-1>.
73. Bäker, M. Calculating phase diagrams with ATAT. <http://arxiv.org/abs/1907.10151> (July 2019).
74. Attari, V. *et al.* Uncertainty propagation in a multiscale CALPHAD-reinforced elasto-chemical phase-field model. *Acta Materialia* **183**, 452–470. ISSN: 13596454 (Jan. 2020).
75. Mermin, N. D. The topological theory of defects in ordered media. *Reviews of Modern Physics* **51**, 591. ISSN: 00346861. <https://journals.aps.org/rmp/abstract/10.1103/RevModPhys.51.591> (July 1979).
76. Hosford, W. F. in *Mechanical Behavior of Materials* 2nd ed., 259–274 (Cambridge University Press, 2009).
77. Anderson, P. M. (M., Hirth, J. P. & Lothe, J. *Theory of dislocations* Third edition. eng. ISBN: 0521864364 (Cambridge University Press, 2017).
78. Hosford, W. F. in *Mechanical Behavior of Materials* 2nd ed., 137–154 (Cambridge University Press, 2009).
79. Zhang, L. *et al.* Molecular dynamics simulation on generalized stacking fault energies of FCC metals under preloading stress. *Chinese Physics B* **24**, 088106. ISSN: 1674-1056. <http://stacks.iop.org/1674-1056/24/i=8/a=088106?key=crossref.4f45dcff46e5fdfc4bc8ad35144b6932> (Aug. 2015).
80. Zimmerman, J. A., Gao, H. & Abraham, F. F. Generalized stacking fault energies for embedded atom FCC metals. *Modelling and Simulation in Materials Science and Engineering* **8**, 103–115. ISSN: 0965-0393. <http://stacks.iop.org/0965-0393/8/i=2/a=302?key=crossref.8229b2c385fc754a8e5d1a43cfdd3307> (Mar. 2000).
81. Hosford, W. F. in *Mechanical Behavior of Materials* 2nd ed., 155–165 (Cambridge University Press, 2009).

82. Veyssi  re, P. & Saada, G. Chapter 53 Microscopy and plasticity of the L12 γ phase. *Dislocations in Solids* **10**, 253–441. ISSN: 1572-4859 (Jan. 1996).
83. Caron, P., Ramusat, C. & Diologent, F. *Influence of the γ' fraction on the γ/γ' topological inversion during high temperature creep of single crystal superalloys* tech. rep. (Superalloys 2008: 11th International Symposium on Superalloys, 2008).
84. Ralph, B., Hill, S. A., Southon, M. J., Thomas, M. P. & Waugh, A. R. The investigation of engineering materials using atom-probe techniques. *Ultramicroscopy* **8**, 361–375. ISSN: 03043991 (Jan. 1982).
85. Yoon, K. E., Noebe, R. D. & Seidman, D. N. Effects of rhenium addition on the temporal evolution of the nanostructure and chemistry of a model Ni-Cr-Al superalloy. I: Experimental observations. *Acta Materialia* **55**, 1145–1157. ISSN: 13596454 (Feb. 2007).
86. Schmidt, R. & Feller-Kniepmeier, M. Effect of heat treatments on phase chemistry of the Nickel-Base superalloy SRR 99. *Metallurgical Transactions A* **23**, 745–757. ISSN: 03602133 (Mar. 1992).
87. Miller, M. K., Jayaram, R., Lin, L. S. & Cetel, A. D. APFIM characterization of single-crystal PWA 1480 nickel-base superalloy. *Applied Surface Science* **76-77**, 172–176. ISSN: 01694332 (Mar. 1994).
88. Khan, T. & Caron, P. Effect of processing conditions and heat treatments on mechanical properties of single-crystal superalloy CMSX-2. *Materials Science and Technology (United Kingdom)* **2**, 486–492. ISSN: 17432847 (1986).
89. Khan, T., Caron, P. & Duret, C. *The development and characterization of a high performance experimental single crystal superalloy* in *Superalloys 1984* (1984), 145–155.
90. Blavette, D. & Bostel, A. Phase composition and long range order in γ' phase of a nickel base single crystal superalloy CMSX2: An atom probe study. *Acta Metallurgica* **32**, 811–816. ISSN: 00016160 (1984).
91. Cui, C. Y., Tian, C. G., Zhou, Y. Z., Jin, T. & Sun, X. F. *Dynamic strain aging in Ni base alloys with different stacking fault energy* tech. rep. (Superalloys 2012: 12th International Symposium on Superalloys, 2012).
92. Wang, X. G., Liu, J. L., Jin, T. & Sun, X. F. The effects of ruthenium additions on tensile deformation mechanisms of single crystal superalloys at different temperatures. *Materials and Design* **63**, 286–293. ISSN: 18734197 (Nov. 2014).
93. Tian, S., Zeng, Z., Fushun, L., Zhang, C. & Liu, C. Creep behavior of a 4.5%-Re single crystal nickel-based superalloy at intermediate temperatures. *Materials Science and Engineering A* **543**, 104–109. ISSN: 09215093 (May 2012).
94. Tian, S. et al. Influence of Temperature on Stacking Fault Energy and Creep Mechanism of a Single Crystal Nickel-based Superalloy. *Journal of Materials Science and Technology* **32**, 790–798. ISSN: 10050302 (Aug. 2016).
95. Blavette, D., Duval, P., Letellier, L. & Guttmann, M. Atomic-scale APFIM and TEM investigation of grain boundary microchemistry in astroloy nickel base superalloys. *Acta Materialia* **44**, 4995–5005. ISSN: 13596454 (Dec. 1996).
96. Nathal, M. V. & Ebert, L. J. Elevated temperature creep-rupture behavior of the single crystal nickel-base superalloy NASAIR 100. *Metallurgical Transactions A* **16**, 427–439. ISSN: 03602133 (Mar. 1985).
97. D  camps, B., Condat, M., Caron, P. & Khan, T. Dissociated matrix dislocations in a σ/σ' Ni-based single crystal superalloy. *Scripta Metallurgica*. ISSN: 00369748 (1984).

98. Pettinari, F. *et al.* Stacking fault energy in short-range ordered γ -phases of Ni-based superalloys. *Materials Science and Engineering A*. ISSN: 09215093 (2002).
99. Ofori, A. P., Humphreys, C. J., Tin, S. & Jones, C. N. *A TEM study of the effect of platinum group metals in advanced single crystal nickel-base superalloys* tech. rep. (Superalloys 2004: 10th International Symposium on Superalloys, 2004).
100. Kawagishi, K. *et al.* *Development of an Oxidation-Resistant High-Strength Sixth-Generation Single-Crystal Superalloy TMS-238* tech. rep. (Superalloys 2012: 12th International Symposium on Superalloys, 2012).
101. Semiatin, S. L. *et al.* High-Temperature Static Coarsening of Gamma-Prime Precipitates in NiAlCr-X Single Crystals. *Metallurgical and Materials Transactions A* **50**, 2289–2301. <https://doi.org/10.1007/s11661-018-05104-w> (2019).
102. Blavette, D., Cadel, E. & Deconihout, B. Role of the atom probe in the study of nickel-based superalloys. *Materials Characterization* **44**, 133–157. ISSN: 10445803 (Jan. 2000).
103. Miller, M. K. *Contributions of atom probe tomography to the understanding of nickel-based superalloys* in *Micron* **32** (Pergamon, Jan. 2001), 757–764.
104. Fuchs, G. E. & Boutwell, B. A. Modeling of the partitioning and phase transformation temperatures of an as-cast third generation single crystal Ni-base superalloy. *Materials Science and Engineering A* **333**, 72–79. ISSN: 09215093 (Aug. 2002).
105. Köster, E. H., Thölén, A. R. & Howie, A. Stacking fault energies of Ni–Co–Cr alloys. *Philosophical Magazine* **10**, 1093–1095. ISSN: 00318086 (1964).
106. Ma, S., Carroll, L. & Pollock, T. M. Development of γ phase stacking faults during high temperature creep of Ru-containing single crystal superalloys. *Acta Materialia* **55**, 5802–5812. ISSN: 13596454 (Oct. 2007).
107. Hart, G. L., Mueller, T., Toher, C. & Curtarolo, S. Machine learning for alloys. *Nature Reviews Materials* 2021 **6**:8 **6**, 730–755. ISSN: 2058-8437. <https://www.nature.com/articles/s41578-021-00340-w> (July 2021).
108. Venkatesh, V. & Rack, H. J. Neural network approach to elevated temperature creep-fatigue life prediction. *International Journal of Fatigue* **21**, 225–234. ISSN: 01421123 (Mar. 1999).
109. Yoo, Y. S., Jo, C. Y. & Jones, C. N. Compositional prediction of creep rupture life of single crystal Ni base superalloy by Bayesian neural network. *Materials Science and Engineering A* **336**, 22–29. ISSN: 09215093 (Oct. 2002).
110. Harada, H., Ohno, K., Yamagata, T., Yokokawa, T. & Yamazaki, M. *Phase calculation and its use in alloy design program for nickel-base superalloys* tech. rep. (Superalloys 1988, 1988).
111. Harada, H. & Murakami, H. in *Computational Materials Design* (ed Saito, T.) 39–70 (Springer Berlin Heidelberg, Berlin, Heidelberg, 1999). ISBN: 978-3-662-03923-6. https://doi.org/10.1007/978-3-662-03923-6_2.
112. Enomoto, M., Harada, H. & Yamazaki, M. Calculation of γ'/γ equilibrium phase compositions in nickel-base superalloys by cluster variation method. *Calphad* **15**, 143–158. ISSN: 03645916 (Apr. 1991).
113. Saito, Y. The Monte Carlo simulation of microstructural evolution in metals. *Materials Science and Engineering A* **223**, 114–124. ISSN: 09215093 (Feb. 1997).
114. Sato, A. *et al.* *A 5th generation SC superalloy with balanced high temperature properties and processability* tech. rep. (Superalloys 2008: 11th International Symposium on Superalloys, 2008).

115. Titsias, M. K. *Variational Learning of Inducing Variables in Sparse Gaussian Processes* Apr. 2009. <https://proceedings.mlr.press/v5/titsias09a.html>.
116. Oviedo, F., Ferres, J. L., Buonassisi, T. & Butler, K. T. Interpretable and Explainable Machine Learning for Materials Science and Chemistry. *Accounts of Materials Research* **3**, 597–607. ISSN: 26436728. <https://pubs.acs.org/doi/full/10.1021/accountsmr.1c00244> (June 2022).
117. Gardner, J. R., Pleiss, G., Bindel, D., Weinberger, K. Q. & Wilson, A. G. GPyTorch: Blackbox Matrix-Matrix Gaussian Process Inference with GPU Acceleration. *Advances in Neural Information Processing Systems* **2018-December**, 7576–7586. ISSN: 10495258. <https://arxiv.org/abs/1809.11165v6> (Sept. 2018).
118. Papadopoulos, G., Edwards, P. J. & Murray, A. F. Confidence estimation methods for neural networks: A practical comparison. *IEEE Transactions on Neural Networks* **12**, 1278–1287. ISSN: 10459227 (Nov. 2001).
119. Collier, J. P. Effects of replacing the refractory elements W, Nb and Ta with Mo in nickel-bases superalloys on microstructural, microchemistry, and mechanical properties. *Metallurgical transactions. A, Physical metallurgy and materials science* **17 A**, 651–661. ISSN: 03602133. <https://link.springer.com/article/10.1007/BF02643984> (1986).
120. Cui, C. Y., Gu, Y. F., Ping, D. H. & Harada, H. Phase constituents in Ni–Al–Co–Ti quaternary alloys. *Intermetallics* **16**, 910–916. ISSN: 0966-9795 (July 2008).
121. Decamps, B. & Condat, M. (a/2)⟨110⟩ dislocations at the γ/γ' interface in a Ni-based superalloy. *physica status solidi (a)* **109**, K15–K18. ISSN: 1521396X. <http://doi.wiley.com/10.1002/pssa.2211090144> (Sept. 1988).
122. Décamps, B., Morton, A. J. & Condat, M. Philosophical Magazine A On the mechanism of shear of γ' precipitates by single (a/2)⟨110⟩ dissociated matrix dislocations in Ni-based superalloys. ISSN: 1460-6992. <https://www.tandfonline.com/action/journalInformation?journalCode=tphm20>.
123. Delargy, K. M. & Smith, G. D. Phase composition and phase stability of high-chromium nickel-based superalloy, IN939. *Metallurgical transactions. A, Physical metallurgy and materials science* **14 A**, 1771–1783 (1983).
124. Diolgent, F. & Caron, P. On the creep behavior at 1033 K of new generation single-crystal superalloys. *Materials Science and Engineering A* **385**, 245–257. ISSN: 09215093 (Nov. 2004).
125. Dreshfield, R. L. *Estimation of gamma phase composition in nickel-base superalloys /based on geometric analysis of a four-component phase diagram* tech. rep. (NASA, Lewis Research Center, Cleveland, OH, USA, 1970). <https://ntrs.nasa.gov/search.jsp?R=19700016436>.
126. Basak, A. & Das, S. Microstructure of nickel-base superalloy MAR-M247 additively manufactured through scanning laser epitaxy (SLE). *Journal of Alloys and Compounds* **705**, 806–816. ISSN: 09258388 (May 2017).
127. Duval, S., Chambreland, S., Caron, P. & Blavette, D. Phase composition and chemical order in the single crystal nickel base superalloy MC2. *Acta Metallurgica Et Materialia*. ISSN: 09567151 (1994).
128. Fahrmann, M. *et al.* Determination of matrix and precipitate elastic constants in ($\gamma\text{-}\gamma'$) Ni-base model alloys, and their relevance to rafting. *Materials Science and Engineering A* **260**, 212–221. ISSN: 09215093 (Feb. 1999).
129. Glas, R., Jouiad, M., Caron, P., Clement, N. & Kirchner, H. O. Order and mechanical properties of the γ matrix of superalloys. *Acta Materialia*. ISSN: 13596454 (1996).

130. Goodfellow, A. J. *et al.* Gamma Prime Precipitate Evolution During Aging of a Model Nickel-Based Superalloy. *Metallurgical and Materials Transactions A: Physical Metallurgy and Materials Science* **49**, 718–728. ISSN: 10735623. <https://link.springer.com/article/10.1007/s11661-017-4336-y> (Mar. 2018).
131. Harada, H., Ishida, A., Murakami, Y., Bhadeshia, H. K. & Yamazaki, M. Atom-probe microanalysis of a nickel-base single crystal superalloy. *Applied Surface Science* **67**, 299–304. ISSN: 01694332 (Apr. 1993).
132. Hobbs, R. A., Zhang, L., Rae, C. M. & Tin, S. The effect of ruthenium on the intermediate to high temperature creep response of high refractory content single crystal nickel-base superalloys. *Materials Science and Engineering A* **489**, 65–76. ISSN: 09215093 (Aug. 2008).
133. Hopgood, A. A. & Martin, J. W. *The Creep Behaviour of a Nickel-based Single-crystal Superalloy* tech. rep. (1986), 27–36.
134. Horst, O. M. *et al.* Exploring the fundamentals of Ni-based superalloy single crystal (SX) alloy design: Chemical composition vs. microstructure. *Materials & Design* **195**, 108976. ISSN: 0264-1275 (Oct. 2020).
135. Blavette, D., Caron, P. & Khan, T. An atom probe investigation of the role of rhenium additions in improving creep resistance of Ni-base superalloys. *Scripta Metallurgica* **20**, 1395–1400. ISSN: 00369748 (Oct. 1986).
136. Huang, H. E. & Koo, C. H. Characteristics and Mechanical Properties of Polycrystalline CM 247 LC Superalloy Casting. *MATERIALS TRANSACTIONS* **45**, 562–568. ISSN: 1345-9678 (2004).
137. Jalilvand, V., Omidvar, H., Rahimipour, M. R. & Shakeri, H. R. Influence of bonding variables on transient liquid phase bonding behavior of nickel based superalloy IN-738LC. *Materials and Design* **52**, 36–46. ISSN: 18734197 (Dec. 2013).
138. Janowski, G. M., Heckel, R. W. & Pletka, B. J. The Effects of Tantalum on the Microstructure of Two Polycrystalline Nickel-Base Superalloys B-1900 + Hf and MAR-M247. *Metallurgical Transactions A* **17A**, 1891–1905 (1986).
139. Jovanović, M. T., Miškovic, Z. & Lukić, B. Microstructure and stress-rupture life of polycrystal, directionally solidified, and single crystal castings of nickel-based IN 939 superalloy. *Materials Characterization* **40**, 261–268. ISSN: 10445803 (1998).
140. Kitajima, Y., Hayashi, S. & Narita, T. Phase Equilibria of the Nickel-Aluminium-Chromium System at 1150°C. *Materials Science Forum* **522-523**, 103–110. ISSN: 1662-9752. <https://www.scientific.net/MSF.522-523.103> (Aug. 2006).
141. Krieger, O. H. & Baris, J. M. The chemical partitioning of elements in gamma prime separated from precipitation-hardened, high-temperature nickel-base alloys. *ASM (Amer. Soc. Metals), Trans. Quart.*, 195–200. <https://www.osti.gov/biblio/4789116-chemical-partitioning-elements-gamma-prime-separated-from-precipitation-hardened-high-temperature-nickel-base-alloys> (1969).
142. Lapington, M. T., Crudden, D. J., Reed, R. C., Moody, M. P. & Bagot, P. A. Characterization of Phase Chemistry and Partitioning in a Family of High-Strength Nickel-Based Superalloys. *Metallurgical and Materials Transactions A: Physical Metallurgy and Materials Science* **49**, 2302–2310. ISSN: 10735623. <https://doi.org/10.1007/s11661-018-4558-7> (June 2018).
143. Liu, Y. *et al.* Microstructure evolution and mechanical performance of nickel based superalloy C1023 at elevated temperatures. *Materials Characterization* **138**, 174–185. ISSN: 1044-5803 (Apr. 2018).

144. Liu, F. *et al.* High-throughput determination of interdiffusivity matrices in Ni-Al-Ti-Cr-Co-Mo-Ta-W multicomponent superalloys and their application in optimization of creep resistance. *Materials Today Communications* **24**, 101018. ISSN: 23524928 (Sept. 2020).
145. Long, H., Mao, S., Liu, Y., Zhang, Z. & Han, X. *Microstructural and compositional design of Ni-based single crystalline superalloys — A review* Apr. 2018.
146. Loomis, W. T., Freeman, J. W. & Sponseller, D. L. The influence of molybdenum on the γ' /phase in experimental nickel-base superalloys. *Metallurgical and Materials Transactions B* **3**, 989–1000. ISSN: 1073-5615 (Apr. 1972).
147. Mihalisin, J. R. & Pasquine, D. L. *Phase Transformations in Nickel-base Superalloys* in *International Symposium on Structural Stability in Superalloys* (Seven Springs, PA, 1968), 134–170.
148. Morrow, H., Sponseller, D. L. & Semchyshen, M. The effects of molybdenum and aluminum on the thermal expansion coefficients of nickel-base alloys. *Metallurgical Transactions A* **6**, 477–485. ISSN: 03602133 (Feb. 1975).
149. Mostafaei, M., Abbasi, S. M. & Mostafaei, M. A. Improvement of γ' coarsening model in high γ' volume fraction Ni-base superalloys containing different Ta/W ratio. *Journal of Alloys and Compounds* **885**, 160938. ISSN: 0925-8388 (Dec. 2021).
150. Brož, P., Svoboda, M., Buršík, J., Kroupa, A. & Havráneková, J. Theoretical and experimental study of the influence of Cr on the $\gamma + \gamma'$ phase field boundary in the Ni-Al-Cr system. *Materials Science and Engineering A* **325**, 59–65. ISSN: 09215093 (Feb. 2002).
151. Park, J. U. *et al.* Alloy design of Ni-based superalloy with high γ' volume fraction suitable for additive manufacturing and its deformation behavior. *Additive Manufacturing* **52**, 102680. ISSN: 2214-8604 (Apr. 2022).
152. Parsa, A. B. *et al.* Advanced Scale Bridging Microstructure Analysis of Single Crystal Ni-Base Superalloys. *Advanced Engineering Materials* **17**, 216–230. ISSN: 14381656. <http://doi.wiley.com/10.1002/adem.201400136> (Feb. 2015).
153. Rakoczy, L. *et al.* Characterization of γ' Precipitates in Cast Ni-Based Superalloy and Their Behaviour at High-Homologous Temperatures Studied by TEM and in Situ XRD. *Materials 2020, Vol. 13, Page 2397* **13**, 2397. ISSN: 1996-1944. <https://www.mdpi.com/1996-1944/13/10/2397/htm%20https://www.mdpi.com/1996-1944/13/10/2397> (May 2020).
154. Reed, R. C., Yeh, A. C., Tin, S., Babu, S. S. & Miller, M. K. Identification of the partitioning characteristics of ruthenium in single crystal superalloys using atom probe tomography. *Scripta Materialia* **51**, 327–331. ISSN: 13596462 (Aug. 2004).
155. Royer, A., Bastie, P. & Veron, M. In situ determination of γ' phase volume fraction and of relations between lattice parameters and precipitate morphology in ni-based single crystal superalloy. *Acta Materialia* **46**, 5357–5368. ISSN: 13596454 (Sept. 1998).
156. Caron, P. *High γ' solvus new generation nickel-based superalloys for single crystal turbine blade applications* in *Superalloys 2000* (2000), 737–746.
157. Safari, J. & Nategh, S. On the heat treatment of Rene-80 nickel-base superalloy. *Journal of Materials Processing Technology* **176**, 240–250. ISSN: 0924-0136 (June 2006).
158. Segersäll, M. *et al.* Thermal-mechanical fatigue behaviour of a new single crystal superalloy: Effects of Si and Re alloying. *Acta Materialia* **95**, 456–467. ISSN: 13596454 (Aug. 2015).
159. Siebörger, D., Knake, H. & Glatzel, U. Temperature dependence of the elastic moduli of the nickel-base superalloy CMSX-4 and its isolated phases. *Materials Science and Engineering A* **298**, 26–33. ISSN: 09215093 (Jan. 2001).

160. Sudbrack, C. K., Yoon, K. E., Noebe, R. D. & Seidman, D. N. Temporal evolution of the nanostructure and phase compositions in a model Ni–Al–Cr alloy. *Acta Materialia* **54**, 3199–3210. ISSN: 1359-6454 (July 2006).
161. Sulzer, S. *et al.* The Effects of Chemistry Variations in New Nickel-Based Superalloys for Industrial Gas Turbine Applications. *Metallurgical and Materials Transactions A: Physical Metallurgy and Materials Science* **51**, 4902–4921. ISSN: 10735623. <https://doi.org/10.1007/s11661-020-05845-7> (Sept. 2020).
162. Tian, S., Qian, B., Su, Y., Yu, H. & Yu, X. Influence of Stacking Fault Energy on Creep Mechanism of a Single Crystal Nickel-Based Superalloy Containing Re. *Materials Science Forum* **706-709**, 2474–2479. ISSN: 1662-9752. <https://www.scientific.net/MSF.706-709.2474> (2012).
163. Tsuno, N., Kakehi, K., Rae, C. M. & Hashizume, R. Effect of ruthenium on creep strength of Ni-Base single-crystal superalloys at 750 °C and 750 MPa. *Metallurgical and Materials Transactions A: Physical Metallurgy and Materials Science* **40**, 269–272. ISSN: 10735623 (Dec. 2009).
164. Wanderka, N. & Glatzel, U. Chemical composition measurements of a nickel-base superalloy by atom probe field ion microscopy. *Materials Science and Engineering: A* **203**, 69–74. ISSN: 0921-5093 (Nov. 1995).
165. Wlodek, S. T., Kelly, M. & Alden, D. A. *The Structure of Rene 88 DT* tech. rep. (Superalloys 1996, 1996).
166. Yuan, Y. *et al.* Influence of Co content on stacking fault energy in Ni-Co base disk superalloys. *Journal of Materials Research* **26**, 2833–2837. ISSN: 08842914 (Nov. 2011).
167. Zhang, Y., Wanderka, N., Schumacher, G., Schneider, R. & Neumann, W. Phase chemistry of the superalloy SC16 after creep deformation. *Acta Materialia* **48**, 2787–2793. ISSN: 1359-6454 (June 2000).
168. Zhang, J., Li, J., Jin, T., Sun, X. & Hu, Z. Effect of Mo concentration on creep properties of a single crystal nickel-base superalloy. *Materials Science and Engineering A* **527**, 3051–3056. ISSN: 09215093 (May 2010).
169. Chen, J. & Xue, L. Process-induced microstructural characteristics of laser consolidated IN-738 superalloy. *Materials Science and Engineering: A* **527**, 7318–7328. ISSN: 0921-5093 (Oct. 2010).
170. Clement, N. & Coulomb, P. Energies de défaut d'empilement et mécanismes de déformation dans les alliages nickel-chrome. *Philosophical Magazine* **30**, 663–672. ISSN: 00318086 (1974).
171. Rohatgi, A. *Webplotdigitizer: Version 4.6* 2022. <https://automeris.io/WebPlotDigitizer>.
172. Lee, K., Ayyasamy, M. V., Delsa, P., Hartnett, T. Q. & Balachandran, P. V. Phase classification of multi-principal element alloys via interpretable machine learning. *npj Computational Materials 2022 8:1* **8**, 1–12. ISSN: 2057-3960. <https://www.nature.com/articles/s41524-022-00704-y> (Feb. 2022).
173. Pröbstle, M. *et al.* Improved creep strength of nickel-base superalloys by optimized γ/γ' partitioning behavior of solid solution strengthening elements. *Materials Science and Engineering A* **676**. ISSN: 09215093 (2016).
174. Verpoort, P. C., MacDonald, P. & Conduit, G. J. Materials data validation and imputation with an artificial neural network. *Computational Materials Science* **147**, 176–185. ISSN: 0927-0256 (May 2018).

175. Liu, Y. *et al.* Predicting creep rupture life of Ni-based single crystal superalloys using divide-and-conquer approach based machine learning. *Acta Materialia* **195**, 454–467. ISSN: 13596454 (Aug. 2020).
176. Tancret, F., Bhadeshia, H. K. & MacKay, D. J. Design of a creep resistant nickel base superalloy for power plant applications: Part 1 - Mechanical properties modelling. *Materials Science and Technology* **19**, 283–290. ISSN: 02670836. <https://www.tandfonline.com/action/journalInformation?journalCode=ymst20> (Mar. 2003).
177. Menou, E., Ramstein, G., Bertrand, E. & Tancret, F. Multi-objective constrained design of nickel-base superalloys using data mining- and thermodynamics-driven genetic algorithms. *Modelling and Simulation in Materials Science and Engineering* **24**. ISSN: 1361651X (Apr. 2016).
178. Menou, E., Rame, J., Desgranges, C., Ramstein, G. & Tancret, F. Computational design of a single crystal nickel-based superalloy with improved specific creep endurance at high temperature. *Computational Materials Science* **170**, 109194. ISSN: 09270256 (Dec. 2019).
179. Zhang, Y. & Xu, X. Lattice Misfit Predictions via the Gaussian Process Regression for Ni-Based Single Crystal Superalloys. *Metals and Materials International*, 1–19. ISSN: 20054149. <https://doi.org/10.1007/s12540-020-00883-7> (Oct. 2020).
180. Yabansu, Y. C., Iskakov, A., Kapustina, A., Rajagopalan, S. & Kalidindi, S. R. Application of Gaussian process regression models for capturing the evolution of microstructure statistics in aging of nickel-based superalloys. *Acta Materialia* **178**, 45–58. ISSN: 13596454 (Oct. 2019).
181. Yuan, Y. *et al.* Creep deformation of a sixth generation Ni-base single crystal superalloy at 800°C. *Materials Science and Engineering A* **608**, 95–100. ISSN: 09215093 (July 2014).
182. Kanagawa, M., Hennig, P., Sejdinovic, D. & Sriperumbudur, B. K. Gaussian Processes and Kernel Methods: A Review on Connections and Equivalences. *arXiv*. <http://arxiv.org/abs/1807.02582> (July 2018).
183. Pedregosa, F. *et al.* Scikit-learn: Machine learning in Python. *Journal of Machine Learning Research* **12**, 2825–2830. ISSN: 15324435. <http://scikit-learn.org>. (Oct. 2011).
184. Tamura, R. *et al.* Machine learning-driven optimization in powder manufacturing of Ni-Co based superalloy. *Materials and Design* **198**, 109290. ISSN: 18734197 (Jan. 2021).
185. Snelson, E. & Ghahramani, Z. Variable noise and dimensionality reduction for sparse Gaussian processes. *Proceedings of the 22nd Conference on Uncertainty in Artificial Intelligence, UAI 2006*, 461–468. <http://arxiv.org/abs/1206.6873> (June 2012).
186. Pollock, T. M. & Tin, S. *Nickel-based superalloys for advanced turbine engines: Chemistry, microstructure, and properties* May 2006. <http://arc.aiaa.org>.
187. Mohammed, R. O. & Cawley, G. C. *Over-fitting in model selection with Gaussian process regression* in *Lecture Notes in Computer Science (including subseries Lecture Notes in Artificial Intelligence and Lecture Notes in Bioinformatics)* **10358 LNAI** (Springer Verlag, 2017), 192–205. ISBN: 9783319624150. <http://theoval.cmp.uea.ac.uk/>.
188. Martin, E. J., Polyakov, V. R., Tian, L. & Perez, R. C. Profile-QSAR 2.0: Kinase Virtual Screening Accuracy Comparable to Four-Concentration IC50s for Realistically Novel Compounds. *Journal of Chemical Information and Modeling* **57**, 2077–2088. ISSN: 15205142 (Aug. 2017).
189. Irwin, B. W., Levell, J. R., Whitehead, T. M., Segall, M. D. & Conduit, G. J. Practical Applications of Deep Learning to Impute Heterogeneous Drug Discovery Data. *Journal of Chemical Information and Modeling* **60**, 2848–2857. ISSN: 15205142. <https://pubs.acs.org/doi/abs/10.1021/acs.jcim.0c00443> (June 2020).

190. Collins, D. M. *et al.* Grain growth behaviour during near- γ' solvus thermal exposures in a polycrystalline nickel-base superalloy. *Acta Materialia* **61**, 3378–3391. ISSN: 1359-6454 (May 2013).
191. Hume-Rothery, W. & Powell, H. M. On the Theory of Super-Lattice Structures in Alloys. *Zeitschrift für Kristallographie - Crystalline Materials* **91**, 23–47. ISSN: 2196-7105. <https://www.degruyter.com/document/doi/10.1524/zkri.1935.91.1.23/html> (Nov. 1935).
192. Hume-Rothery, W. *Atomic theory for students of metallurgy*. [3d rev. reprint]. eng (Institute of Metals, London, 1955).
193. Pettifor, D. G. A chemical scale for crystal-structure maps. *Solid State Communications* **51**, 31–34. ISSN: 0038-1098 (July 1984).
194. Glawe, H., Sanna, A., Gross, E. K. & Marques, M. A. The optimal one dimensional periodic table: a modified Pettifor chemical scale from data mining. *New Journal of Physics* **18**, 093011. ISSN: 1367-2630. [https://iopscience.iop.org/article/10.1088/1367-2630/18/9/093011/meta](https://iopscience.iop.org/article/10.1088/1367-2630/18/9/093011%20https://iopscience.iop.org/article/10.1088/1367-2630/18/9/093011/meta) (Sept. 2016).
195. Qin, Z. *et al.* Phase prediction of Ni-base superalloys via high-throughput experiments and machine learning. *Materials Research Letters* **9**, 32–40. ISSN: 21663831. <https://www.tandfonline.com/doi/abs/10.1080/21663831.2020.1815093> (Jan. 2021).
196. Asensio Dominguez, L., Goodall, R. & Todd, I. Prediction and validation of quaternary high entropy alloys using statistical approaches. <https://doi.org/10.1179/1743284715Y.0000000019> **31**, 1201–1206. ISSN: 17432847. <https://www.tandfonline.com/doi/abs/10.1179/1743284715Y.0000000019> (July 2015).
197. Tancret, F., Toda-Caraballo, I., Menou, E. & Rivera Díaz-Del-Castillo, P. E. J. Designing high entropy alloys employing thermodynamics and Gaussian process statistical analysis. *Materials & Design* **115**, 486–497. ISSN: 0264-1275 (Feb. 2017).
198. Xue, D. *et al.* An informatics approach to transformation temperatures of NiTi-based shape memory alloys. *Acta Materialia* **125**, 532–541. ISSN: 1359-6454 (Feb. 2017).
199. Menou, E. *et al.* Evolutionary design of strong and stable high entropy alloys using multi-objective optimisation based on physical models, statistics and thermodynamics. *Materials & Design* **143**, 185–195. ISSN: 0264-1275 (Apr. 2018).
200. Mamun, O., Wenzlick, M., Hawk, J. & Devanathan, R. A machine learning aided interpretable model for rupture strength prediction in Fe-based martensitic and austenitic alloys. *Scientific Reports 2021 11:1* **11**, 1–9. ISSN: 2045-2322. <https://www.nature.com/articles/s41598-021-83694-z> (Mar. 2021).
201. Murdock, R. J., Kauwe, S. K., Wang, A. Y. T. & Sparks, T. D. Is Domain Knowledge Necessary for Machine Learning Materials Properties? *Integrating Materials and Manufacturing Innovation* **9**, 221–227. ISSN: 21939772. <https://link.springer.com/article/10.1007/s40192-020-00179-z> (Sept. 2020).
202. Fleischmann, E., Miller, M. K., Affeldt, E. & Glatzel, U. Quantitative experimental determination of the solid solution hardening potential of rhenium, tungsten and molybdenum in single-crystal nickel-based superalloys. *Acta Materialia* **87**, 350–356. ISSN: 13596454 (Apr. 2015).
203. Tsao, T. *et al.* Developing New Type of High Temperature Alloys—High Entropy Superalloys. *International Journal of Metallurgical & Materials Engineering* **1**. <http://dx.doi.org/10.15344/2455-2372/2015/107> (June 2015).

204. Chen, J. *et al.* A review on fundamental of high entropy alloys with promising high-temperature properties. *Journal of Alloys and Compounds* **760**, 15–30. ISSN: 09258388 (Sept. 2018).
205. Joele, M. & Matizamhuka, W. R. A Review on the High Temperature Strengthening Mechanisms of High Entropy Superalloys (HESA). *Materials* **14**. ISSN: 19961944. [/pmc/articles/PMC8510092/](https://www.ncbi.nlm.nih.gov/pmc/articles/PMC8510092/) (Oct. 2021).
206. Detrois, M. *et al.* Design and thermomechanical properties of a γ' precipitate-strengthened Ni-based superalloy with high entropy γ matrix. *Journal of Alloys and Compounds* **792**, 550–560. ISSN: 09258388 (July 2019).
207. Manzoni, A. M. & Glatzel, U. *New multiphase compositionally complex alloys driven by the high entropy alloy approach* Jan. 2019.
208. Álvarez, M. A., Rosasco, L. & Lawrence, N. D. Kernels for Vector-Valued Functions: a Review. *Foundations and Trends in Machine Learning* **4**, 195–266. ISSN: 19358237. <https://arxiv.org/abs/1106.6251v2> (June 2011).
209. Ward, L., Agrawal, A., Choudhary, A. & Wolverton, C. A general-purpose machine learning framework for predicting properties of inorganic materials. *npj Computational Materials 2016 2:1* **2**, 1–7. ISSN: 2057-3960. <https://www.nature.com/articles/npjcompumats201628> (Aug. 2016).
210. Ling, J. *et al.* Machine Learning for Alloy Composition and Process Optimization. *Proceedings of the ASME Turbo Expo* **6**. <https://citrination.com> (Aug. 2018).
211. Waber, J. T. & Cromer, D. T. Orbital Radii of Atoms and Ions. *The Journal of Chemical Physics* **42**, 4116. ISSN: 0021-9606. <https://aip.scitation.org/doi/abs/10.1063/1.1695904> (July 2004).
212. in. *CRC handbook of chemistry and physics* 3rd electronic ed. (CRC Press : Taylor & Francis, Boca Raton, Fla., 2021).
213. Lifshitz, I. M. & Slyozov, V. V. The kinetics of precipitation from supersaturated solid solutions. *Journal of Physics and Chemistry of Solids* **19**, 35–50. ISSN: 0022-3697 (Apr. 1961).
214. Morral, J. E. & Purdy, G. R. Particle coarsening in binary and multicomponent alloys. *Scripta Metallurgica et Materialia* **30**, 905–908. ISSN: 0956-716X (Apr. 1994).
215. Philippe, T. & Voorhees, P. W. Ostwald ripening in multicomponent alloys. *Acta Materialia* **61**, 4237–4244. ISSN: 1359-6454 (June 2013).
216. Xia, W., Zhao, X., Yue, L. & Zhang, Z. Microstructural evolution and creep mechanisms in Ni-based single crystal superalloys: A review. *Journal of Alloys and Compounds* **819**, 152954. ISSN: 0925-8388 (Apr. 2020).
217. Zhang, J. X., Wang, J. C., Harada, H. & Koizumi, Y. The effect of lattice misfit on the dislocation motion in superalloys during high-temperature low-stress creep. *Acta Materialia* **53**, 4623–4633. ISSN: 1359-6454 (Oct. 2005).
218. Neumeier, S., Ang, J., Hobbs, R. A., Rae, C. M. & Stone, H. J. Lattice Misfit of High Refractory Ruthenium Containing Nickel-Base Superalloys. *Advanced Materials Research* **278**, 60–65. ISSN: 1662-8985. <https://www.scientific.net/AMR.278.60> (July 2011).
219. Chandra, T., Ionescu, M. & Mantovani, D. Influence of Stacking Fault Energy on Creep Mechanism of a Single Crystal Nickel-Based Superalloy Containing Re. *Materials Science Forum* **706–709**, 2474–2479. <https://www.scientific.net/MSF.706-709.2474> (2012).

220. Perdew, J. P. *et al.* Restoring the density-gradient expansion for exchange in solids and surfaces. <http://arxiv.org/abs/0711.0156%20http://dx.doi.org/10.1103/PhysRevLett.100.136406> (Nov. 2007).
221. Gossdidier, T., Hazotte, A. & Simon, A. Precipitation and dissolution processes in γ/γ' single crystal nickel-based superalloys. *Materials Science and Engineering A* **256**, 183–196. ISSN: 09215093 (Nov. 1998).
222. Yukawa, N., Morinaga, M., Murata, Y., Ezaki, H. & Inoue', S. *High performance single crystal superalloys developed by the d-electrons concept in Superalloys 1988* (1988).
223. Campbell, C. E., Boettinger, W. J. & Kattner, U. R. Development of a diffusion mobility database for Ni-base superalloys. *Acta Materialia* **50**, 775–792. ISSN: 13596454 (Feb. 2002).
224. Zhang, L., Zhou, Y., Jin, X., Du, X. & Li, B. Precipitation-hardened high entropy alloys with excellent tensile properties. *Materials Science and Engineering: A* **732**, 186–191. ISSN: 0921-5093 (Aug. 2018).
225. Goodfellow, A. J. *et al.* The effect of phase chemistry on the extent of strengthening mechanisms in model Ni-Cr-Al-Ti-Mo based superalloys. *Acta Materialia* **153**, 290–302. ISSN: 1359-6454 (July 2018).
226. Sato, A. *et al.* The effects of ruthenium on the phase stability of fourth generation Ni-base single crystal superalloys. *Scripta Materialia* **54**, 1679–1684. ISSN: 1359-6462 (May 2006).
227. Argence, D., Vemault, C., Desvallces, Y. & Fournier, D. *MC-NG: A 4th generation single-crystal superalloy for future aeronautical turbine blades and vanes in Superalloys 2000* (2000).
228. Walston, S., Cetel, A., MacKay, R., Duhl, D. & Dreshfield, R. *Joint Development of a Fourth Generation Single Crystal Superalloy* tech. rep. (NASA, Dec. 2004). <http://www.sti.nasa.gov>.
229. Zheng, F. *et al.* A new strategy of tailoring strength and ductility of CoCrFeNi based high-entropy alloy. *Materials Science and Engineering: A* **774**, 138940. ISSN: 0921-5093 (Feb. 2020).
230. Zhu, J., Lu, X., Balieu, R. & Kringos, N. Modelling and numerical simulation of phase separation in polymer modified bitumen by phase-field method. *Materials & Design* **107**, 322–332. ISSN: 0264-1275 (Oct. 2016).
231. Li, Y. C., Wang, C. P. & Liu, X. J. Thermodynamic assessments of binary phase diagrams in organic and polymeric systems. *Calphad* **33**, 415–419. ISSN: 0364-5916 (June 2009).
232. Li, Y. Thermodynamic and kinetic study of spinodal phase separation in heptane–phenol system. *Calphad* **50**, 113–117. ISSN: 0364-5916 (Sept. 2015).
233. Salabat, A., Tiani Moghadam, S. & Rahmati Far, M. Liquid–liquid equilibria of aqueous two-phase systems composed of TritonX-100 and sodium citrate or magnesium sulfate salts. *Calphad* **34**, 81–83. ISSN: 0364-5916 (Mar. 2010).
234. Meurer, A. *et al.* SymPy: Symbolic computing in python. *PeerJ Computer Science* **2017**, e103. ISSN: 23765992. <https://peerj.com/articles/cs-103> (Jan. 2017).
235. Divya, V. D. *et al.* Microstructure of selective laser melted CM247LC nickel-based superalloy and its evolution through heat treatment. *Materials Characterization* **114**, 62–74. ISSN: 1044-5803 (Apr. 2016).
236. Erickson, G. L. *The Development and Application of CMSX®-10* tech. rep. () .

237. Virtanen, P. *et al.* SciPy 1.0: fundamental algorithms for scientific computing in Python. *Nature Methods* 2020 17:3 **17**, 261–272. ISSN: 1548-7105. <https://www.nature.com/articles/s41592-019-0686-2> (Feb. 2020).
238. Xiang, Y., Sun, D. Y., Fan, W. & Gong, X. G. Generalized simulated annealing algorithm and its application to the Thomson model. *Physics Letters A* **233**, 216–220. ISSN: 0375-9601 (Aug. 1997).
239. Tsallis, C. & Stariolo, D. A. Generalized simulated annealing. *Physica A: Statistical Mechanics and its Applications* **233**, 395–406. ISSN: 0378-4371 (Nov. 1996).
240. Tsallis, C. Possible generalization of Boltzmann-Gibbs statistics. *Journal of Statistical Physics* 1988 52:1 **52**, 479–487. ISSN: 1572-9613. <https://link.springer.com/article/10.1007/BF01016429> (July 1988).
241. *High-temperature high-strength nickel-base alloys no. 393* tech. rep. (INCO / Nickel Institute, 1995).
242. Keller, T. *et al.* Application of finite element, phase-field, and CALPHAD-based methods to additive manufacturing of Ni-based superalloys. *Acta Materialia* **139**, 244–253. ISSN: 13596454 (Oct. 2017).
243. Zhou, Y. *et al.* Thermodynamics up to the melting point in a TaVCrW high entropy alloy: Systematic ab initio study aided by machine learning potentials. *Physical Review B* **105**, 214302. ISSN: 24699969. <https://journals.aps.org/prb/abstract/10.1103/PhysRevB.105.214302> (June 2022).
244. Liu, P. *et al.* Machine learning assisted design of γ' -strengthened Co-base superalloys with multi-performance optimization. *npj Computational Materials* 2020 6:1 **6**, 1–9. ISSN: 2057-3960. <https://www.nature.com/articles/s41524-020-0334-5> (May 2020).
245. Lookman, T., Balachandran, P. V., Xue, D. & Yuan, R. Active learning in materials science with emphasis on adaptive sampling using uncertainties for targeted design. *npj Computational Materials* 2019 5:1 **5**, 1–17. ISSN: 2057-3960. <https://www.nature.com/articles/s41524-019-0153-8> (Feb. 2019).
246. Wen, C. *et al.* Machine learning assisted design of high entropy alloys with desired property. *Acta Materialia* **170**, 109–117. ISSN: 1359-6454 (May 2019).
247. Johnson, R. A. Alloy models with the embedded-atom method. *Physical Review B* **39**, 12554–12559. ISSN: 01631829 (1989).
248. Li, Q.-J., Sheng, H. & Ma, E. Strengthening in multi-principal element alloys with local-chemical-order roughened dislocation pathways. *Nature Communications* 2019 10:1 **10**, 1–11. ISSN: 2041-1723. <https://www.nature.com/articles/s41467-019-11464-7> (Aug. 2019).
249. Zhou, X. W. *et al.* Atomic scale structure of sputtered metal multilayers. *Acta Materialia* **49**, 4005–4015. ISSN: 13596454 (Nov. 2001).
250. Du, J. P., Wang, C. Y. & Yu, T. Construction and application of multi-element EAM potential (Ni-Al-Re) in γ/γ' Ni-based single crystal superalloys. *Modelling and Simulation in Materials Science and Engineering* **21**. ISSN: 09650393 (Jan. 2013).
251. Daw, M. S. & Baskes, M. I. Embedded-atom method: Derivation and application to impurities, surfaces, and other defects in metals. *Physical Review B* **29**, 6443–6453. ISSN: 01631829. <https://journals.aps.org/prb/abstract/10.1103/PhysRevB.29.6443> (June 1984).
252. Daw, M. S. Model of metallic cohesion: The embedded-atom method. *Physical Review B* **39**, 7441–7452. ISSN: 01631829 (1989).

253. Daw, M. S., Foiles, S. M. & Baskes, M. I. *The embedded-atom method: a review of theory and applications* Mar. 1993.
254. Wadley, H. N., Zhou, X., Johnson, R. A. & Neurock, M. *Mechanisms, models and methods of vapor deposition* Jan. 2001.
255. Zhou, X. W., Johnson, R. A. & Wadley, H. N. Misfit-energy-increasing dislocations in vapor-deposited CoFe/NiFe multilayers. *Physical Review B - Condensed Matter and Materials Physics* **69**. ISSN: 01631829 (Apr. 2004).
256. Xie, L., Brault, P., Bauchire, J. M., Thomann, A. L. & Bedra, L. Molecular dynamics simulations of clusters and thin film growth in the context of plasma sputtering deposition. *Journal of Physics D: Applied Physics* **47**. ISSN: 13616463 (June 2014).
257. Lin, Z., Johnson, R. A. & Zhigilei, L. V. Computational study of the generation of crystal defects in a bcc metal target irradiated by short laser pulses. *Physical Review B - Condensed Matter and Materials Physics* **77**, 214108. ISSN: 10980121. <https://journals.aps.org/prb/abstract/10.1103/PhysRevB.77.214108> (June 2008).
258. Stukowski, A., Fransson, E., Mock, M. & Erhart, P. Atomicrex—a general purpose tool for the construction of atomic interaction models. *Modelling and Simulation in Materials Science and Engineering* **25**, 055003. ISSN: 0965-0393. <https://iopscience.iop.org/article/10.1088/1361-651X/aa6ecf%20https://iopscience.iop.org/article/10.1088/1361-651X/aa6ecf/meta> (May 2017).
259. Tromans, D. *Elastic anisotropy of HCP metal crystals and polycrystals* tech. rep. 4 (2011). www.arpapress.com/Volumes/Vol6Issue4/IJRAS_6_4_14.pdf.
260. Shankar Narayana, M., Gopi Krishna, N. & Sirdeshmukh, D. B. X-ray determination of Debye-Waller factors and Debye temperatures of h.c.p. elements Ti, Zr, Ru, Tm, Hf. *Acta Crystallographica Section A: Foundations of Crystallography* **57**, 217–218. ISSN: 01087673. <http://scripts.iucr.org/cgi-bin/paper?S0108767300018560> (Mar. 2001).
261. Purushotham, E. & Gopi Krishna, N. Mean square amplitudes of vibration and associated Debye temperatures of rhenium, osmium and thallium. *Physica B: Condensed Matter* **405**, 3308–3311. ISSN: 09214526 (Aug. 2010).
262. Xiang, Y. & Gong, X. G. Efficiency of generalized simulated annealing. *Physical Review E - Statistical Physics, Plasmas, Fluids, and Related Interdisciplinary Topics* **62**, 4473–4476. ISSN: 1063651X. <https://journals.aps.org/pre/abstract/10.1103/PhysRevE.62.4473> (Sept. 2000).
263. Xiang, Y., Gubian, S., Suomela, B. & Hoeng, J. *Generalized Simulated Annealing for Global Optimization: The GenSA Package An Application to Non-Convex Optimization in Finance and Physics* tech. rep. () .
264. Mullen, K. M. Continuous global optimization in R. *Journal of Statistical Software* **60**, 1–45. ISSN: 15487660. [https://www.jstatsoft.org/index.php/jss/article/view/v060i06%20https://www.jstatsoft.org/index.php/jss/article/view/v060i06](https://www.jstatsoft.org/index.php/jss/article/view/v060i06/v60i06.pdf%20https://www.jstatsoft.org/index.php/jss/article/view/v060i06) (Sept. 2014).
265. Okamoto, H. *Ni-Ru (Nickel-Ruthenium)* May 2009. <https://link.springer.com/article/10.1007/s11669-009-9541-y>.
266. Okamoto, H. *Ni-Re (Nickel-Rhenium)* Aug. 2012. <https://link.springer.com/article/10.1007/s11669-012-0053-9>.
267. Ochiai, S., Oya, Y. & Suzuki, T. Alloying behaviour of Ni₃Al, Ni₃Ga, Ni₃Si and Ni₃Ge. *Acta Metallurgica* **32**, 289–298. ISSN: 00016160 (Feb. 1984).